

This item is the archived peer-reviewed author-version of:

The peculiar potential of transition metal dichalcogenides for thermoelectric applications : a perspective on future computational research

Reference:

Sargin Gozde Ozbal, Sarikurt Sevil, Sevincli Haldun, Sevik Cem.- The peculiar potential of transition metal dichalcogenides for thermoelectric applications : a perspective on future computational research
Journal of applied physics / American Institute of Physics- ISSN 1089-7550 - 133:15(2023), 150902
Full text (Publisher's DOI): <https://doi.org/10.1063/5.0130350>
To cite this reference: <https://hdl.handle.net/10067/2003510151162165141>

The peculiar potential of transition metal dichalcogenides for thermoelectric applications: A perspective on future computational research

Gözde Özbal Sargın,¹ Sevil Sarıkurt,² Hâldun Sevinçli,³ and Cem Sevik^{4, 5}

¹UNAM—National Nanotechnology Research Center and Institute of Materials Science and Nanotechnology, Bilkent University, Ankara 06800, Turkey

²Network Technologies Department, TUBITAK ULAKBIM, 06800 Ankara, Turkey

³Department of Materials Science and Engineering, Izmir Institute of Technology, 35430 Izmir, Turkey

⁴Department of Mechanical Engineering, Faculty of Engineering, Eskisehir Technical University, 26555 Eskisehir, Turkey

⁵Department of Physics & NANOlaboratory Center of Excellence, University of Antwerp, Groenenborgerlaan 171, B-2020 Antwerp, Belgium

(*Electronic mail: gsargin@unam.bilkent.edu.tr, sevil.sarikurt@tubitak.gov.tr, haldunsevincli@iyte.edu.tr, csevik@eskisehir.edu.tr)

(Dated: 4 April 2023)

The peculiar potential transition metal dichalcogenides in regard to sensor and device applications has been exhibited by both experimental and theoretical studies. The use of these materials, thermodynamically stable even at elevated temperatures, particularly in nano and optoelectronic technology, is about to come true. On the other hand, the distinct electronic and thermal transport properties possessing unique coherency, which may result in higher thermoelectric efficiency, have also been reported. However, exploiting this potential in terms of power generation and cooling applications requires a deeper understanding of these materials in this regard. This perspective study, concentrated with this intention, summarizes thermoelectric research based on transition metal dichalcogenides from a broad perspective and also provides a general evaluation of future theoretical investigations inevitable to shed more light on the physics of electronic and thermal transport in these materials and to lead future experimental research.

CONTENTS

		2. Nonequilibrium Green's Functions (NEGF)	10
		3. Molecular Dynamics (MD)	10
I. Introduction	2		
II. Introduction to Thermoelectricity and Transport Phenomena	2	V. Computational Tools for Calculating Transport Coefficients	11
A. Electronic Conduction of Charge and Heat	2	A. Charge Transport	11
B. Seebeck and Peltier Effects	3	1. PERTURBO	11
C. Vibrational Heat Transport	3	2. EPW	11
D. Confinement Effect on Electronic and Vibrational Heat Transport	3	3. EPIC-STAR	11
E. Thermoelectric Efficiency	4	4. BoltzTraP	11
1. Lorenz Number	4	5. AMSET	11
2. Power factor and thermoelectric figure of merit (PF and ZT)	4	6. BoltzWann	12
3. Thermoelectric Quality Factor (TEQF)	5	7. TransOpt	12
4. Electronic Fitness Function (EFF)	5	8. Phoebe	12
5. Maximum efficiency	6	9. AICON	12
III. Electron Transport	6	10. elphbolt	12
A. Simulation Methods	6	11. Non-equilibrium Transport	13
1. Landauer Formalism	6	B. Vibrational Heat Transport	13
2. Boltzmann Transport Equation (BTE)	6	1. ShengBTE	13
IV. Phonon Transport	8	2. Phono3py	13
A. Analytical Models	8	3. AlmaBTE	13
1. Slack Model	8	4. κ ALDO	13
2. Modified Debye-Callaway Model	9	5. OpenBTE	14
3. Modified Callaway-Klemens Approach	9	6. ALAMODE	14
B. Simulation Methods	10	7. hiPhive: a Machine Learning Algorithms	14
1. Phonon Boltzmann Transport Equation	10	VI. Theoretical and Experimental Studies on Thermoelectric Properties of TMDs	14
		A. TiX_2 , ZrX_2 , HfX_2 ($X=S, Se, Te$)	14
		B. CrX_2 , MoX_2 , WX_2 ($X=S, Se, Te$)	16

C. PdX_2 , PtX_2 ($X=S, Se, Te$) 23

VII. Conclusion and Future Perspective 26

Acknowledgments 28

I. INTRODUCTION

The need for clean and renewable energy, triggered by environmental problems globally, has led to an increased interest in thermoelectric (TE) materials, which is one of the alternatives^{1,2}. As a result of subsequent research efforts, these materials are proposed to be used in several different application areas such as Space exploration, industrial applications in remote areas, automobiles, aircraft and helicopters, ships, locomotive industries, recovery of waste heat in industries, decentralized domestic power, and combined heat and power (CHP) generation systems³. Indeed, successful applications have been achieved for particular needs, but widespread use has not been achieved yet due to the lack of highly efficient TE materials at different temperature regimes. Therefore, optimization studies on this material-based technology are still an active research area in both academia and industry. Recently, in the search for materials and devices with better TE performances, experts have focused mainly on the following issues (i) generator modeling based on low-dimensional materials, (ii) finding superior TE materials to achieve the highest efficiency throughout the generator's temperature range, and (iii) applying new strategies to boost TE efficiency of materials. As a result, the tremendous potential of low dimensional materials due to reduced dimensions and nanostructuring, which opens ways to engineer the electrical and thermal transport properties, has been exposed. In this context, two-dimensional (2D) Transition Metal Dichalcogenides (TMDs) have become particularly prominent materials that have generally possessed the crystal structures 2H and 1T with D_{6h} and D_{3d} space groups, respectively. The engineering of electrical and phonon transport properties and the controllable TE nature of this material family has been reported by numerous studies. These notable efforts point out the potential of these materials in future TE applications.

In this review, we focus on recent updates in the TE properties of 2D-TMDs within the scope of the above-mentioned aspects. Figure 1 summarizes all the considered alternative materials. Also, we summarize state-of-the-art techniques for the computational characterization of transport properties of these materials with more accurate techniques previously used in the literature. The structure of the review is organized as follows: Introduction of Transport and Thermoelectric property calculation methods and future perspective, particularly on the computational methods for accurate determination of Thermoelectric Properties of these materials.

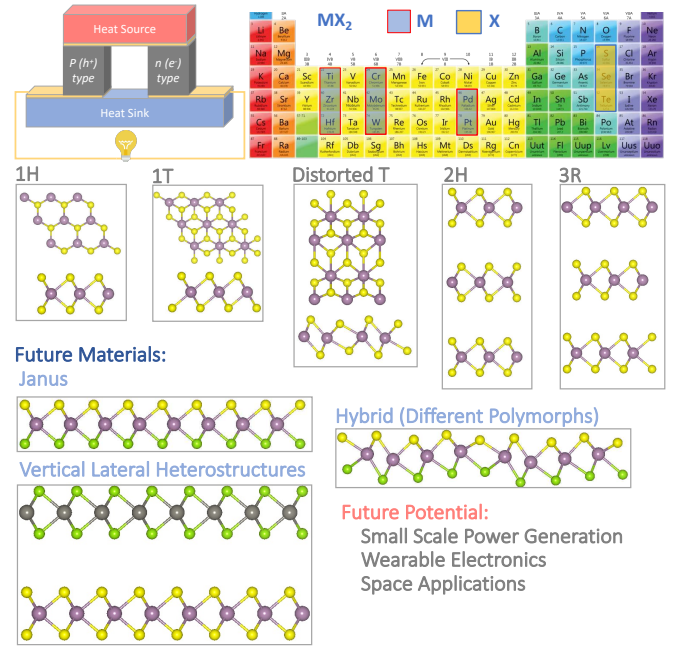


FIG. 1. The metal and chalcogen alternatives for transition metal dichalcogenide crystals in our scope and the schematic representation of possible crystal structures for these 2D materials.

II. INTRODUCTION TO THERMOELECTRICITY AND TRANSPORT PHENOMENA

It is the material's ability to conduct charge and heat, which determines its TE properties, hence it is required to understand the details of electron and phonon flow in given system. The fundamental equations for electron and phonon flow, and definitions for charge and heat conductivities will be given in this section.

A. Electronic Conduction of Charge and Heat

To shed light on the TE potential of materials, we will first introduce expressions for charge and electronic heat current across the material. In the Landauer picture⁴, these find their definitions as

$$I = \frac{2e}{h} \int dE \mathcal{T}(E) [f_L(E) - f_R(E)], \quad (1)$$

$$I_Q = \frac{2}{h} \int dE \mathcal{T}(E) [f_L(E) - f_R(E)] (E - \mu), \quad (2)$$

where E is electron's energy, μ is the chemical potential, h is Planck constant, $f_{L/R}$ is the occupation factors at the left/right reservoir, and \mathcal{T} stands for the electronic transmission spectrum between the reservoirs. Electronic transmission spectrum is explicitly expressed as $\mathcal{T}(E) = M(E)t(E)$ with $M(E)$ being the number of available transmission channels, $t(E)$ the transmission probability.

The ratio between charge to heat current is the essential factor that determines the efficiency. In the bulk (diffusive) limit,

it is useful to use the transport distribution function (TDF) Σ in place of \mathcal{T} . It is customary to define the transport coefficients in terms of the integral \mathcal{L}_n as

$$\sigma = e^2 \mathcal{L}_0, \quad (3)$$

$$T\sigma S = e \mathcal{L}_1, \quad (4)$$

$$T\kappa_0 = \mathcal{L}_2, \quad (5)$$

$$\kappa_{\text{el}} = \kappa_0 - T\sigma S^2, \quad (6)$$

where

$$\mathcal{L}_n = \int dE \left(-\frac{\partial f}{\partial E} \right) \Sigma(E) (E - \mu)^n. \quad (7)$$

In these definitions, σ is the electrical conductivity, S is Seebeck coefficient, and κ_0 and the κ_{el} stand for thermal conductivity (TC) at zero bias and zero current conditions. It is worth noting the relation between the transmission spectrum \mathcal{T} and the transport distribution Σ can be expressed as⁵

$$\Sigma(E) = \frac{l^2}{h} M(E) t(E) = \frac{l}{h} M(E) \lambda(E), \quad (8)$$

where l is the sample length and λ is the electron mean-free-path.

B. Seebeck and Peltier Effects

In its simplest terms, Seebeck effect enables driving electric current due to the temperature gradient across the material. Quantitatively, the Seebeck coefficient (thermopower), expressed as $S = -\Delta V / \Delta T$, corresponds to the effective potential difference at the hot and cold ends per temperature difference. It is related to TDF through Equations 3, 4 and 7. Efforts to enhance the electrical part of the ZT have been made by increasing the Seebeck coefficient and electrical conductivity, which are unfavourably interdependent to each other. Mott's formula^{6,7}, which can be derived through the Sommerfeld expansion of Eq. 4, express the σ dependence of S is given as;

$$S = -\frac{\pi^2 k_B^2 T}{3e} \frac{d}{dE} [\ln \sigma(E)]|_{E=E_f}. \quad (9)$$

Defining conductivity as $\sigma(E) = en(E)\mu(E)$, with n and μ being the carrier density and mobility, one can write⁸⁻¹⁰,

$$S = -\frac{\pi^2 k_B^2 T}{3e} \left\{ \frac{1}{n} \frac{dn}{dE} + \frac{1}{\mu} \frac{d\mu}{dE} \right\}_{E=E_f}. \quad (10)$$

The two terms in Eq. 10 reveal two fundamental mechanisms that enhance S . Sharp changes in the energy dependence of DOS and of the scattering amplitudes around the Fermi level are the key factors to increase S . Although Mott's formula was originally derived to estimate S for bulk materials, it enables a prediction for 2D structures as well.

The reverse phenomenon, known as a Peltier effect¹¹, leads to cooling of a junction between two dissimilar materials due to the applied electric potential. The Peltier coefficient is defined as $\Pi = \dot{Q} / I = TS$, and its optimization conditions are essentially the same with those of the Seebeck coefficient.

C. Vibrational Heat Transport

Phonons are the primary carriers of heat in insulators. In other words, in TE generators most of the heat driven by the temperature difference is carried by lattice vibrations without generating electric current. Similarly in TE coolers, heat flow due to lattice vibrations is in opposite direction with that of the charge carriers. Therefore it is primarily important to suppress lattice TC for TE applications. The simplest definition for lattice TC is given referring to the kinetic theory of gasses as¹²

$$\kappa_L = \frac{1}{3} C v \lambda_p, \quad (11)$$

where C is the specific heat, v is the average group velocity and λ_p is the phonon mean-free-path. Above Debye temperature, λ decreases with temperature and hence the T^{-1} dependence of κ_L . An accurate computation of κ_L requires a detailed account of multi-phonon processes. Thanks to the computational tools developed during the last decades, it has become possible to perform all quantum mechanical calculations of lattice TC of periodic systems, which will be reviewed in the following sections.

D. Confinement Effect on Electronic and Vibrational Heat Transport

Earlier studies, which have been considered milestones in TE research revealed that ZT could reach extraordinary values by reducing the dimensionality of the system¹³⁻¹⁵. High TE efficiency of low dimensional materials compared to bulk counterparts is mainly induced by the confinement effect. Two independently tunable TE parameters i.e. Seebeck coefficient, S and the lattice TC, κ_L are affected by the confinement effect. As seen in Figure 2, sharp changes in the density of states (DOS) are observed by reducing the dimension of the system. Energy-dependent number of available channels $M(E)$ is directly related to the DOS⁵ as follows,

$$D(E) = \sum_{\mathbf{k}} \delta(E - E_{\mathbf{k}}) \quad (12)$$

$$M(E) = \frac{h}{2L} \sum_{\mathbf{k}} |v_x| \delta(E - E_{\mathbf{k}}) \quad (13)$$

Here, v_x is carrier velocity along x direction and L is the length of the system.

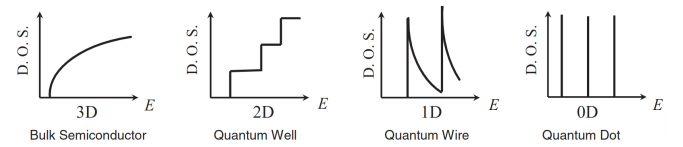


FIG. 2. Electronic DOS for (a) a bulk 3D crystalline semiconductor, (b) a 2D quantumwell, (c) a 1D nanowire or nanotube, and (d) a 0D quantum dot. Reproduced with permission from Advanced Materials 19, 1043 (2007). Copyright 2007 John Wiley and Sons.

The sudden change in DOS with respect to the energy will feed into the electronic transmission spectrum constructively.

Also, S is proportional to the energy derivative of carrier density and hence DOS as can be seen from the Mott-Jones relation. Therefore, while scaling down the system size, the occurrence of significant changes in DOS leads to an increase in S and PF simultaneously.

In the vibrational heat transport aspect, decreasing the dimension from 3D to 2D and 2D to 1D leads to phonon confinement effect on κ_L of 2D structures^{16,17}. This alters the phonon dispersion and contribution of the acoustic phonons to the κ_L as well as causes to increase in phonon-boundary scattering. Among 2D TMDs, lattice transport properties of MoX_2 and WX_2 ($X=\text{S, Se}$) structures are mostly studied by comparing their bulk structures. The results show that reduction from 3D to 2D as well as decreasing layer thickness can be used as an effective tool to lower the κ_L and enhance ZT ^{18,19}. In TMDs, reduction of κ_L is also achieved for nanoribbon structures by nanostructuring²⁰. For further details and discussions about the confinement effect on electronic and vibrational heat transport, there are well-written reviews for interested readers^{8,21–24}.

In this review, we focus on periodic 2D materials. However, it should be mentioned that in a device implementation, the edge states may influence the electronic conductivity and thermoelectric properties in a significant manner^{25–31}. Furthermore, these edge states can be tuned chemically (by ligands, etc.) and/or topologically, leading to very peculiar effects^{29,32}. This is beyond the scope of this work, but the reader might find the following references interesting^{33,34}.

E. Thermoelectric Efficiency

1. Lorenz Number

The fact that electrons carry both charge and heat finds its formulation in the Wiedemann-Franz Law, namely κ_{el} is proportional to σT , and the proportionality constant $L = \kappa_{el}/\sigma T$ is known as the Lorenz number. Enabling an electrical measurement of κ_{el} , Lorenz number plays an important role in materials characterization. For metals and fully degenerate semiconductors Lorenz number is $L_0 = \pi^2 k_B^2/3e^2$. Under non-degenerate conditions lower bound for L_0 is $2(k_B/q)^2$. The precise value of L is determined by the details of the electronic band dispersion, scattering mechanisms, and carrier concentration.³⁵ A Seebeck coefficient dependent Lorenz function was introduced by Kim *et.al.* in order to obtain a more accurate value³⁶. They consider a quadratic band dispersion and acoustic phonon scattering to express the Lorenz number as

$$L = 1.5 + \exp\left(-\frac{S}{116}\right), \quad (14)$$

This equation uses S values which are obtained from experimental data and it yields a reasonable accuracy for the considered cases. However its reliability is jeopardized when a complex band structure is involved.

Wang *et.al.* have shown that Lorenz number is affected by both electronic band structure and energy dependent scatterings.³⁵ They give a detailed definition for L and introduce a

descriptor, $\text{Sen}(E)$, to predict effect of Σ on L ,

$$\text{Sen}(E) = \frac{L(E)}{\Sigma(E)}. \quad (15)$$

They emphasized that, 2D and 3D parabolic bands are found to have different sensitivity as a function of energy due to the distinct profiles of the Σ . Assuming acoustic deformation potential scattering and parabolic bands, the behaviour of L is identical in 1D, 2D and 3D. This method enables to obtain a material-specific Lorenz number.³⁷

The Wiedemann-Franz law has been recently exploited to obtain κ_{el} in 2D TMDs^{38–43}. For PdSe_2 and 1T- HfS_2 , for example, L_0 was assumed as in metals, where $ZT > 1$ was reported for PdSe_2 .^{42,44} There are also other studies, where $L = 1.5 \times 10^{-8} \text{W } \Omega \text{ K}^{-2}$ is used as in non-degenerate semiconductors.³⁸

2. Power factor and thermoelectric figure of merit (PF and ZT)

The power factor, $PF = S^2\sigma$, depends heavily on electronic band structure of a material. Other factors that affect the PF are carrier scattering mechanisms and the doping level. The optimization of the PF is not straightforward. On the one hand, a large DOS effective mass $m_d^* = N_v^{2/3} m_b^*$ results in high S and therefore it is in favor of PF . On the other hand, if high m_d^* originated from large band effective mass $m_b^* = (m_i^* m_t^{*2})^{1/3}$, the Seebeck coefficient increases while mobility and hence electrical conductivity decreases simultaneously. It is worth to note that the DOS effective mass determines the Seebeck coefficient, while conductivity effective mass which is expressed as $m_c^* = 3(m_i^{*-1} + 2m_t^{*-1})^{-1}$ determines the mobility. Furthermore m_b^* and m_c^* are equal, only if

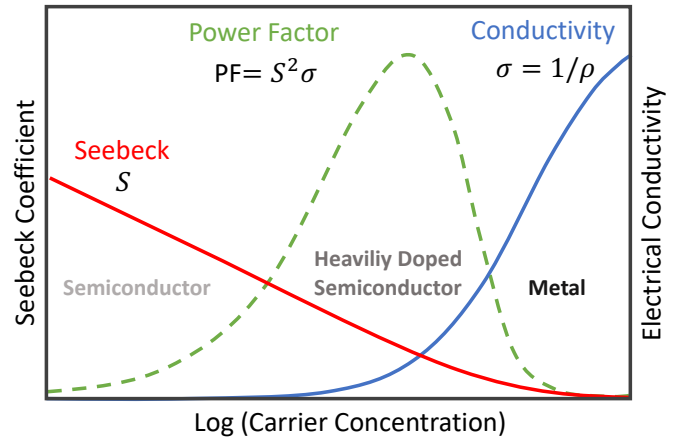


FIG. 3. Dependence of S , σ and PF on carrier concentration. S is highest at lower concentrations, characteristically for semiconductors, whereas σ is highest at higher carrier concentrations as in metals. The power factor is maximized at intermediate values of carrier concentration. Reproduced with permission from Reports on Progress in Physics 51, 459 (1988). Copyright 1998 IOP Publishing.

transverse and longitudinal effective masses are equal so they are interchangeable for spherical carrier pockets^{45–48}. As a result, for optimizing PF one has to take the dominant factor into account. In this case band/valley degeneracy N_v plays a key role in estimating the PF . Band/valley degeneracy N_v increases the m_d^* as well as the number of conduction channels, which are supposed to enhance both S and σ . For example, Cherniushok *et al.* reported that the multi-valley band structure of $\text{Cu}_7\text{PS}_6\text{--Cu}_7\text{PSe}_6$ alloy leads to a significant increase in the Seebeck coefficient and hence PF ⁴⁹. In addition, degenerate valleys/bands of 2D-TMDs like bilayer ZrSe_2 and HfSe_2 results in remarkable ZT values⁵⁰. H-phase of TiS_2 , TiSe_2 , HfS_2 , HfSe_2 , and 1T-phase of ZrO_2 and HfO_2 presents a high p -type PF compared to the others due to the small energy difference between the hole valleys at low symmetry points⁵¹. However large N_v does not always enhance S and σ when inter/intra valley scatterings are enhanced. In summary, tuning S and σ independently is a difficult task, if not impossible, due to their complicated relations carrier concentration. Therefore, several different strategies are often employed to increase PF and suppress lattice TC.

The maximum PF is achieved at intermediate carrier concentrations (Figure 3). It is important to note that the carrier concentration that maximizes PF is not the optimal one for the overall performance because electronic contribution to TC, which is not accounted for in PF , is also a major factor for performance.

Dimensionless TE figure of merit gives the TE efficiency of a material using its electronic and thermal transport properties. In general, ZT increases with temperature for both bulk and 2D materials. ZT is also used to predict the value of TE conversion efficiency and maximum coefficient of performance. ZT plays the main role for determining the efficiency of a material, and it is expressed as

$$ZT = \frac{S^2 \sigma}{\kappa} T, \quad (16)$$

where $\kappa = \kappa_{el} + \kappa_L$ is TC with electronic and phononic contributions. For a TE device to reach the efficiency of traditional devices, the material should have a ZT value greater than 3. Equivalent to Eqn. 16, using Wiedemann-Franz Law, ZT can be written in terms of L ,

$$ZT = \frac{\kappa_e / (\kappa_{el} + \kappa_L) S^2}{L}. \quad (17)$$

Expressing ZT in terms of L is helpful for estimating the threshold value of S , which is required for ZT to exceed the target value when L is set depending on whether the material is a degenerate or non-degenerate semiconductor⁵².

For example, by equating, $L = L_0$ for a degenerate semiconductor, $ZT = 1$ can be attained if S is at least $156 \mu\text{V/K}$ under the assumption that $\kappa_e / (\kappa_{el} + \kappa_L) = 1$.

The major pathways that have been followed in thermoelectrics research are to explore new materials that inherently exhibit high ZT , or to improve ZT of known materials by utilizing diverse strategies. Electronic band structure engineering, and suppression of lattice TC are essential ingredients for optimization. For optimizing TE performance of 2D TMDs,

tuning of band/valley degeneracy, optimization of DOS effective mass m_d^* with band flattening and band gap tuning have been proposed. Apart from electronic part, strategies for reducing the κ_L include increasing phonon-phonon and electron-phonon scatterings.

3. Thermoelectric Quality Factor (TEQF)

A key descriptor in determining the TE efficiency of materials is the dimensionless quality factor β (also known as the material factor). The quality factor is often used to estimate the TE potential of bulk materials. Several different definitions exist in the literature for this quantity, one of which is⁵³,

$$\beta = n_v \mu_v \frac{k_B^2 T}{e \kappa_L}. \quad (18)$$

Here, n_v is the number of valleys, μ_v is the mobility of the carriers in a single valley. Another version is given in closed form as⁵⁴

$$\beta = \mu_0 \frac{m_d^{*3/2}}{\kappa_L}, \quad (19)$$

where μ_0 is the bulk carrier mobility and m_d^* is the DOS effective mass.

One possible definition for low-dimensional materials with complex band structures is given as³⁷

$$\beta(E_f) = \left(\frac{k_B}{e} \right)^2 \frac{\sigma(E_f) T}{\kappa_l}. \quad (20)$$

The temperature and Fermi energy dependence of quality factor emerges when one writes the explicit expressions of κ_l and σ . Furthermore, orders of T and Fermi integral varies with the electronic band dispersion, dimensionality, and the dominant scattering mechanism. More recently, Bilc *et al.*⁴⁷ offer a new quantity called as 2D effective mass quality factor B_m^{2D} which is proportional to the square of the degeneracy of carrier pockets N_v at a given m_{2D} as given below

$$B_m^{2D} = \frac{N_v m_d^{2D}}{(m_{xx} m_{yy})^{1/2}} = N_v^2 \quad (21)$$

Taking the monolayer WSe_2 as an example, one has $N_v = 2$ and $N_v = 6$ for two different extrema in the conduction band and hence $B_m^{2D} = 4$ and $B_m^{2D} = 36$ for n -type doping. In the case of bulk WSe_2 , $B_{m,ab} = 21.1$ and ZT value of 0.55 is smaller than that of one to three layers of WSe_2 .

4. Electronic Fitness Function (EFF)

Transport coefficients (S , σ and κ) are counter correlated, which complicates a systematic search for a superior TE material. Therefore discovery of a high-performance TE material by optimizing the individual components of ZT is a challenging endeavor. To address this difficulty, Xing *et al.*^{55,56} developed the Electronic Fitness Function (EFF) after conducting

a thorough analysis of well-known TE materials. EFF represents the electronic part of the TE performance and acts as a decoupler between conflicting σ and S . It is defined as

$$t_f = \frac{\sigma}{\tau} \frac{S^2}{N^{2/3}} \quad (22)$$

where represents the volumetric DOS. N is proportional to the DOS effective mass and Fermi energy as $N \propto (m_d^*)^{3/2} E_F^{1/2}$ for a parabolic band.

As stated, the EFF is well-known for capturing the trends that signal good TE performance by high-throughput computations in an efficient and cost-effective way⁵⁷⁻⁶¹. It has also been applied to the TMD material family, extensively⁶⁰. Since HfSe₂ and ZrSe₂ monolayers⁶² are potential TE materials, the calculated EFF_{max} values of HfSe₂ and ZrSe₂ monolayers have been reported as 0.24 and $0.25 \times 10^{-19} \text{ W}^{5/3} \text{ m s}^{-1/3} \text{ K}^{-2}$ for p -type carrier and 0.35 and $0.31 \times 10^{-19} \text{ W}^{5/3} \text{ m s}^{-1/3} \text{ K}^{-2}$ for n -type carrier at 300 K, respectively. The corresponding Seebeck coefficients reported as around 500 μ V/K. These results revealed out that EFF can also be used as an effective way to classify promising 2D TE materials as in the case for bulk and half-Heusler alloys^{55,61}.

5. Maximum efficiency

In order to introduce the maximum TE conversion efficiency of a device, it is necessary to take into consideration two factors, ZT and the Carnot efficiency. The theoretical maximum for the performance of a TE generator (TEG) is the Carnot efficiency which is achieved when ZT approaches infinity.⁶³ TE conversion efficiency is defined as

$$\eta = \frac{P_{out}}{Q_{in}} = \frac{\Delta T}{T_H} \cdot \frac{\sqrt{1+ZT} - 1}{\sqrt{1+ZT} + T_C/T_H}, \quad (23)$$

where $\Delta T = T_H - T_C$. The first term in the above equation is the Carnot efficiency (η_{Carnot}) and the second term, which is a function of ZT is the reduced efficiency factor^{64,65}. The power conversion efficiencies of the TE devices consisting of new generation TE materials have been reported as high as 15%. Mostly, PbTe, Skutterudite, half-Heusler, Mg₂Sn_{1-x}Si_x, SnSe, Cu₂Q (Q=S,Se,Te) and Yb₁₄MnSb₁₁ based modules are considered in these new generation TEGs⁶⁶. In the case of atomically thin 2D materials, unconventional design features are required for flexible TE modules^{67,68}. Rapid progress in the fabrication of optimized large-area 2D material films paves the way for implementing 2D materials in flexible TE modules. Among 2D single crystalline TMDs, MoS₂ and WSe₂ outperform compared to commercially used inorganic materials in terms of their PF . 2D MoS₂ and WSe₂ possess n -type PF value of $8500 \mu\text{W m}^{-1} \text{K}^{-2}$ and p -type PF value of $3700 \mu\text{W m}^{-1} \text{K}^{-2}$, respectively^{69,70}. In like manner, the maximum cooling coefficient of performance COP_{max} is defined by the ratio of the amount of cooling to the input electrical power, which can be obtained by optimizing the applied current as⁷¹

$$COP_{max} = \frac{Q_C}{P} = \frac{T_C}{\Delta T} \cdot \frac{\sqrt{1+ZT} - T_H/T_C}{\sqrt{1+ZT} + 1}. \quad (24)$$

Theoretical estimations have shown that the COP can be as high as 35% for $ZT = 4$ and exceeds 60% when $ZT = 20$ ⁷². However, obtaining these ZT values, even for 2D materials, is impossible without utilizing any engineering. Experimental studies reported that maximum cooling COP can exceed 1^{73,74}. Recent research efforts conducted by Wang *et al.* on thermionic converters, which operate in the ballistic regime, suggests that the 2D van der Waals Heterostructures (p -type Pt-G-WSe₂-G-Pt and n -type Sc-WSe₂-MoSe₂-WSe₂-Sc) could exhibit cooling efficiency over 30% of the Carnot efficiency above 450K⁷⁵.

III. ELECTRON TRANSPORT

A. Simulation Methods

1. Landauer Formalism

Landauer approach is sometimes faultily limited only to ballistic transport phenomena but it is equally valid in diffusion and localization regimes, as well. It uses quantum mechanical transmission probabilities to study transport properties of materials and devices. At zero temperature, equilibrium conductance is given as

$$G = \frac{2e^2}{h} \mathcal{T}. \quad (25)$$

Comparing with Eqn. 8, it is seen that the transmission probability $t(E)$ and the number of channels have determinantal roles on both Landauer conductance G and transport distribution function Σ . In the diffusion limit, $t = \lambda/(\lambda + l) \simeq \lambda/l$. In the localization regime transmission probability decays exponentially with length, $t \sim e^{-\xi/l}$, ξ being the localization length. Not only the ballistic regime, but also diffusion and localization regimes emerge using the transmission probabilities in the Landauer picture.

2. Boltzmann Transport Equation (BTE)

The semi-classical Boltzmann Transport Equation (BTE) qualifies both electrons and phonons in position and momentum space via the distribution function $f(x, \nu, t)$. For electrons, the reasonable assumption for the distribution function is using the Fermi-Dirac distribution function. The BTE combined with density functional theory (DFT) is the most prevalent formalism in order to investigate TE transport properties of materials, specifically in diffusive limits. TE transport coefficients are obtained based on BTE by replacing the TDF $\Sigma(E)$ in Eq. 7 with,

$$\Sigma(E) = \sum_{\vec{k}} v_x^2(\vec{k}) \tau(\vec{k}) \delta(E - E(\vec{k})). \quad (26)$$

Here, $\Sigma(E)$ depends on band velocity of charge carrier along the transport direction $v_x(\vec{k})$ with \vec{k} being the wave vector and total relaxation time $\tau(\vec{k})$ which can be calculated using

Matthiessen's rule i.e. $\tau^{-1} = \sum_i \tau_i^{-1}$, where τ_i composed of all different scattering mechanisms.

To date, several studies based on BTE discussed the shape of the TDF that will maximize ZT or PF . Mahan and Sofo, who pioneered these studies, proposed that the TE performance will reach its maximum value when the TDF has a Dirac-delta shape⁷⁶. However, the fact that the materials have an exact Dirac-delta shaped TDF is rather unlikely, therefore, efforts to explore the most effective TDF form for optimizing the TE performance are carried on^{77,78}. Rudderham *et al.*⁷⁹ have been performed a comprehensive study that can elucidate how TE properties change with the scattering models, electronic band dispersion and dimension of the structure. Sevinçli⁸⁰ studied ballistic TE properties of 2D hexagonal group-VA structures within Landauer framework and reported that step-like transmission spectrum $\mathcal{T}(\varepsilon) = \theta(\varepsilon_v - \varepsilon)(k_1 + k_2)a/\pi$ give rise to high PF . Very recently, boxcar function $\Sigma_{ZT}(x) = \Sigma_{max}[\theta(x - x'_a) - (\theta(x - x'_b))]$ and Heaviside function $\Sigma_{PF}(x) = \Sigma_{max}\theta(x - x')$ are found to be best TDF models to obtain upper limit values for ZT and PF . In these expressions while $x'_{a,b}$ is a function of S and ZT , x' depends on S ⁸¹. It is obvious that from the definition of TDF, accurate prediction of relaxation time plays an important role in order to determine the TDF. For the case of common scattering type i.e. electron-phonon scattering, relaxation time (only electron-phonon mediated) is mainly evaluated from deformation potential theory or full electron-phonon coupling matrix elements which are discussed in detail. It should be noted that several study set τ as a constant⁷⁶.

a. Deformation Potential Theory Deformation potential theory (DP theory) was originally formulated by Bardeen and Shockley⁸² in 1950's for long-wavelength acoustic phonon scatterings in non-polar crystals. In this approximation, the occurrence of degenerate energy bands is ignored and the energy surface is accepted as isotropic in the Brillouin zone. Also, only coupling between electrons and acoustic phonons is considered. Several reports on TE properties of 2D materials treat the electron-phonon coupling by using DP theory combined with an effective mass approximation which is a traditionally employed approximation for simplicity as given below,

$$\mu^{2D} = \frac{e\tau}{m^*} = \frac{2e\hbar^3 C^{2D}}{3k_B T m^{*2} E_l^2} \quad (27)$$

where, C^{2D} is the elastic modulus along the transport direction calculated from quadratic curve fitting of the total energy of the unit cell defined as $C = [\partial^2 E / \partial \delta^2] / S^0$. Here, E is the total energy of the system, δ is the applied uniaxial strain, S^0 is the cross-sectional area of the relaxed structure, m^* is the effective mass $m^* = \hbar^2 \left[\frac{\partial^2 E(k)}{\partial k^2} \right]^{-1}$ and E_l represents the DP constant which is energy shift of the band edge position with respect to the lattice deformation $E_l = \Delta E_{CBM(VBM)} / (\Delta l / l_0)$. Mobility definition has been derived assuming that system possesses a single, parabolic and isotropic band structure. However most of systems have more complex band structures exhibiting ellipsoidally shaped pockets as well as valley/band degeneracy.

For anisotropic 2D materials, generalized form including variables in different directions can be expressed as⁸³

$$\mu_x^{2D} = \frac{2e\hbar^3 C_x^{2D}}{3k_B T m_x^{*3/2} m_y^{*1/2} E_{lx}^2}, \quad (28)$$

$$\mu_y^{2D} = \frac{2e\hbar^3 C_y^{2D}}{3k_B T m_x^{*1/2} m_y^{*3/2} E_{ly}^2}. \quad (29)$$

Note that m^* in above Eqs. for systems that possess multiple valley band structures, conductivity effective mass m_c^* should be used in Eq. 27 instead of m^* . The DP theory based mobility calculations of 2D systems possessing electronic band structure with valley/band degeneracy shows this approximation results in significantly larger relaxation-time τ and charge carrier mobility μ values when compared with the full electron-phonon interaction calculations. The source of this overestimation attributed to the following reasons. Intravalley scatterings, which can be the dominant scattering mechanism, are neglected and the material can be anisotropic, which affects not only the effective mass, but also the elastic modulus and DP constant. Since most of the materials do not exhibit purely parabolic valence band peaks or conduction band valleys, anisotropy in the deformation response should not be ignored in the implementation of DP theory⁸⁴.

Over the past few years, studies focusing on e-ph interaction have shown that, DP theory cannot successfully predict mobility in 2D-materials with buckled geometry. It was revealed that ZA, TA intervalley, and ZA intravalley scatterings become predominant caused by buckled geometry of stanene⁸⁵. Therefore DP theory misestimates τ and μ in stanene, and similarly silicene and germanene where horizontal symmetry is broken^{86,87}. However, DP theory works in a good accuracy in graphene and MoS₂ in which out-of-plane mirror symmetry exist⁸⁵. Still, in most of the studies investigating the TE properties of 2D-TMD materials via Boltzmann Transport Theory, τ is estimated with DP theory.

b. Electron-Phonon Coupling Electron-phonon scattering plays an important role in determining the transport properties. The relaxation time in Eq. 26 depends on the electron-phonon interaction matrix elements, which can be obtained using density functional perturbation theory (DFPT). For the scattering of an electron from state ψ_{ik} (bare Bloch eigenstate) to ψ_{jk+q} , the e-ph coupling matrix element is described by⁸⁸

$$g_{ji}^\lambda(\mathbf{k}, \mathbf{q}) = \left(\frac{\hbar}{2M\omega_{q,\lambda}} \right)^{1/2} \langle \psi_{jk+q} | \Delta_{q\lambda} V_{KS} | \psi_{ik} \rangle, \quad (30)$$

where $\Delta_{q\lambda} V_{KS}$ is the derivative of the self-consistent Kohn-Sham potential with respect to the atomic displacement associated with the phonon mode λ and wavevector \mathbf{q} . Assuming a constant relaxation time, e-ph scattering relaxation time τ_k can be calculated as

$$\frac{1}{\tau(i, \mathbf{k})} = \frac{2\pi}{\hbar} \sum_{j\mathbf{q}\lambda} |g_{ji}^\lambda(\mathbf{k}, \mathbf{q})|^2 \quad (31)$$

$$\times \{ [f_{jk+q}^0 + n_{q\lambda}^0] \delta(\varepsilon_{jk+q} - \varepsilon_{ik} - \hbar\omega_{q\lambda}) + [1 + n_{q\lambda}^0 - f_{jk+q}^0] \delta(\varepsilon_{jk+q} - \varepsilon_{ik} + \hbar\omega_{q\lambda}) \}. \quad (32)$$

$$+ [1 + n_{q\lambda}^0 - f_{jk+q}^0] \delta(\varepsilon_{jk+q} - \varepsilon_{ik} + \hbar\omega_{q\lambda}) \}. \quad (33)$$

and carrier mobility can be expressed within the Boltzmann transport theory as⁸⁸,

$$\mu = e \frac{\sum_i \int \tau(i, \mathbf{k}) v^2(i, \mathbf{k}) \left(\frac{\partial f_{i\mathbf{k}}^0}{\partial E_{i\mathbf{k}}} \right) d\mathbf{k}}{\sum_i \int f_{i\mathbf{k}}^0 d\mathbf{k}}. \quad (34)$$

Note that, in order to obtain an accurate e-ph coupling matrix, Wannier function-based interpolation techniques as implemented in EPW code (mentioned below) can be used. Since, this approach is computationally expensive an alternative method electron-phonon averaged EPA was developed and tested^{52,89}. Here, electron DOS and phonon DOS are typically treated independently of each other, and their equilibrium values are used.

In thermoelectrics, carrier mobility plays a key role as seen in the definition of electrical conductivity, $\sigma = ne\mu$. In general, 2D TMDs have low e/h mobility at room temperature where upper limit is around $300 \text{ cm}^2\text{V}^{-1}\text{s}^{-1}$. Relatively small μ values of 2D TMD's compared to bulk silicon and gallium arsenide (1366 and $8500 \text{ cm}^2\text{V}^{-1}\text{s}^{-1}$)⁹⁰ have prompted researchers to discuss to improve strategies specially for the use of 2D TMDs in field effect transistors (FETs)⁹¹. Recent studies elaborately investigating the origins of low μ in these materials show that intrinsic carrier mobility is suppressed by LO phonon scattering in most TMDs. Unlike other compounds, for MoS_2 and WS_2 , the mobility is limited by LA phonon scatterings⁹⁰. Another study focusing on the mobility values of six prototype 2D materials including MoS_2 , WS_2 and WSe_2 points out the critical role of intervalley scatterings, band anisotropy, and doping density. Their findings show that, μ takes the value of 144 and $60 \text{ cm}^2\text{V}^{-1}\text{s}^{-1}$ for MoS_2 and WS_2 based on BTE calculations with EPC matrix elements⁹². Among 2D TMDs, WS_2 has the highest μ of $246 \text{ cm}^2\text{V}^{-1}\text{s}^{-1}$, followed by MoS_2 ($183 \text{ cm}^2\text{V}^{-1}\text{s}^{-1}$), while the μ for all the others are below $100 \text{ cm}^2\text{V}^{-1}\text{s}^{-1}$ as demonstrated in Figure 4⁹³. Besides carrier mobility calculations, there are on-going efforts to determine the TE coefficients of 2D-TMDs with the inclusion of e-ph coupling. Electron mobility and PF ($47 \text{ cm}^2\text{V}^{-1}\text{s}^{-1}$ and $2.93 \times 10^{-3} \text{ Wm}^{-1}\text{K}^{-2}$) of MoS_2 move closer to experimentally obtained values with considering e-ph interaction⁹⁴. Comprehensive study on TE properties of $1\text{T}'$ -phase MX_2 ($M = \text{Mo}, \text{W}; X = \text{S}, \text{Se}, \text{Te}$) family shows that MoS_2 and MoSe_2 have the strongest and weakest e-ph coupling, respectively⁹⁵. Among them, MoSe_2 exhibits hole carrier mobility and PF values of $690 \text{ cm}^2\text{V}^{-1}\text{s}^{-1}$ and $6 \times 10^{-3} \text{ Wm}^{-1}\text{K}^{-2}$ at room temperature due to the weak e-ph coupling. These findings reveal that $1\text{T}'$ MoSe_2 can be a potential TE material. Furthermore, dramatic differences are observed in σ_e and PF for ZrS_2 when τ is obtained from DP theory and from full determination of e-ph coupling⁹⁶. For bulk MoSe_2 , it is reported that S is negligibly affected by accounting e-ph interaction⁹⁷.

The effect of electron-phonon interaction on lattice thermal conductivity of TMDs was addressed only a few works. It was shown for MoS_2 and PtSSe_2 that strong suppressions of κ_L takes place due to strong e-ph interaction and characteristic band structure of PtSSe_2 ⁹⁸

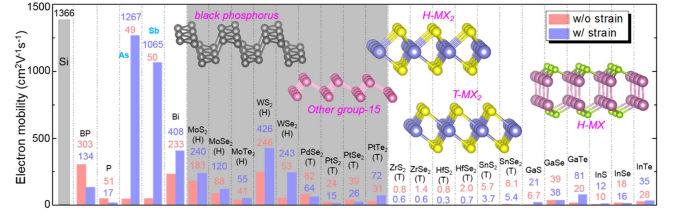


FIG. 4. Intrinsic electron mobility at room temperature of the 2D semiconductors commonly studied in experiments. Results of materials without strain are shown in red, and those with a 3% uniform tensile strain are shown in blue. The inset figures show the side views of those 2D materials. Reproduced with permission from Physical Review Letters 125, 177701 (2020). Copyright 2020 American Physical Society.

IV. PHONON TRANSPORT

A. Analytical Models

1. Slack Model

Approximations proposed by Slack⁹⁹ back in 1973 work reasonably well for estimating the lattice TC of a diverse amount of materials. Slack suggested that, under several conditions and assumptions, it is possible for a material to exhibit high lattice TC if it meets four criteria, including (1) light average atomic mass, (2) strong interatomic bonding, (3) non-complex crystal structure and (4) low anharmonicity. The first three criteria are related to the harmonic properties. In this model, only the acoustic phonons contribute to heat transport and Umklapp scattering dominates in κ_{Slack} . Slack derived the following equation for κ_L of 3D materials^{99,100},

$$\kappa_{\text{Slack}} = A \frac{m\theta_D^3 \delta n^{1/3}}{\gamma^2 T}, \quad (35)$$

where δ^2 is the unit-cell area per atom, n is the number of atoms in the unit cell, A is a constant given in terms of average Grüneisen parameter (γ) of phonon modes, as $A = 2.43 \times 10^{-8} \times [1 - 0.514/\gamma + 0.228/\gamma^2]^{-1}$, and m is the average atomic mass of the unit cell. Although this equation was originally derived by considering 3D materials, it is also quite successful in estimating the TC of 2D materials.

Muratore *et al.*¹⁰¹ showed that the Slack Model can accurately predict the cross-plane TCs of hexagonal TMD compounds *i.e.* MoS_2 , WS_2 and WSe_2 . However, the experimental measurements show roughly an order of magnitude reduction in in-plane lattice TC of thin film TMDs. Since Slack's equation regards only the phonon-phonon interactions, effective TC can be defined with combining κ_{Slack} and boundary scattering which is essential for 2D materials¹⁰¹

$$\frac{1}{\kappa_{\text{Measured}}} = \frac{1}{\kappa_{\text{Slack}}} + \frac{1}{\frac{1}{3} C_v v_p^2 \tau_s} \quad (36)$$

where C_v is the volumetric heat capacity, v_p is the phonon group velocity, $\tau_s = L/v_p$ is the relaxation time with L being

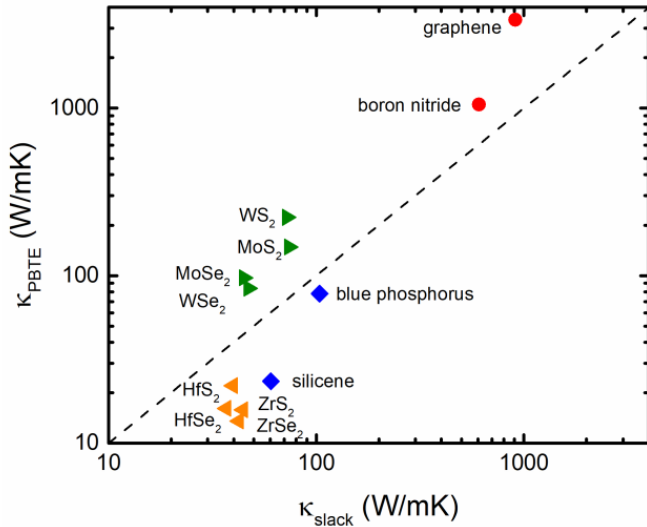


FIG. 5. Comparison of TCs of some 2D materials calculated from the Slack equation (x -axis) and from the first-principles-based PBTE (y -axis). Reproduced with permission from Review of Modern Physics 90, 041002 (2018). Copyright 2018 American Physical Society.

the scattering length. In a recent paper¹⁰², κ_L of several 2D materials including TMDs are reported by comparing Peierls-Boltzmann transport equation and Slack's equation. Figure 5 shows a comparison of κ_L values of some 2D materials as obtained from Slack equation against those from more sophisticated methods. We note that, even though the trends are well captured by Slack's equation, one should be very careful to use it for the calculations that require a high accuracy, such as TE efficiency prediction.

2. Modified Debye-Callaway Model

Another widely used method to predict κ_L is the Debye-Callaway method. The modified version, built upon the traditional Debye-Callaway theory, developed on the calculation of lattice TC by averaging the contributions from acoustic and optical branches based on their specific heat. The total phonon scattering rate ($1/\tau_C$) is the sum of normal phonon scattering ($1/\tau_N$) which does not contribute to the direct thermal resistance, and the Umklapp phonon-phonon scattering ($1/\tau_U$) which is the resistive rate. Also, the contribution of the three acoustic modes to the lattice TC into transverse and longitudinal modes is expressed as $\kappa = \kappa_{LA} + \kappa_{TA} + \kappa'_{TA}$. Finally, the partial conductivities κ_i of longitudinal and transverse acoustic modes (i corresponds to LA, TA or TA' modes) are written as^{103–105}

$$\kappa_i = \frac{1}{3} C_i T^3 \left\{ \int_0^{\theta_i/T} \tau_c^i(x) I(x) dx + \frac{\left[\int_0^{\theta_i/T} \frac{\tau_c^i(x)}{\tau_N^i(x)} I(x) dx \right]^2}{\int_0^{\theta_i/T} \frac{\tau_c^i(x)}{\tau_N^i(x) \tau_{ij}^i(x)} I(x) dx} \right\}. \quad (37)$$

Here, θ_i is the Debye temperature for each acoustic branch i , $C_i = k_B^4 / (2\pi^2 \hbar^3 v_i)$, $I(x) = x^4 e^x / (e^x - 1)^2$ and $x = \hbar\omega / (k_B T)$. Using this approach the final value of lattice TC can be calculated via producing the required parameters i.e. θ , phonon velocity (v), and Grüneisen parameter (γ) by quasiharmonic approximation. The modified Debye-Callaway model has been implemented in a novel software tool named AICON¹⁰⁶. Here, the contribution of optical branches is also included and θ , v , and γ are obtained from DFT calculations. The room temperature κ_L value for penta-graphene estimated with this code, $568 \text{ W m}^{-1} \text{ K}^{-1}$ is close to the one calculated with the highly accurate approach adopted in ShengBTE code¹⁰⁷. Also, for the Penta-BCN monolayer the obtained room temperature κ_L value, $98 \text{ W m}^{-1} \text{ K}^{-1}$ is comparable with the literature¹⁰⁸. When other scattering mechanisms, i.e boundary scattering, are included, it can be concluded that the κ_L of many low-dimensional materials can be calculated with the AICON package. The Modified Debye-Callaway Model via AICON has not been used for 2D TMDs materials yet. Further details about the capabilities of AICON can be found in Section V.

3. Modified Callaway-Klemens Approach

The Modified Callaway-Klemens approach, which has been used to investigate graphene by Nika *et al.*¹⁰⁹, is another alternative to calculate lattice TC of 2D materials. It treats three-phonon scatterings exactly using accurate phonon dispersions of 2D materials, hence the 2D nature of the systems is incorporated more accurately. The model was also applied to calculate the sample length and temperature-dependent lattice TC of single-layer and multilayer hexagonal boron nitride by D'Souza *et al.*¹¹⁰. Within this model, lattice TC is expressed by the following equation

$$\kappa = \frac{1}{4\pi k_B T^2 N \delta} \sum_s \int_{q_{min}}^{q_{max}} [\hbar\omega_s(q)]^2 v_s^2(q) \tau_{U,s}(q) \times \frac{e^{\frac{\hbar\omega_s(q)}{k_B T}}}{[e^{\frac{\hbar\omega_s(q)}{k_B T}} - 1]^2} q dq, \quad (38)$$

where $\tau_{U,s}$ is the three-phonon umklapp scattering corresponding to branch s at the wave vector q expressed as

$$\tau_{U,s} = \frac{M v_s^2(q) \omega_{D,s}}{\gamma_s^2(q) k_B T \omega_s^2(q)} \quad (39)$$

The 2D character manifests itself in the phonon DOS and restrictions on the phonon Umklapp scattering phase-space. When compared to experimental findings, the modified Callaway-Klemens model results in compatible values for lattice TC of bulk h-BN. However for single layer h-BN, it misestimates κ of monolayer h-BN due to the RTA^{109,110} based solution of BTE.

B. Simulation Methods

1. Phonon Boltzmann Transport Equation

The phonon BTE was first formulated by Peierls¹¹¹ in 1929 as the microscopic description of the phonon heat conduction in dielectric crystals, where he defined heat flow in terms of motions and scatterings of phonon gas, using the BTE. Let us assume that a small temperature gradient $\vec{\nabla}T$ causes to deviation of the phonon distribution function from its equilibrium distribution, $n_{\vec{q}j} = n_{\vec{q}j}^0 + n_{\vec{q}j}^1$ where the $n_{\vec{q}j}$ represents non-equilibrium distribution function. Linearized Peierls-Boltzmann transport equation is given as¹¹²,

$$\vec{v}_{\vec{q}j} \cdot \vec{\nabla}T \left(\frac{\partial n_{\vec{q}j}}{\partial T} \right) = \left(\frac{\partial n_{\vec{q}j}}{\partial t} \right)_{scattering}, \quad (40)$$

where $\vec{v}_{\vec{q}j}$ is the velocity of a phonon with wavevector \vec{q} in branch j . The left hand side of the Eq. 40 represents phonon diffusion induced by the thermal gradient while the right hand side shows different scatterers like impurities, boundaries, defects and other phonons. Here, we will not go into details of this approach, since calculation steps of solving BTE by implementing iterative method are reviewed in a number of papers^{113,114}. The use of the BTE method in combination with the DFT calculations has worked very well in predicting the TC of 2D materials¹¹⁵⁻¹¹⁷. Therefore solving BTE becomes one of the most powerful and widely used approaches to obtain TC through the equation

$$\kappa_{\alpha\beta} = \sum_{\vec{q},j} C_{\vec{q}j} v_{\vec{q}j\alpha} v_{\vec{q}j\beta} \tau_{\vec{q}j\beta}, \quad (41)$$

where $C_{\vec{q}j} = (\hbar\omega_{\vec{q}j})V^{-1}\partial n_{\vec{q}j}^0/\partial T$ is the volume-normalized mode-specific heat and the α, β denote direction in Cartesian coordinates. The velocity of phonon mode (\vec{q}, j) and mode specific heat capacity $C_{\vec{q}j}$ which are the two of three components of the TC are obtained from the harmonic force constants while the relaxation time is obtained from the anharmonic force constants.

2. Nonequilibrium Green's Functions (NEGF)

The fully quantum mechanical non-equilibrium Green function (NEGF) formalism can be applied to both electron and phonon transport. Vibrational heat current at the harmonic limit, where only elastic processes are taken into account, can be written as

$$J = \int_0^\infty \frac{d\omega}{2\pi} \hbar\omega T_{ph}(\omega) (f_B(\omega, T_L) - f_B(\omega, T_R)). \quad (42)$$

Here, $T_{ph}(\omega)$ phonon transmission spectrum and $f_B(\omega, T_L)$, $(f_B(\omega, T_R))$ is the Bose-Einstein distribution function at temperature T_L (T_R). Phonon transmission spectrum is expressed through the Caroli formula as,

$$T(\omega) = Tr[\Gamma_L(\omega)G_C^r(\omega)\Gamma_R(\omega)G_C^a(\omega)], \quad (43)$$

where $G_C^{r/a}(\omega) = (G_C^a(\omega))^\dagger$ is the retarded (advanced) Green function for the central part of the device, while $\Gamma_{L(R)}(\omega)$ is the broadening matrix due to the left (right) contact. Consequently, the thermal conductance is expressed as

$$\sigma_{ph} = \frac{1}{2\pi} \int_0^\infty \hbar\omega T(\omega) \frac{\partial f(\omega, T)}{\partial T} d\omega. \quad (44)$$

As temperature goes to zero, thermal conductance approaches to the limiting value $\sigma_{ph} = M_{ac}\sigma_{ph}^0$, where M_{ac} is the number of acoustic phonon branches and

$$\sigma_{ph}^0 = \frac{\pi^2 k_B^2 T}{3h} \quad (45)$$

is the quantum of thermal conductance. Phonon transmission spectra and thermal conductance values of most of 2D-TMDs are reported by implementing NEGF formalism⁵¹. Transition from the ballistic to diffusive regime can be simply achieved by describing the phonon transmission spectrum as

$$T(\omega) = \frac{M(\omega)}{1 + (L/l_0(\omega))}. \quad (46)$$

The term $M(\omega)$ is the number of phonon modes at frequency ω , l_0 being the phonon mean free path and L is the device length¹¹⁸. The effects of inelastic processes are included by calculating the appropriate self-energy terms. They require to be computed self-consistently therefore increase the computational cost and limit the applicability of the method to systems containing large number of atoms. Further details NEGF formalism for lattice thermal transport can be found in Refs.^[119-128]

3. Molecular Dynamics (MD)

The other powerful tool to predict lattice TC is molecular dynamics (MD) simulations. Classical MD simulations are well-founded under the assumption that all of the phonon modes are fully excited above Debye temperature. Therefore quantum corrections should be included at lower temperatures¹²⁹. Classical MD simulations benefit from the knowledge of the dynamics of each particle based on Newton's second law of motion and interatomic potentials. There are two frequently used MD methods to predict the TC. (1) Equilibrium Molecular Dynamics (EMD) - uses Green-Kubo relation, where thermal transport properties are computed from the fluctuation-dissipation theorem. Due to the high statistical errors within the nature of the method, it is debatable how much this method is efficient when applied on monolayer systems with low TC ($> 1Wm^{-1}K^{-1}$). (2) Non-equilibrium Molecular Dynamics (NEMD) simulations are based on Fourier's law in which temperature gradient is generated by two thermostats along the transport direction.

The accuracy of an MD calculation rests predominantly on the used interatomic potential. Recently, temperature-dependent phonon properties of 2D TMDs, namely, MoS₂, MoSe₂, WS₂, and WSe₂ are calculated by utilizing previously derived Stillinger-Weber-type potentials¹³⁰⁻¹³². Phonon lifetimes and mode contributions are obtained by employing the

spectral-energy-density (SED) method. Although the SED method is computationally expensive, it is commonly used for phonon properties of 2D materials since it considers all non-harmonic effects as well as further phonon scatterings. The calculated room temperature values 91.66, 89.43, 39.94, and 29.05 $\text{Wm}^{-1} \text{K}^{-1}$ for WS_2 , MoS_2 , WSe_2 , and MoSe_2 , respectively¹³².

V. COMPUTATIONAL TOOLS FOR CALCULATING TRANSPORT COEFFICIENTS

A. Charge Transport

1. PERTURBO

The open-source software package PERTURBO, which has been proposed by Zhou *et al.*¹³³, provides efficient and generally applicable *ab initio* techniques for quantitatively investigating electron-phonon interactions and carrier dynamics in metals, semiconductors, insulators, and 2D materials. Currently, PERTURBO code requests electronic structure and electron-phonon coupling data (DFT and DFPT calculations) obtained by Quantum Espresso^{134,135} code and Wannier interpolated¹³⁶ localized orbitals as implemented in WANNIER90 code^{137,138} to minimize the computing cost. PERTURBO is a powerful tool to investigate electron-phonon interactions, relaxation times, electrical conductivity, carrier mobility, and Seebeck coefficient, either within the relaxation time approximation (RTA)¹³⁹ or with the iterative solution of the BTE¹⁴⁰.

2. EPW

Electron-phonon Wannier (EPW)^{141,142} is a DFPT and Maximally Localized Wannier Function¹⁴³ based simulation tool that calculates electron-phonon interactions and related properties such as the total electron-phonon coupling strength, the transport spectral function, and the temperature-dependent electron and hole mobility within the Boltzmann transport formalism. It uses a highly accurate approach to characterize the TE transport properties of semiconductor materials and has been recently applied 2D materials such as ZrS_2 ⁹⁶, antimonene⁸⁴, and Janus Ga_2SSe ¹⁴⁴, successfully. Accurate determination of carrier relaxation times is highly critical in order to correctly estimate the TE potential of a material. In this regard, the EPW code comes into prominence as a critical tool for TE research.

3. EPIC-STAR

Energy-dependent Phonon- and Impurity-limited Carrier Scattering Time Approximation (EPIC STAR) software¹⁴⁵ is developed by Deng *et al.* to calculate the intrinsic semiconductor charge transport properties such as carrier mobility, electrical conductivity, Seebeck coefficient, and electrical

TC for inorganic materials. Within this software, a generalized Eliashberg function was used for short-range electron-phonon scattering whereas analytical expressions developed from first-principles for long-range electron-phonon and electron-impurity scattering mechanisms. For well-known materials (polar, non-polar isotropic, anisotropic) with high mobility and high TE performance such as Si, GaAs, Mg_2Si , and NbFeSb, EPIC STAR approach is validated by comparing the results with both available experimental data and the output of other theoretical approaches¹⁴⁵.

EPIC STAR is based on DFPT calculations and semi-classical BTE. Deng *et al.*¹⁴⁵ revealed that they successfully reduced the computational cost of first-principles calculations within EPIC STAR by at least one order of magnitude compared to other accurate first-principles-based methods such as EPW method¹⁴¹. This novel technique provides great fidelity, particularly for non-polar and polar semiconductors, with extremely low computing cost following DFPT calculations by incorporating a modified Eliashberg function and adding polar optical phonon contribution, impurity scattering, and free carrier screening.

4. BoltzTraP

BoltzTraP¹⁴⁶ and its updated version BoltzTraP2¹⁴⁷ are open-source codes that can be used to calculate TE coefficients such as Seebeck coefficient, electrical conductivity, electrical TC as functions of temperature and chemical potential. These codes are based on semi-classical Boltzmann transport theory with constant relaxation time approximation (CRTA). BoltzTraP uses the linearized BTE to compute a smoothed Fourier expression of energy bands. BoltzTraP2 also calculates Onsager transport coefficients for extended systems using BTE.

The usage of both BoltzTraP and BoltzTraP2 have been particularly common, especially in high-throughput thermoelectrics studies^{60,148–150} due to their numerical reliability and being efficient approach for calculating analytic representations of quasi-particle energies.

5. AMSET

Ab initio Scattering and Transport (AMSET) is developed by Ganose *et al.*¹⁵¹ to predict carrier scattering rates of semiconductors and insulators based on first-principles computations. It is a powerful tool for computing electron lifetimes and transport parameters in solid-state materials. The code is based on a combined Fourier-linear interpolation scheme by using electronic eigenvalues obtained by DFT as implemented in BoltzTraP2 package¹⁴⁷. The main objective for this software is to be used in conjunction with DFT based methods such as EPW¹⁴¹ and PERTURBO¹³³, which have much higher computational resource requirements.

6. BoltzWann

Using maximally localized Wannier function interpolation, Pizzi *et al.*¹⁵² developed a novel algorithm for assessing the TE transport features of solid-state materials. Briefly, within the algorithm, the CRTA based solution of semi-classical BTE for the homogeneous periodic systems is obtained using band energies and band derivatives derived from Wannier interpolations. Here, exponential localization of the Wannier functions enables a highly accurate solution of the Brillouin zone integrals with very moderate computational costs. With this approach, the band derivatives can be evaluated analytically at an arbitrary point without the need to rely on finite-difference methods, producing numerically stable results even at band crossings and near weakly avoided crossings. Similar to the BoltzTraP^{146,147} case the relaxation times for electrons must be evaluated with another approach or empirically to end up with final transport properties with this software.

TE coefficients (S , σ) of pristine and Janus Pd dichalcogenides were evaluated by Moujaes *et al.*¹⁵³ using BoltzWann code previously. Here, they estimate the relaxation time parameters by using the electron-phonon coupling values as implemented in EPW code.

7. TransOpt

TransOpt (formerly named as Transoptic)¹⁵⁴ allows to evaluate electrical transport coefficients such as electrical conductivity, Seebeck coefficient, electronic TC, Lorenz number, power factor, and EFF using BTE. Within this software, the carrier relaxation times are determined by the recently developed constant electron-phonon coupling approximation. The code is interfaced with both the Vienna ab initio Simulation Package (VASP) and Quantum Espresso. In the latter case, the code uses full first-principles electron-phonon data.

In general, the BTE based codes neglect dependence of relaxation time on the electronic structure. However, taking it into account, TransOpt predicts electrical transport properties with better accuracy. Moreover, the implemented momentum matrix method results in an efficient solution to the well-known band crossing problem.

8. Phoebe

Phoebe (a collection of PHONon and Electron Boltzmann Equation solvers), proposed by Cepellotti *et al.*¹⁵⁵ is an open-source software package to investigate the electron and phonon transport properties. A scattering matrix formalism has been implemented to develop and solve the BTE for crystals in the project. The electron-phonon, phonon-phonon, boundary, and phonon isotope scattering contributions to transport characteristics have been considered within the framework.

The goal in creating this program was to use the relationship between thermal and electrical conduction to create a single framework for characterizing electron and phonon trans-

port features of materials. In addition, this software package has also been designed to handle the intense computational effort of *ab initio* transport computations by taking into account MPI-OpenMP hybrid parallelism, distributed memory data structures, and GPU acceleration. To acquire the first-principles coupling strength of the phonon-phonon interaction, Phoebe was interfaced with Phono3py¹⁵⁶, and Sheng-BTE¹⁵⁷, while the electron-phonon interaction was interfaced with Quantum ESPRESSO^{134,135}. Fourier/Wannier interpolation¹³⁶ methods or EPA approximation⁸⁹ are used to accomplish accurate integration of the BTE and associated transport features.

9. AICON

AICON (Ab Initio Conductivities)¹⁰⁶ is a software developed in Python for computing lattice TC of crystalline bulk materials using the modified Debye-Callaway model, which is outlined above. The implemented approach considers the contributions from both acoustic and optical branches based on their specific heat unlike traditional Debye-Callaway theory. The empirical parameter-free algorithm requests phonon spectrum, phonon velocity, and Grüneisen parameter, which can be calculated using third-party *ab initio* packages. Therefore, the fast and accurate approach implemented on AICON enables high-throughput calculations of lattice TC even in large and complex systems. Moreover, the program results in different scattering processes rates which are highly beneficial for understanding the phonon transfer behavior. Recently, it has been applied for bulk 3R-TMD crystals¹⁵⁸ with reasonable accuracy.

AICON2¹⁵⁹ is the recent fast and more accurate version based on the generalized Kane band model and perturbation theory in the framework of the RTA. The algorithm considers the three scattering mechanisms that affect the total relaxation time; acoustic phonon scattering, polar optical phonon scattering, and ionized impurity scattering. Again, all the requested input data can be obtained from the first principles calculations. The code was tested on a group of semiconductors, and a reasonable agreement with the experiment was presented¹⁶⁰.

10. elphbolt

The elphbolt software solves the coupled electron-phonon BTEs from first principles. The code has a critical advantage due to its ability to calculate the effect of the non-equilibrium phonons on the electronic transport (phonon drag) and non-equilibrium electrons on the phononic transport (electron drag) in a fully self-consistent scheme. The charge (mode resolved electronic charge conductivity and electronic TC), lattice (mode resolved phonon TC and phonon Peltier coefficient), and therefore TE transport coefficients (mode resolved electronic Seebeck and Peltier coefficients) and the effect of e-ph drag on all of the above quantities for the temperature gradient and electric fields can be predicted with it. The code can

be applied to 3D and 2D insulators, semiconductors, semimetals, and metals¹⁶¹.

It has been applied to investigate TE properties of *n*-doped gallium arsenide¹⁶². The predicted low-temperature enhancement in the Seebeck coefficient which can not be captured with the uncoupled electron BTE clearly shows the advantage of the fully coupled electron-phonon BTEs and thus elphbolt.

11. Non-equilibrium Transport

Non-equilibrium Green's function-based electron transport codes are also useful to estimate the thermoelectric performance of in particular nanostructured materials. The open-source examples which can be used to investigate transport properties via tight-binding or density functional theory Hamiltonians are TranSiesta¹⁶³, GOLLUM¹⁶⁴, SMEAGOL¹⁶⁵, OpenMX¹⁶⁶, Kwant¹⁶⁷, Kite¹⁶⁸, and CP2K¹⁶⁹. The pros and cons analysis of each framework depends on the crystal and structure you investigate.

The non-equilibrium prediction of phonon transmission and transport has been also readily implemented in some codes such as GOLLUM.

B. Vibrational Heat Transport

The thermal transport properties of semiconductors can be predicted by MD Simulations but this approach requires highly accurate interatomic-potentials. In fact, for structures with complex chemical composition and bond order, interatomic potential generation is complicated and time-consuming work. Therefore, in order to investigate the TE properties of crystalline semiconductor solids, one of the best options is the first principles-based solution of phonon BTE. Within this approach, the phonon properties and lattice thermal transport coefficients can be obtained with second-order harmonic and third-order anharmonic interatomic force constants calculated from first-principles simulations. In this regard, the well known options are reviewed below.

1. ShengBTE

ShengBTE¹⁵⁷ is a software package calculating the lattice TC of crystalline bulk materials and nanowires with diffusive boundary conditions. The code is capable of both RTA and the full iterative solution of the BTE. The current version use second-, third-, and fourth-order interatomic force constants calculated by first-principles approaches as the main input. Then, it computes converged sets of phonon scattering rates and uses them to obtain many related quantities such as mean free paths and relaxation times. The software is useful in the search of novel materials with targeted thermal conduction properties, and for the in-depth understanding of experimental measurements of thermal transport in solids. It has been applied to many different solids for defect-free bulk- and nanocrystalline solids accurately^{157,170}. It has been also used for

different TMD crystals and captured results in good agreement with both other predictions and available experimental data^{150,171,172}.

FourPhonon¹⁷³ is an extension module to ShengBTE for calculating the four-phonon scattering rates with an adaptive energy broadening scheme and determining the corresponding TC. Inspired by the work of Feng and Ruan's four-phonon calculation framework¹⁷⁴, which has led the community to revise the understanding of thermal transport theory, the developers implemented this extension.

2. Phono3py

The software Phono3py¹⁵⁶ addresses the phonon-phonon interaction and related properties using the supercell approach in a way similar to the Phonopy¹⁷⁵ code which is developed by the same authors to perform phonon calculations at harmonic and quasi-harmonic levels. Thermal transport-related quantities such as lattice TC, phonon lifetime/linewidth, imaginary part of self-energy, the joint density of states (JDOS), and weighted-JDOS can be obtained with this code via the solution of BTE both within the RTA and including the full scattering operator.

Lattice TCs of zincblende- and wurtzite-type compounds with 33 combinations of elements are calculated with the single-mode relaxation-time approximation and a full solution of the linearized phonon Boltzmann equation from first-principles anharmonic lattice dynamics calculations. The results are in very good agreement with available experimental data¹⁵⁶.

3. AlmaBTE

AlmaBTE¹⁷⁶ is another tool that can be used to solve BTE for phonons from first-principles. With the advantage of the futures such as specialized models to address in-plane and cross-plane TC of thin films¹⁷⁷, a variance-reduced Monte Carlo solver of the BTE for the steady-state regime^{178,179} in one dimension the code predictively tackles phonon transport not only in bulk crystals but also in thin films, superlattices, and multiscale structures with size features in the nm- μ m range. The recent version also includes FourPhonons, a tool that, as the name suggests, can handle four-phonon scattering. In addition to the general transport quantities, thermal conductances and effective TCs, space-resolved average temperature profiles, and heat-current distributions resolved in frequency and space can be obtained with AlmaBTE. The capabilities implemented in AlmaBTE are well suited to use for novel materials and nanostructure characterization.

4. κ ALDo

The software κ ALDo¹⁸⁰ is introduced as a versatile and scalable open-source software to compute phonon transport not only in crystals but also in glasses, and nanostructured

solids. The code is based on a unified workflow, which implements both the BTE and the Quasi Harmonic Green-Kubo (QHKG)¹⁸¹ methods to take into account material disorder. The code includes different solvers for the BTE, the RTA, the self-consistent solution, and the direct inversion of the scattering matrix. Moreover, It is also feasible for systems with few tens of atoms per cell which is not possible with the other available BTE solvers in the literature. As noted by the developers, the advantages of κ ALDO are based on both the approach implemented and its versatile architecture that takes advantage of both CPU multi-threading and GPU. The modular design enables this code to couple seamlessly to a variety of force calculators, using either interatomic force constants or first-principles approaches.

The thermal transport properties of crystalline and partially disordered silicon-based systems and silicon-germanium alloy clathrates with largely reduced TC were successfully characterized with this approach¹⁸⁰.

5. OpenBTE

OpenBTE¹⁸², is a solver for the first-principles, multi-dimensional phonon BTE that can obtain space-dependent heat transport deterministically. It is particularly capable of the calculation of the temperature and heat flux maps, and also the prediction of mode-resolved effective TC. The used anisotropic-mean-free-path BTE approach¹⁸³, a method based on the interpolation of the phonon populations onto the vectorial mean-free-path space, has proven to yield results with the desired accuracy much faster than its counterparts. This code has capabilities to be used in nanoscale heat transport simulations and therefore may lead to the development of novel nanomaterials for thermal energy applications.

6. ALAMODE

ALAMODE^{184,185} is a software designed for analyzing lattice anharmonicity and lattice TC of crystalline solids. The code is based on the versatile first-principles data-driven model potentials that pave the way to investigating the lattice thermal transport properties of solids either by BTE or MD. Within this code, in addition to finite displacement, anharmonic force constants can be extracted from the trajectory of first-principles MD simulations at high temperatures. The code successfully estimates the phonon lifetimes and lattice thermal transport properties of severely anharmonic materials via combining the perturbation theory with the solution to the self-consistent phonon theory¹⁸⁶. Moreover, the implemented potential represented as a Taylor expansion with respect to atomic displacements enables users to perform NEMD simulations for thermal transport, which is another powerful and reliable tool to estimate the effects of impurities and interfaces that could be of great significance in TE materials.

7. hiPhive: a Machine Learning Algorithms

The Hiphive Python package¹⁸⁷ enables the construction of force constant models up to arbitrary order. In order to calculate thermal transport properties via first-principles based solution of BTE, the efficient extraction of force constants (FCs) is crucial to obtain accurate phonon relaxation rates. The approach implemented in the Hiphive enable users to efficiently calculate high-order FCs both in large systems and systems with low-symmetry. The code is interfaced with most of the well-known first principles codes via the atomic simulation environment (ASE) package¹⁸⁸. With the advantage of various powerful machine learning algorithms, the code can reach considerable accuracy by using much lower number of FCs than the ones used in regular first principles approaches. Therefore, hiPhive becomes genuinely advantageous for obtaining thermal transport properties for large and/or low symmetry systems (defects, interfaces, surfaces, large unit cells, etc.). The code successfully applied to different TMDs and Janus SnSSe, and PtSte^{189,190}.

VI. THEORETICAL AND EXPERIMENTAL STUDIES ON THERMOELECTRIC PROPERTIES OF TMDs

In this section, we review the recent progress and research updates in the study of transport and TE properties of TMDs and related nanostructures. Note that the comparison of TE property calculations is a quite complicated issue due to the variety of approaches used in both electronic and thermal transport calculations. In particular, the variety of considered approaches to estimate relaxation times of carriers and the length of non-periodic material dimension in thermal transport characterization of 1D and 2D materials have strong influence on the final efficiency. Therefore, here we discuss the potential of TMDs as TE materials considering only reported ZT values to take your attention to how the current state of the art in transport property calculations is far from clearly explaining the TE materials due to the lack of available theoretical approach to accurately determine carrier relaxation times including the effect of scattering sources such as structural defects and disorders. Considering this fact, we assess the promising TMDs for future TE applications in three different groups, as a result of an intense review of TE performance measures obtained with different theoretical and experimental approaches.

A. TiX_2 , ZrX_2 , HfX_2 ($\text{X}=\text{S}, \text{Se}, \text{Te}$)

Single-layer 1T-ZrS₂ was experimentally synthesized about a decade ago^{191,192}. Subsequently, several research groups investigated structural, electronic, thermal, as well as TE properties of this material. In this regard, based on first-principles calculations combined with Landauer-Büttiker formalism, Özbal *et al.*⁵¹ reported the *n*-type ballistic ZT values of 1T-ZrS₂ as 0.57 and 1.75 at 300 K and 800 K, respectively. The *p*-type ballistic ZT values (0.23 and 0.87) are lower than

that of n -type, which is attributed to higher effective mass of the electrons compared to holes. Implementing the BTE-based approaches with the help of BoltzTraP and BoltzTraP2 packages, the highest p -type ZT value for ZrS_2 at 1000 K was calculated as 0.12¹⁹³, and 2.4 was reported under %6 strain at 300 K³⁸. At higher temperatures, the optimum performance for n - and p -type ZT values of 5.1 for 1T- ZrS_2 were reported again under %6 strain³⁸. Moreover, Sharma *et al.*⁹⁶ examined the impact of e-ph coupling on TE properties of this material by using EPW software. In this work, τ values were computed from the imaginary part of electron self-energy and compared with the ones obtained from the DP theory. Since the S is insensitive to the τ , for both the cases it follows the same behavior and has the nearly same magnitude. However, for σ and PF , an order of magnitude difference in σ and PF were obtained. Therefore, the strong influence of the chosen approach to characterize τ was reported by EPW and DP calculations on ZrS_2 .

A similar material, 1T- $ZrSe_2$ was investigated along with TE properties by Abdulsalam *et al.*¹⁹³. The ZT value, 0.43 was predicted for $ZrSe_2$ at 1000 K with hole doping¹⁹³. Another study⁵¹ has revealed that the 1T- $ZrSe_2$ shows moderate p -type TE performance compared to 2H counterpart at the ballistic limit. On the other hand, 2H- $ZrSe_2$ possesses a reasonably high ZT value of around 1.5 at 300 K both for p - and n -types as shown in Figure 6. Qin *et al.*³⁹ adopted the BTE approach within the rigid band and constant relaxation-time approximations (RBA and CRTA) as implemented in the BoltzTraP code and they reported that the material under the 7.5% tensile strain have a remarkable high ZT values 4.58 and 3.84, respectively.

TE properties of hafnium dichalcogenides were also considered¹⁹³ and maximum ZT values of 1.65 (1000 K) and 0.43 (600 K) were obtained for HfS_2 and $HfSe_2$, respectively. BTE approach based calculations clearly revealed that the maximum ZT values of monolayer $ZrSe_2$ and $HfSe_2$ are around 1 for optimal p - and n -doping concentrations⁶². Here, both lower electronic transport coefficients and higher κ_L of $HfSe_2$ results in comparable ZT value with that of $ZrSe_2$. Within the ballistic limit, Ozbal *et al.*⁵¹ obtained that p - and n -type ZT can be as high as 1.57 and 1.28, respectively at 300 K as depicted in Figure 6. The strain engineering was also applied to the 1T- HfS_2 and outstanding TE performance of this materials was obtained above %6 biaxial strain at room temperature⁴². Here, electronic transport properties were calculated by implementing BoltzTraP software package whereas κ_L values were predicted by ShengBTE. In unstrained case, Wang *et al.* reported the maximum $n(p)$ -type ZT value as 1.09 (0.09) which is in good agreement with previously reported values, 0.96¹⁹⁴ and 0.13¹⁹⁵ for n - and p -types, respectively. n -type ZT value reaches its maximum of 2.29 at %6 while p -type ZT reaches its peak value of 2.29 at %7 biaxial stain. However, the values 0.6 and 0.67⁵¹ obtained for ballistic limit are not compatible with these values. Similarly, prominent enhancement in p - and n -type ZT has been calculated by using same methods for 1T- $HfSe_2$. As strain increases, the collective effect of the increase in PF and decrease in κ_L leads to an improvement in p - and n -type ZT up to 2.47 and 1.91 respec-

tively, at room temperature¹⁹⁶. In another study¹⁹⁷, adopting the κ_L values from a previously reported results^{62,198}, the strong influence of strain on ZT values was also depicted for $TiSe_2$ via BoltzTraP2 calculations.

Before moving on to the nanostructuring strategies, we treat the TE properties of TiX_2 monolayers. Ozbal *et al.*⁵¹ reported that, HSE06 correction exhibits a transition from semimetallic to semiconducting behavior for 1T- TiS_2 . Opening bandgap results in an n -type ZT exceeding 1 when the temperature reaches 800 K. 2H- TiS_2 possesses larger p -type ZT compared to 2H- $TiSe_2$ and $TiTe_2$ while n -type ZT values of all are around 1 at 300 K. A considerable enhancement in ZT has been found at an %8 biaxial strain by utilizing the Boltzmann transport theory with the BoltzTraP code. The maximum ZT value of 0.95 (0.82) is obtained for the p -type (n -type) doped system¹⁹⁹. From the experimental point of view, enhancement in ZT of layered 1T-type TiS_2 powders which were pretreated by following the shear pulverization approach has been observed with a maximum value of 0.7 at 673 K²⁰⁰. The source of this remarkable improvement in ZT is due to the increase in σ and decrease in κ_L as a result of enhanced grain boundary scattering.

Wang *et al.*²⁰¹ exfoliated the 2D TiS_2 nanosheets from layered polycrystalline powders, and then assembled them with C_{60} nanoparticles. The produced C_{60}/TiS_2 hybrid films exhibit a $ZT \sim 0.3$ at 400 K due to the increase in PF and degradation in κ_L . Similarly, for the organic intercalation of layered TMD, $TiS_2[(HA)_{0.08}(H_2O)_{0.22}(DMSO)_{0.03}]$, the ZT value is predicted as 0.28 at 373 K. These results point out the potential of layered hybrid TMD structures for moderate temperature, flexible, wearable TE generator technology²⁰².

$TiSe_2$ undergoes metal to insulator transition when tensile strain is applied²⁰³. Convergence of valleys, enlarged bandgap, and higher m_{eff} provides an enhancement in S as well as PF at a strain of 4%. Under 4% strain, opposite charge carriers participate in electronic transport at high temperatures leading reduction in S . Widening band gap serves to enhance the S while reducing both electrical and TC in a non-linear fashion. As a consequence, PF increases with strain and increasing temperature in the high-doping limit above 10^{10} cm^{-2} .

The above-summarized results clearly show that TiX_2 , ZrX_2 , HfX_2 ($X=S, Se, Te$) layers possess a potential for TE applications. But further engineering is necessary to reach the desired efficiency for future technological applications. Indeed, previous studies show that layer-, nano-, and heterostructure-engineering has the potential to reach that point. Within this context, Yan *et al.*⁵⁰ investigated the TE properties of bilayers of 1T- MS_2 ($M = Zr, Hf$) by using BoltzTraP package within the RBA and constant scattering time (τ) approximation. They predicted that in particular for $HfSe_2$ bilayer, multilayer interactions give rise to an increased phonon scattering and therefore lower TC. This simply results in enhanced TE performance for multilayer structures. The room temperature ZT values of these multilayers were calculated as 3.83 and 1.84 for $HfSe_2$ and $ZrSe_2$, respectively. TE coefficients of van der Waals heterobilayers consists of $HfSe_2/TiSe_2$, $ZrSe_2/HfSe_2$ and $ZrSe_2/TiSe_2$ combinations are

also investigated using BoltzTraP2 tool¹⁹⁷. ZT values are estimated via previously reported κ_L values^{62,198}. Among these vertical heterostructures, $ZrSe_2/TiSe_2$ gives considerably high ZT values as 1.72. Also, TE coefficients of combinations of MX_2 bilayers where $M = Zr, Hf$; $X = S, Se$ are studied in the most favorable stacking geometry by Khan *et al.*²⁰⁴. The Boltzmann semi-classical theory and CRTA as implemented in BoltzTraP code were used and a relatively larger PF at 1200 K was reported for the ZrS_2 - $HfSe_2$ structure.

Beyond bilayers and heterostructures, constructing in-plane superlattice monolayer (SLM) structures is another strategy to achieve improvement in ZT . Ding *et al.*²⁰⁵ studied the transport properties of $ZrSe_2/HfSe_2$ SLM considering different doping levels. The electronic transport properties were obtained using semi-classical Boltzmann transport theory and the RBA as implemented in BoltzTraP code. Using the ShengBTE code, the κ_L was obtained via solving the phonon BTE. The Authors reported valley degeneracies and flat band characteristics in CB of SLM as well as the stair-like behavior in DOS leading to an enhancement in S . Also, the phonon scatterings at the superlattice interfaces were predicted as resulting in suppressed κ_L . Thus, as a result of these combined effects exceptionally high n - and p -type ZT values as 5.3 and 3.9 for two perpendicular directions were achieved.

As another engineering approach, TE properties of armchair nanoribbons of the 2D trigonal phase of $HfSe_2$ are comprehensively studied by implementing DFT calculations coupled with Landauer formalism²⁰. One-third of phonon thermal conductance of the 2D case was obtained for considered nanostructures. The performed detailed transport analyses showed that the n -type S and the PF differ because of the structural symmetry, whereas the p -type TE coefficients are not significantly influenced. As a result, the p -type ZT value of $HfSe_2$ nanoribbons at 300 and 800 K are calculated as 4 and 3 times larger than the 2D case, respectively. Also, the influence of structural defects on TE properties of HfS_2 monolayer was investigated by introducing two types of vacancy and dopant¹⁹⁴. Based on BTE calculations within CRTA which were carried out with BoltzTraP code, a slight increase in room temperature ZT value was reported. In addition, for Hf vacancy more than 50% enhancement in ZT was predicted.

Recently, the influence of the SOC on the TE properties of HfS_2 , $HfSe_2$, and $HfSSe$ monolayers have been examined¹⁹⁵ in the framework DFT calculations combined with BTE. The TE properties were calculated in BoltzTraP code considering CSTA. Calculated band structures with SOC reveal that VBM keeps possessing 2-fold degeneracy while the conduction band splits into the degenerate valleys at the M point. Even if S remains almost same values for both n - and p -type doping, n -type $S^2\sigma/\tau$ namely PF increases about 1.5-2 times compared to results without SOC. These results clearly show the necessity of SOC inclusion in calculations. In addition, for $ZrTe_2$, it is found that, TE coefficients including S and σ_e and the κ_{el} strongly depending on the XC functional choice²⁰⁶.

Another degree of freedom has been included in the TE research of TMDs with the successful realization of Janus layers. Thence, the TE properties of 2D Janus TMDs have attracted notable attention, recently.

Transport coefficients of Janus $ZrSSe$ monolayer²⁰⁷ and $ZrSSe$, $HfSSe$, and $PtSSe$ vdW heterostructures²⁰⁸ were calculated through solving BTE within the CRTA, as implemented in the BoltzTraP code. After revealing of dynamical stability of $ZrSSe$ monolayer, the κ_L has been calculated by solving linearized phonon BTE with a single-mode RTA implemented in Phono3py. $ZrSSe$ was reported to have κ_L of $1.68 \text{ W m}^{-1} \text{ K}^{-1}$ which was considerably lower than that of $ZrSe_2$. Although $ZrSSe$ and $ZrSe_2$ possess almost same n -type ZT_{el} , one may predict that the $ZrSSe$ monolayer show better n -type TE performance due to the difference in κ_L . Here, $ZrSSe$ - $HfSSe$ heterostructure with a larger PF was predicted as the most efficient TE material candidate among other investigated constituting pure and Janus TMDs.

It has also been recently demonstrated that both monolayer and bilayer $HfSSe$ have a tremendous potential as TE materials where maximum ZT values approaching 3.24 and 5.54 at 600 K, respectively²⁰⁹. Besides, the variation of band structure of this material with strain enable the engineering the TE properties²¹⁰. All the aforementioned κ_L and ZT values of group IVB TMDs are summarized in Table I. The depicted ZT values correspond to the room temperature, otherwise it is stated in the Table.

B. CrX_2 , MoX_2 , WX_2 ($X=S, Se, Te$)

TE properties of bulk and few-layered structures of MoX_2 , WX_2 ($X=S, Se$) have been explored experimentally by different research groups using different methods^{69,70,211-222}. Peimyoo *et al.*²¹⁷ determined the TC values of suspended 1L- and 2L- WS_2 as 32 and 53 $\text{W m}^{-1} \text{ K}^{-1}$ at $T=300$ K by micro-Raman spectroscopy. Using frequency dependent time-domain thermoreflectance method, Jiang *et al.*²²⁰ measured the in-plane TC values of bulk MoS_2 , WS_2 , $MoSe_2$, and WSe_2 as 82, 120, 35, and 42 $\text{W m}^{-1} \text{ K}^{-1}$, respectively. Moreover, the layer number dependence of TC for 1L-3L WSe_2 and interfacial thermal conductance between few-layered WSe_2 and the substrate were demonstrated by Zhang *et al.*²²¹ using opto-thermal Raman technique. They observed that the TC of WSe_2 reduces while the layer thickness increases from 1L ($\kappa_L=37 \pm 12 \text{ W m}^{-1} \text{ K}^{-1}$) to 3L ($\kappa_L=20 \pm 6 \text{ W m}^{-1} \text{ K}^{-1}$). The other intriguing result is that suspended WSe_2 has a larger TC compared to supported one. Beyond these experimental efforts, NEMD calculations were implemented to authenticate layer dependence of TC and the decreasing behaviour with an increase in layer number was confirmed²²¹. The experimental TC values and interfacial thermal conductance of 1L-3L are summarized in Table II.

The temperature dependent TC of suspended few-layer MoS_2 was experimentally measured by different researchers using Raman spectroscopy. Sahoo *et al.*²¹³ and Yan *et al.*²¹⁴ carried out temperature- and laser-power-dependent Raman scattering experiments to obtain TC of few-layer MoS_2 . Sahoo *et al.*²¹³ reported TC of 11 layers MoS_2 with 6.6 nm thick as $\sim 52 \text{ W m}^{-1} \text{ K}^{-1}$. Yan *et al.*²¹⁴ observed the TC of single layer MoS_2 as $34.5 \pm 4 \text{ W m}^{-1} \text{ K}^{-1}$. Taube *et al.*²¹⁹ measured the TC of supported MoS_2 as $62.2 \text{ W m}^{-1} \text{ K}^{-1}$ at room tem-

TABLE I. Lattice thermal conductivity (conductance) and ZT values of Ti, Zr, and Hf dichalcogenides at room temperature.

Material	Phase (1T/2H)	Theoretical Method (Tool)	κ_L ($\text{Wm}^{-1}\text{K}^{-1}$)	ZT		ZT_{max}		Refs.
				n -type	p -type	n -type	p -type	
TiS ₂	2H	Landauer	0.95 (conductance per width)	1.05	0.98	2.66@800K	2.14@800K	51
	1T	Landauer	-	0.37	0.11	1.21@800K	0.38@800K	51
	1T	BTE (BoltzTraP)	1.58	0.82	0.95			199
TiSe ₂	2H	Landauer	0.95 (conductance per width)	0.9	0.86	2.09@800K	1.81@800K	51
TiTe ₂	2H	Landauer	0.7 (conductance per width)	0.9	0.4	0.87@500K	0.38@500K	51
ZrS ₂	1T	BTE (BoltzTraP2)	1.99	1.8	2.4	5.1 @800K	5.1@800K	38
	1T	Landauer	0.83 (conductance per width)	0.57	0.23	1.75@800K	0.87@800K	51
	1T	BTE (BoltzTraP2)	7.61	< 0.03	< 0.04	0.06@1000K	0.12@1000K	193
ZrSe ₂	1T	BTE (BoltzTraP2)	3.41	<0.01	0.04	<0.01@1000K	0.043@1000K	193
	1T	Landauer	0.71 (conductance per width)	0.63	0.22	1.76@800K	0.65@800K	51
	1T	BTE (BoltzTraP)	0.94	4.58	3.84	-	-	39
ZrTe ₂	1T	BTE (BoltzTraP)	1.2	-	-	0.95@400K	0.87@600K	62
	2H	Landauer	0.54 (conductance per width)	1.42	1.41	3.61@800K	2.96@800K	51
	2H	Landauer	0.55 (conductance per width)	1.18	1.06	1.88@500K	1.73@500K	51
HfS ₂	1T	BTE (BoltzTraP2)	5.32	0.12	0.75	0.12@1000K	1.65@1000K	193
	1T	BTE (BoltzTraP)		1	0.96	1.23@1200K		194
	1T	BTE (BoltzTraP)	2.836			0.84@600K		195
HfSe ₂	1T	Landauer	0.71	0.67	0.26	1.96@800K	0.92@800K	51
	2H	Landauer	0.65	1.17	1.38	2.92@800K	3.03@800K	51
	2H	BTE (BoltzTraP)		1.05	0.98			194
HfTe ₂	1T	BTE (BoltzTraP2)	3.3	0.2	0.2	0.3@500K	0.43@600K	193
	1T	Landauer	0.59 (conductance per width)	0.75	0.26	2.11@800K	0.84@800K	51
	1T	BTE (BoltzTraP)	1.8	-	-	0.95@400K	0.87@400K	62
HfSSe	1T	BTE (BoltzTraP)	1.517			0.90@600K		195
	1T	BTE (BoltzTraP)	1.16	1.91	2.47	-	-	196
	2H	Landauer	0.51 (conductance per width)	1.28	1.57	3.04@800K	3.3@800K	51
HfTe ₂	2H	Landauer	0.48 (conductance per width)	1.17	0.56	1.34@800K	0.91@800K	51
HfSSe	Janus	BTE (BoltzTraP)	2.23			0.81@600K		195
HfSSe	Janus	BTE (BoltzTraP)	4.18	1.18	0.35	3.24@600K	1.01@600K	209
HfSSe	Janus/bilayer	BTE (BoltzTraP)	3.93	2.33	0.82	5.54@600K	2.5@600K	209
HfSe ₂ /TiSe ₂	1T-Hetero	BTE (BoltzTraP2)	Ref. ^{62,198}	0.16				197
ZrSe ₂ /HfSe ₂	1T-Hetero	BTE (BoltzTraP2)	Ref. ^{62,198}	1.34				197
ZrSe ₂ /TiSe ₂	1T-Hetero	BTE (BoltzTraP2)	Ref. ^{62,198}	1.72				197

perature. And its value drastically decreases to $7.45 \text{ W m}^{-1} \text{ K}^{-1}$ when temperature is increased to 450 K. In addition to these, Jo *et al.*²¹⁵ measured the basal-plane TC of suspended four- and seven layer MoS₂ as (44-50) and (48-52) $\text{W m}^{-1} \text{ K}^{-1}$ at room temperature using micro-bridge method, respectively. This differences can be originated from preparation process of exfoliated monolayer or few-layer MoS₂ and also measurement method.

TC of single-layer (1L) and bilayer (2L) MoS₂ and MoSe₂ reported by Zhang *et al.*²¹⁸ using optothermal Raman technique. At room temperature, the measured TC values for 1L MoS₂ and MoSe₂, were reported as (84 ± 17) and $(59 \pm 18) \text{ W m}^{-1} \text{ K}^{-1}$, whereas 2L MoS₂ and MoSe₂ exhibit lower TC with a value of (77 ± 25) and $(42 \pm 13) \text{ W m}^{-1} \text{ K}^{-1}$, respectively. Hippalgaonkar *et al.*⁶⁹ measured the TE PF of few-layer MoS₂ in the metallic regime at room temperature and observed the largest PF for bilayer MoS₂ as $8.5 \text{ mW m}^{-1} \text{ K}^{-2}$ at applied gate voltage ($V_g = 104 \text{ V}$). The corresponding carrier concentration was reported as $n_{2D} \simeq 1.06 \times 10^{13} \text{ cm}^{-2}$.

They also demonstrated the effective mobilities of monolayer, bilayer and trilayer, at room temperature, as $37 \text{ cm}^2 \text{ V}^{-1} \text{ s}^{-1}$, $64 \text{ cm}^2 \text{ V}^{-1} \text{ s}^{-1}$ and $31 \text{ cm}^2 \text{ V}^{-1} \text{ s}^{-1}$ respectively. The thermoelectric PF of suspended monolayer MoS₂ was reported²²³ as $28 \text{ mW m}^{-1} \text{ K}^{-2}$ at $n_{2D} \simeq 1.0 \times 10^{12} \text{ cm}^{-2}$. Wang *et al.*²²² explored the in-plane TC values for varying sample thicknesses of suspended MoS₂ and MoSe₂ using nanosecond energy transport state resolved Raman (ns ET-Raman) technique with high accuracy. While the layer thickness for MoS₂ ranges from 45 nm to 115 nm and for MoSe₂ from 40 nm to 135 nm, the lattice TC was enhanced from 40.0 ± 2.2 to $74.3 \pm 3.2 \text{ W m}^{-1} \text{ K}^{-1}$ for MoS₂, and from 11.1 ± 0.4 to $20.3 \pm 0.9 \text{ W m}^{-1} \text{ K}^{-1}$ for MoSe₂. The larger in-plane thermal conductance of thicker samples originates from the bigger heat conduction cross-section. The long mean free path (long-MFP) of thicker sheets implies a reduced surface scattering effect. So, thickness dependency is caused by considerable surface scattering of long-MFP phonons. It is worth pointing out that surface scattering was found to significantly impact

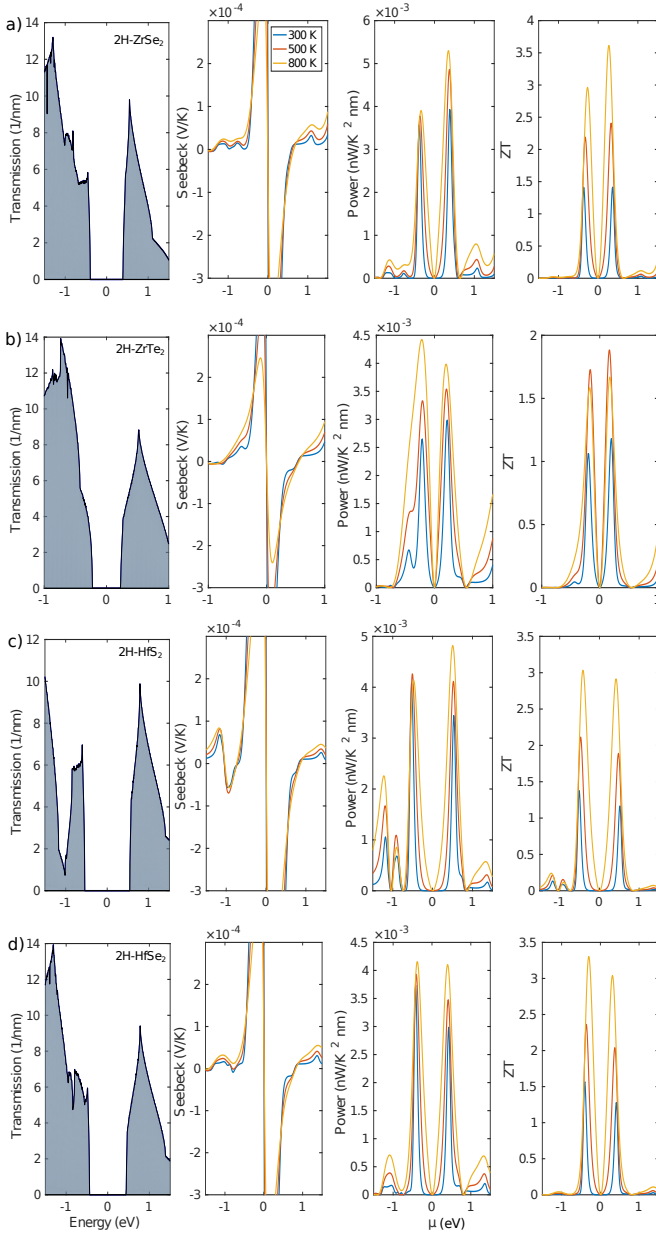


FIG. 6. Electronic transmission, Seebeck coefficient, power factor, and thermoelectric figure of merit are plotted around the Fermi level for 2H-ZrSe₂, 2H-ZrTe₂, 2H-HfS₂, and 2H-HfSe₂. Reproduced with permission from Physical Review B 100, 085415 (2019). Copyright 2019 American Physical Society.

electron and phonon transport in few-layered black phosphorus²²⁴ and suspended Bi₂Te₃ nanoplates²²⁵.

Cross-plane Seebeck coefficients of CVD-grown MoS₂, WS₂, and WSe₂ were also measured²²⁶. The Seebeck coefficients for MoS₂, WSe₂, and WS₂ thin films have been found to be approximately 115, 129, and 211 $\mu\text{V K}^{-1}$ at room temperature, respectively. Large differences in cross- and in-plane S values (115 mV K^{-1} /742 mV K^{-1}) were observed, which reveal the strong anisotropic behaviour of large-area MoS₂

with a ratio of 6.5 at 300 K. The trend was attributed to the energy filtering effect in the holey MoS₂ film through in-plane direction²²⁶. Experimentally obtained values of lattice TC and interface thermal conductance for 1L–3L structures are summarized in Table II.

In addition to the experimental studies, there have been extensive theoretical studies on the thermal properties of the monolayer, few-layer, hetero, and Janus structures of MoX₂ and WX₂ that performed different computational simulations and methods^{231–235}. The reported TC values notably differ from each other due to the difference in the simulation methods adopted in calculations. Furthermore, there have been reviews from different perspectives, as well^{124,236,237}.

Using the phonon BTE along with RTA, Wei *et al.* comprehensively explored the size and roughness dependency of phonon TC of monolayer MoS₂²³⁸. Since monolayer MoS₂ has short phonon MFP compared to graphene, its TC is weakly dependent on size and roughness. Monolayer MoS₂ exhibits lower TC compared to graphene²³⁹. The highest contribution to the TC comes from the LA phonon mode. The ZA phonon mode exhibits a relatively large contribution (33%) compared to the TA mode (7.5%). They also reported that the contributions of TA and ZA phonon modes are almost length-independent, while the LA mode is slightly dependent. The phonon TC of MoS₂ monolayer was also found as roughness-independent due to the short phonon MFP. The obtained TC value for monolayer MoS₂ was reported as 26.2 $\text{W m}^{-1} \text{K}^{-1}$. Using NEGF, Cai *et al.* investigated the lattice TC of MoS₂ monolayer with 18.1 nm phonon MFP as 23.2 $\text{W m}^{-1} \text{K}^{-1}$ at $T=300 \text{ K}$ ²⁴⁰. In addition, Cai *et al.* found lattice TC value as 6.66 $\text{W m}^{-1} \text{K}^{-1}$ by considering the phonon MFP value as 5.2 nm from MD calculation in the literature²⁴¹.

Since both bulk and monolayer forms of MoS₂ have not possessed very high ZT values, some researchers focused on TE properties of 1D MoS₂ armchair nanoribbons (aNRs). Liu *et al.*²⁴¹ performed MD simulations to investigate the TC of both MoS₂ monolayer and MoS₂ aNRs with 3.2 nm width. At room temperature, the calculated TC value of MoS₂ monolayer was reported as 1.35 $\text{W m}^{-1} \text{K}^{-1}$. They revealed that TC values of MoS₂ NRs are slightly dependent on the width and length of the material. The converged TC of MoS₂ aNRs was obtained as 1.7 $\text{W m}^{-1} \text{K}^{-1}$ when the sample size was considered long enough. Besides, TC of MoS₂ aNRs was reported as approximately 1.02 $\text{W m}^{-1} \text{K}^{-1}$ at room temperature. Using first-principles calculations and semi-classical Boltzmann theory as implemented in BoltzTraP code, Fan *et al.*²⁴² explored TE coefficients and ZT values of 1D MoS₂ aNRs with different width. They also obtained the relaxation time using DP theory. The Seebeck value of MoS₂ aNR with 4 ribbon width obtained as 224 $\mu\text{V/K}$ whereas aNR with 5 and 6 ribbon width exhibits higher Seebeck coefficients with a value of 727 and 640 $\mu\text{V/K}$, respectively. This difference originates from the band gap. The calculated band gap for 4-aNR was 0.15 eV, while 5-aNR and 6-aNR have 0.49 and 0.44 eV energy band gaps. By using the lattice TC value (1.02 $\text{W m}^{-1} \text{K}^{-1}$) from the literature²⁴¹, they reported the ZT value as 3.4 for p -type and 2.5 for n -type carriers of 4-aNR at room temperature. Since 5-aNR and 6-aNR have lower electrical con-

TABLE II. Experimentally determined TC and interfacial thermal conductance values of MoX₂ and WX₂ (X=S,Se)

Material	Method	supported	suspended (300 K)	suspended (500 K)	interfacial κ (MW/m ² K)	Refs.
Bulk MoS ₂	Pumb-probe		85-112			227
1L MoS ₂	Raman	55 +/- 20	84 +/- 17	66 +/- 16	0.44 +/- 0.07	218
	Raman		34.5 +/- 4			214
2L MoS ₂	Raman	35 +/- 7	77 +/- 25	29 +/- 10	0.74 +/- 0.05	218
4L MoS ₂	Micro-bridge		44-50			215
	Raman		60.3			228
6L MoS ₂	Raman		46			228
7L MoS ₂	Micro-bridge		48-52			215
8L MoS ₂	Raman		35.1			228
11L MoS ₂	Raman		52			213
1L MoSe ₂	Raman	24 +/- 11	59 +/- 18		0.09 +/- 0.03	218
2L MoSe ₂	Raman	17 +/- 4	42 +/- 13		0.13 +/- 0.03	218
1L WSe ₂	Raman	37 +/- 12	49 +/- 14		2.95 +/- 0.46	221
2L WSe ₂	Raman	24 +/- 12			3.45 +/- 0.50	221
3L WSe ₂	Raman	20 +/- 6			3.46 +/- 0.45	221
1L WS ₂	micro-Raman		32			217
2L WS ₂	micro-Raman		53			217
			28 ± 5			229
			38 ± 6			230
2L WS ₂ (2 μm length)			24 +/- 3			230
2L WS ₂ (5 μm length)			21 +/- 2.5			230

ductivity and PF than 4-aNR, they possess lower ZT values with a value of 0.8 for *p*-type and 1.3-1.7 for *n*-type carrier²⁴².

Li *et al.* performed first-principles calculations and employed BTE, and obtained the lattice TC of monolayer MoS₂ with a sample size of 1 μm as 83 W m⁻¹ K⁻¹ at T=300K²⁴³. Jin *et al.* investigated the electron and phonon transport properties of single-layer MoS₂ using first-principles calculations and equilibrium MD simulations²⁴⁴. TC value of single layer MoS₂ was reported as 116.8, 79.6, 52.9 W m⁻¹ K⁻¹ and the ZT value of *n*-type MoS₂ was predicted as 0.04, 0.07 and 0.11 at 300 K, 400 K, 500 K, respectively²⁴⁴. Gu *et al.* performed simulations to reveal the layer thickness dependency of TC for MoS₂ using first-principles-based Peierls-Boltzmann transport equation method¹¹⁶. They concluded that the TC value decreases as the thickness of the MoS₂ layer increases. They predicted the room temperature lattice TC value of naturally occurring and isotopically pure bulk MoS₂ as 94 W m⁻¹ K⁻¹ and 112 W m⁻¹ K⁻¹, respectively. As the thickness goes from 1L to 3L, lattice TC of naturally occurring MoS₂ takes values from 138 W m⁻¹ K⁻¹ to 98 W m⁻¹ K⁻¹ whereas isotopically pure MoS₂ has TC values ranging from 155 W m⁻¹ K⁻¹ to 115 W m⁻¹ K⁻¹. From these results, it can be clearly stated that the lattice TC value of 3L MoS₂ is quite close to that of bulk structure.

Using ShengBTE code, Gandhi *et al.* obtained the lattice TC value of bulk and monolayer MoS₂ as 2.3 and 131 W m⁻¹ K⁻¹ at T=300 K, respectively²⁴⁵. Afterwards, Hong *et al.*²⁴⁶ predicted the lattice TC of MoS₂ and MoSe₂ as 110.43 and 43.88 W m⁻¹ K⁻¹ by performing MD simulations. Peng *et al.*²⁴⁷ carried out first-principles calculations to investigate the lattice TC of monolayer MoS₂, MoSe₂, and WS₂ and they

reported the TC value at room temperature as 33.6 W m⁻¹ K⁻¹, 17.6 W m⁻¹ K⁻¹ and 31.8 W m⁻¹ K⁻¹, respectively. Ge *et al.* calculated the lattice TC and ZT value of 1T'' phase of MoSe₂ as 10.7 W m⁻¹ K⁻¹ and ~ 0.2 at room temperature using Slack model⁹⁵.

Huang *et al.* investigated TE performance of monolayer MoX₂ and WX₂ (X=S, Se) by using 2D ballistic transport approach based on energy dispersions²⁴⁸. They reported the Seebeck coefficient, electrical conductance, and thermal conductance contributed by electrons, lattice thermal conductance, and ZT parameters for *p*-type and *n*-type charge carriers. For both *p*-type and *n*-type, the considered monolayers possess similar ZT values at low temperature values. They reported that *p*-type MoS₂ has higher ZT with a value of 0.58 at around 300 K whereas *n*-type WSe₂ possess high ZT value compared to MoS₂, MoSe₂, WS₂ at high temperature values above 300 K. Besides, *n*-type MoS₂ exhibits lower room temperature ZT with a value of 0.25.

Using ballistic transport approach, Huang and co-workers²⁴⁹ examined the thickness dependence of TE properties of layered MoS₂ and WSe₂ structures, since the TC values of MoS₂ films and disordered WSe₂ demonstrated as low as 0.1-1 W m⁻¹ K⁻¹ and 0.05 W m⁻¹ K⁻¹, respectively^{250,251}. They revealed out that the maximum ZT value for *n*-type 1L-MoS₂ and 2L-WSe₂ can reach 1.6 and 2.1 at 500 K, respectively²⁴⁹.

Wickramaratne *et al.* explored the TE properties of MX₂ (M=Mo, W; X=S, Se) with different number of layers using first principles calculations and Landauer formalism²⁵². To calculate TE parameters for each material, they took into account the experimentally reported lattice TC values²¹⁴ as

34.5 W m⁻¹ K⁻¹ for monolayer and 52 W m⁻¹ K⁻¹ for few layered structures. Among considered materials and different layer thicknesses, TE performance of *n*-type 2L-MoSe₂ possess the highest value (2.39) at room temperature. For 2L thickness, this maximum value is followed by *n*-type 2L-WS₂ with a value of 1.98. In addition, they found that *p*-type bilayer MoS₂ exhibits the highest ZT value (1.15 at T=300 K) among the considered layered materials.

In a recent study, Jobayr *et al.*²⁵³ investigated the TE properties of both bulk and monolayer structures of MoS₂, MoSe₂, WS₂ and WSe₂ using BTE. By taking into account phonon TC values as 0.245 (MoS₂), 0.18 (MoSe₂), 0.212 (WS₂), and 0.164 (WSe₂) W m⁻¹ K⁻¹ from the previous work reported by Huang *et al.*²⁴⁸, they calculated the ZT values of *n*-type charge carrier concentration for MoS₂, MoSe₂, WS₂ and WSe₂ at room temperature as 2.2147, 2.2859, 2.8729, and 2.9191, respectively. It can be concluded that WS₂ and WSe₂ exhibit a competitive ZT values.

Kumar *et al.*¹⁸ comprehensively investigated the TE properties of both bulk and monolayer MoSe₂ and WSe₂ using BoltzTraP and ShengBTE codes. Due to their calculation results, they predicted that monolayer MoSe₂ and WSe₂ has lower Seebeck coefficient (427 and 350 μ V/K) in comparison to their bulk counterparts (690 and 680 μ V/K). They determined the relaxation time by taking into account experimental hole conductivity values of undoped materials^{254,255} and predicted σ/τ values at room temperature. As a result, they reported the in-plane and out-of-plane relaxation times as 1.6×10^{-13} s and 1.4×10^{-15} s for WSe₂, and 5.7×10^{-15} s and 8.0×10^{-17} s for MoSe₂, respectively. The lattice TC value of monolayer WSe₂ was predicted as lower than that of monolayer MoSe₂. Both *p*-type and *n*-type WSe₂ has higher ZT value compared to MoSe₂¹⁸.

Zhou and Chen²⁵⁶ obtained lattice TC of WSe₂ monolayer using DFT and the linearized phonon BTE within RTA. They reported that WSe₂ monolayer (1 μm sample size) exhibits ultralow TC with a value of 3.935 W m⁻¹ K⁻¹ compared to MoS₂, MoSe₂, WS₂ monolayers. In literature, TC values of MoS₂ monolayer with 1 μm sample size were reported as 83 and 103 W m⁻¹ K⁻¹ using BTE^{15,243}. In addition, TC value for MoS₂ monolayer predicted as 23.3 W m⁻¹ K⁻¹ using NEGF²⁵⁷. Moreover, Zhang *et al.* performed first-principles calculations within BTE to explore TCs of honeycomb MX₂ (M = Cr, Mo, W; X = O, S, Se, Te) monolayers²⁵⁸. As an overall evaluation, they revealed out that as the mass of atom M or X increases, the lattice TCs of MX₂ monolayers decrease. On the other hand, when M varies from Cr to W, lattice TCs of sulfides and selenides (MX₂; M = Cr, Mo, W; X=S,Se) increase. With further analysis, they pointed out that the trend in the lattice TC mostly originates from the phonon relaxation time. Zhang *et al.*²⁵⁸ explored the length dependency of lattice TC of considered MX₂ monolayers with width d = 5 μm at room temperature. The lattice TC of TM oxides increases rapidly with length and is more dependent on length than compared to TM sulfides and selenides, except WS₂. The reported TC values at L=15 μm for oxides (MO₂; M=Cr, Mo, W) are 236.2 (CrO₂), 209.6 (MoO₂), 157.5 (WO₂) W m⁻¹ K⁻¹, for sulfides are 88.8 (CrS₂), 82.2 (MoS₂), 121.2

(WS₂) W m⁻¹ K⁻¹. The lattice TC values for selenides and tellurides has smaller values compared to oxides and sulfides. CrSe₂, MoSe₂ and WSe₂ exhibit 35.3, 46.2, 72.7 W m⁻¹ K⁻¹ TC values while CrTe₂, MoTe₂ and WTe₂ possess 27.9, 41.4 30.2 W m⁻¹ K⁻¹, respectively.

Gu and Yang¹¹⁵ studied the phonon transport properties of both 2H- and 1T-type MX₂ (M=Mo, W, Zr, and Hf, X=S and Se) monolayers using first-principles calculations within iterative solution of Peierls-Boltzmann transport equation and also from single-mode RTA. The lattice TC value of MoS₂ was predicted as 103 W m⁻¹ K⁻¹ from iterative solution of Peierls-Boltzmann transport equation whereas the value reported as 83 W m⁻¹ K⁻¹ using single-mode RTA. Among the considered monolayers, WS₂ has the largest TC and the calculated value from Peierls-Boltzmann transport equation was 141.8 W m⁻¹ K⁻¹ at T=300 K. For MoS₂, MoSe₂ and WSe₂, lattice TC was reported as 103.3 W m⁻¹ K⁻¹, 54.3 W m⁻¹ K⁻¹ and 52.6 W m⁻¹ K⁻¹ at T=300 K, respectively. In addition, they also obtained TC of MoS₂ performing MD simulations, and the result is lower in comparison to first-principles calculations. They pointed out that, for the same sample size of 1 μm, 1T-type MX₂ monolayers possess lower lattice TC values than 2H-type MX₂ monolayers.

Ma *et al.* explored the ballistic thermal transport properties of MoX₂, WX₂ (X=S, Se) monolayers²⁵⁹. For low temperature values (~ below 50 K), thermal conductance of MX₂ (M=Mo, W; X=S, Se) tends to increase with increasing atomic mass. Besides, it has a tendency to decrease with atomic mass for high temperature values. They pointed out that it is possible to control the thermal conductance by the atomic mass efficiently.

Ballistic electronic and phononic transport properties of semiconducting 2D TMDs and TMDOs (MX₂ with M = Cr, Mo, W, Ti, Zr, Hf; X = O, S, Se, Te) both in 2H and 1T phases comprehensively explored using first-principles calculations within Landauer-Büttiker formalism by Özbal *et al.*⁵¹. They pointed out that mostly TM tellurides in 2H phase exhibit lower phonon thermal conductance compared to TM oxides, sulfides, and selenides at all considered temperature values (T=300 K, 500 K, and 800 K). According to their calculation results, CrO₂ exhibits the highest phonon thermal conductance with a value of 2.09 W m⁻¹ K⁻¹ at room temperature. For most of the considered 2D TMDs and TMDOs, phonon thermal conductance slightly increases with increasing temperature. Due to high vibrational frequency, the phonon thermal conductance of TMDOs has a remarkable increase with rising temperature. In general, TM oxides have higher phonon thermal conductance compared to sulfides, selenides, and tellurides. Therefore, TM oxides are the materials with the lowest ZT value among the materials studied. At room temperature, *p*-type 2H-MX₂ (M=Cr, Mo, W; X=S, Se, Te) possess ZT value in the range from 0.33 to 0.55. For *n*-type charge carriers, ZT has values between 0.27-0.54. Both *p*-type and *n*-type ZT values of these materials enhanced to higher than 1 when temperature is increased to T=800 K. Besides, it was revealed out that ZT values of *n*-type MoSe₂ (1.91), MoTe₂ (2.21), WSe₂ (2.18) and *p*-type MoTe₂ (1.85) are high enough to be considered. All the detailed results for phonon thermal

conductance and ZT values are given in Tables III-IV.

Since strain, vacancy, defects, and doping have remarkable impact on TC and hence ZT of graphene^{260–262} and silicene^{263,264}, researchers explored the influence of lattice defects and/or strain on TE properties of monolayer and/or few layer MoS₂, MoSe₂, WS₂ as well^{117,265–273}. Under compressive and tensile strain, TE coefficients for monolayer MoS₂ were obtained by considering SOC effect²⁷⁴. Since SOC extinguish the band degeneracy, it leads to an enhancement in the PF and PF has larger values compared to the case where the SOC effect is not taken into account. For MoS₂ monolayer, SOC causes an improvement for *n*-type carrier concentration while it decreases PF of *p*-type carrier concentration. Strain also has a significant impact on the power factor^{265,266}.

Bera and Sahu investigated the both uniaxial and biaxial strain effect on TE performance of monolayer WS₂ using Phono3py code²⁶⁷. For strain-free case, room temperature lattice TC of WS₂ monolayer was reported as 72 W m⁻¹ K⁻¹. At higher temperature values (T=900 K), ZT value has its maximum and the calculated value was reported as 0.516 for *n*-type and 0.494 for *p*-type WS₂ monolayer. With the effect of applied 2% biaxial compressive strain, ZT value of *n*-type WS₂ increases to 0.700 while it has its maximum value (0.720) for applied 4% uniaxial compressive strain. For 2% biaxial tensile strain and 4% uniaxial tensile strain, ZT values of *p*-type WS₂ reported as 0.550 and 0.568, respectively, at T=900K.

Han *et al* calculated the biaxial strain effect on lattice TC of WS₂ monolayer using ShengBTE code²⁷⁵. For unstrained case, they reported the lattice TC value as 262.78 W m⁻¹ K⁻¹. For 8% biaxial tensile strain its value reduces to 190.66 W m⁻¹ K⁻¹ while WS₂ monolayer has 217.40 W m⁻¹ K⁻¹ lattice TC under the effect of -4% biaxial compressive strain.

Ding *et al.* explored the TC of both pristine and defective MoS₂ under the influence of strain using NEMD simulations²⁶⁸. Mo (S) vacancy defect as small as 0.5% changes the TC significantly by 60% (35%). With the effect of 12% tensile strain, TC of defected MoS₂ decreases by 60% and TC of pristine MoS₂ also decreases almost at the same rate. Peng *et al.* studied the effect of Sulfur vacancies on thermal transport properties of monolayer MoS₂ using ShengBTE code²⁶⁹. They reported the room temperature κ_L value for pure MoS₂ and MoS₂ with monosulfur vacancy defect as 154.3 W m⁻¹ K⁻¹ and 62.1 W m⁻¹ K⁻¹, respectively. For MoS₂ with disulfur vacancy ($\kappa_L=38.2$ W m⁻¹ K⁻¹) and double monosulfur vacancy ($\kappa_L=40.2$ W m⁻¹ K⁻¹) defects, room temperature κ_L values were predicted as lower than those of pure and monosulfur vacancy defect due to decreasing phonon group velocities and increasing three-phonon Umklapp scattering. Sharma *et al.* pointed out that MoS₂ monolayer with Sulfur vacancy defect exhibits higher figure of merit ($ZT = 6.24$) compared to MoS₂ monolayer in pristine form at room temperature²⁷¹. In addition, room temperature ZT value for MoS₂ monolayer with MoS₂ vacancy defect was predicted as 1.30. The reported ZT values of MoS₂ monolayer in the literature is in the range from 0.02 to 0.53 (Table III).

The effect of W doping in pristine MoSe₂ and also defected MoSe₂ with Se vacancy was investigated by Yan *et al* using phonon BTE²⁷⁰. They found out that Se vacancy leads to a

decrease in lattice TC of MoSe₂ monolayer. MoSe₂ monolayer with Se vacancy rate of 1%, 2% and 4% exhibits 27.7%, 39.5% and 51.9% lower lattice TC values compared to pristine MoSe₂ monolayer. On the other hand, it was reported that lattice TC of W doped pristine MoSe₂ with a sufficiently large size has a remarkable increase (23.6 %) whereas W doping in defective MoSe₂ caused a decrease in lattice TC. Furthermore, they also revealed out that room temperature lattice TC has 34.0 % and 46.2 % lower values when Se vacancy defect with a rate of 1% and 2% applied to the W doped MoSe₂, respectively.

Although various ways to tune TC of 2D materials have been theoretically successful, it is difficult to achieve this experimentally due to various technical challenges. Phonon transport properties of few-layer MoS₂ flakes with defects were studied experimentally using different techniques^{276,277}. Aiyiti *et al.*²⁷⁶ measured the TC of MoS₂ by applying a novel approach i.e., mild oxygen plasma. A crystalline–amorphous transition emerges under high-dose plasma with a sharp change in TC. They exfoliated three different samples, namely MoS₂-A, MoS₂-B and MoS₂-C, from the bulk MoS₂ and determined the room temperature TC values as 30 ± 3 W m⁻¹ K⁻¹, 34 ± 5 W m⁻¹ K⁻¹ and 31 ± 4 W m⁻¹ K⁻¹, respectively. According to their NEMD calculations, for 5% defect concentration, the TC value of the defective structure was obtained as 55% lower than the pristine structure²⁷⁶. Zhao *et al.* performed helium ion (He+) irradiation to explore the TC of defected few-layer MoS₂ flakes²⁷⁷. They estimated the TC values for two few-layer MoS₂ flakes as 38 ± 6 and 28 ± 5 W m⁻¹ K⁻¹. In order to create a defect in the crystal structure, the irradiation dose has been increased continuously. They reported that both Mo-vacancy and S-vacancy cause a decrease in TC value.

Guo comprehensively explored phonon transport properties of Janus MoSSe monolayer using linearized phonon BTE within the single-mode RTA²⁷⁸. At room temperature, the predicted value of thermal sheet conductance of MoSSe Janus monolayer is 342.50 W K⁻¹ which is higher than that of ZrSSe monolayer (33.6 W K⁻¹)²⁰⁷. This difference results from the difference in the phonon dispersions. Furthermore, they reported that lattice TC value of MoSSe Janus monolayer (13.90 W m⁻¹ K⁻¹) is in the range of MoS₂ (23.15 W m⁻¹ K⁻¹) and MoSe₂ (11.54 W m⁻¹ K⁻¹) monolayers.

By calculating TE coefficients using BoltzTraP code and considering lattice TC of MoS₂ as reported in literature²⁴⁰ ($\kappa_L = 23.2$ W m⁻¹ K⁻¹ at T=300 K), Vallinayagam *et al.* obtained the TE figure of merit of MoS₂ monolayers with substitution of S by Se and SeMoS Janus layer²⁷⁹. For MoS₂ monolayers with substitution of S by Te and TeMoS Janus layer, lattice TC value of monolayer MoTe₂ has been taken into account from the literature²⁸⁰ as 42.2 nW K⁻¹ at T=300 K. They calculated the ZT value for Se substituted MoS₂ monolayers at T=300 K as ~ 1.0 . Te substituted MoS₂ monolayers possess a little lower ZT values compared to Se substituted monolayers. In addition, SeMoS Janus layer exhibits a ZT value around ~ 1.0 -1.02 while ZT value of TeMoS Janus layer has ~ 0.84 -0.86. TE performance of WS₂ and Janus WSSe and WSTe monolayers obtained by Patel *et al.* using BoltzTrap2 code²⁸¹.

They reported that Janus WSTe monolayer possess higher ZT value than WS₂ (ZT=0.006) and Janus WSSe monolayer (ZT=0.013) with a value of 0.74 at T= 300 K. For higher temperature values (T=1200 K), ZT value of Janus WSTe monolayer increases to 2.56.

Chaurasiya *et al.* obtained the strain effect on TE properties and lattice TC of Janus WSSe monolayer by using BoltzTraP package and Phono3py code²⁸². For strain-free case, Janus WSSe monolayer has a lattice TC value of 25.37 W m⁻¹ K⁻¹ at room temperature which is lower than WSe₂ and MoSe₂¹¹⁵. Under the effect of tensile strain, TC value of WSSe monolayer reduces to 9.90 W m⁻¹ K⁻¹. At T=1500 K, calculated ZT of unstrained WSSe was reported as 0.72 (0.73) for *n* (*p*)-type carriers. They pointed out that the ZT value of *n* (*p*)-type WSSe significantly increases to 1.06 (1.08) with the effect of biaxial strain.

Zhang *et al.* investigated the phonon thermal properties of MoS₂/MoSe₂ heterobilayer by performing NEMD simulations²⁸³. They reported the TC value of MoS₂, MoSe₂, and MoS₂/MoSe₂ bilayer 2D sheet as 32.9, 24.8, and 28.8 W m⁻¹ K⁻¹ at room temperature, respectively. Using ShengBTE code, Ma *et al.*²⁸⁴ obtained the lattice TC value of MoS₂/MoSe₂ bilayer heterostructure. They revealed out that the lattice TC value of MoS₂/MoSe₂ bilayer heterostructure is around 25.39 W m⁻¹ K⁻¹ at room temperature. This value lies between calculated TC values of its monolayer counterparts MoS₂ (39.61²⁸⁴ and 33.6²⁴⁷ W m⁻¹ K⁻¹) and MoSe₂ (17.55²⁸⁴ and 17.6²⁴⁷ W m⁻¹ K⁻¹) reported in the relevant article and also literature.

Deng *et al.* comprehensively examined the TE performance of monolayer and bilayer MoSSe nanoribbons and also graphene/MoSSe heterostructure nanoribbons using NEGF and the Landauer equation²⁸⁵. According to their calculation results, at T=300 K, bilayer MoSSe nanoribbons exhibits ultralow lattice TC with a value of 0.012 nW K⁻¹ and this value followed by graphene/SeMoS stacked nanoribbons (0.045 nW K⁻¹), graphene/SMoSe stacked nanoribbons (0.067 nW K⁻¹), symmetric armchair MoSSe nanoribbons (0.077 nW K⁻¹). Room temperature ZT value for *n*-type graphene/SeMoS (*p*-type graphene/SMoSe) stacked nanoribbons reported as 2.01 (1.16) which is higher (lower) than that of symmetric armchair MoSSe nanoribbons (*p*-type ZT=1.64) and bilayer MoSSe nanoribbons (*n*-type ZT=1.28). It can be concluded that these nanoribbon structures exhibits better TE performance compared to graphene, MoS₂ monolayer and Janus MoSSe monolayer structures^{248,279}.

Zhang *et al.* explored the lateral and out-of-plane (interfacial) lattice TC of bilayer MoS₂ and WS₂, heterobilayer MoS₂/WS₂ and superlattice MoS₂/WS₂ by iteratively solving phonon BTE as implemented in ShengBTE package²⁸⁶. At room temperature, lateral κ_L values of bilayer MoS₂ and WS₂ were obtained as 61.13 W m⁻¹ K⁻¹ and 87.52 W m⁻¹ K⁻¹, respectively, which are compatible with the experimental results^{217,218}. At T=500 K, bilayer MoS₂ has lower lateral κ_L with a value of 36.77 W m⁻¹ K⁻¹. For heterobilayer MoS₂/WS₂, lateral κ_L was reported as 70.01 W m⁻¹ K⁻¹ and this value is in the range of bilayer MoS₂ and WS₂ structures. Moreover, superlattice MoS₂/WS₂ possess much more lower

lateral κ_L with a value of 7.22 W m⁻¹ K⁻¹ than monolayer, bilayer and heterobilayer structures due to decreasing phonon relaxation time.

Using NEMD method, Zhang *et al.*²⁸⁷ explored the phonon thermal properties of MoS₂-MoSe₂, MoS₂-WS₂, and MoS₂-WSe₂ heterobilayers. They investigated the dependence of lattice TC on the width and length of the related material. It is concluded that while the TC value for different widths remains almost unchanged, the TC value increases monotonically as the length increases. For a sufficiently high length value (> 400 nm), the TC value begins to converge. The reported TC values for MoS₂-MoSe₂, MoS₂-WS₂, and MoS₂-WSe₂ heterobilayers as follows; 34.1 W m⁻¹ K⁻¹, 68.9 W m⁻¹ K⁻¹, and 33.0 W m⁻¹ K⁻¹, respectively.

Bharadwaj *et al.*²⁸⁸ investigated the TE performance of heterostructures consisting of possible combinations of MoS₂, MoSe₂, WS₂, and WSe₂ at different temperatures (T=300 K, 500 K, 800 K) by performing quantum transport calculations combined with Boltzmann transport theory. They reported the heterostructures with notable room-temperature ZT values as *n*-type WS₂/WSe₂ (0.997) and *p*-type MoSe₂/WSe₂ (0.714). At higher temperature values (T=800 K), *n*-type WS₂/WSe₂ (1.806) and *n*-type WS₂/MoS₂ (1.641), *p*-type MoS₂/MoSe₂ (1.289) and *p*-type MoSe₂/WSe₂ (1.045) exhibit highest ZT values compared to considered heterostructured materials.

The room temperature lattice TC value of WSe₂/WTe₂ heterostructure was reported as 70.694 W m⁻¹ K⁻¹ at T=300 K by Luo *et al.*²⁸⁹ using ShengBTE code. This value is larger than that of some TMDs such as MoSe₂ (54.3 W m⁻¹ K⁻¹) and WSe₂ (52.6 W m⁻¹)¹¹⁵. Moreover, Chang *et al.*²⁹⁰ determined the phonon thermal transport properties of WS₂/WSe₂ heterostructures by employing ShengBTE code. They reported that WS₂/WSe₂ heterostructure has lattice TC value of 62.98 W m⁻¹ K⁻¹ at T=300 K. It can be stated that this value falls between the calculated lattice TC values of WS₂ (101.74 W m⁻¹ K⁻¹) and WSe₂ (46.8 W m⁻¹ K⁻¹) monolayers.

Han *et al.* performed calculations to investigate TE properties of WS₂, WSe₂ monolayers, and WS₂-WSe₂ phononic crystals at different temperatures using BoltzTraP code and ShengBTE package⁴³. At T=300 K, the lattice TC value of WS₂ and WSe₂ monolayers obtained as 299.87 W m⁻¹ K⁻¹ and 120.86 W m⁻¹ K⁻¹. For WS₂-WSe₂ phononic crystals, superlattices with the smallest period length (SL1) and the second smallest period length (SL2), the lattice TC values were reported as notably low compared to monolayered structures. Through *x* (*y*)-direction, they obtained that SL1 and SL2 have anisotropic lattice TC with a value of 69.95 W m⁻¹ K⁻¹ (75.06 W m⁻¹ K⁻¹) and 46 W m⁻¹ K⁻¹ (53.52 W m⁻¹ K⁻¹), respectively. They also predicted the ZT values for both monolayers and phononic crystals superlattices. At T=1000 K, *p*-type WS₂ and WSe₂ monolayers exhibit the highest TE performance with a ZT value of 0.43 and 0.37, respectively. Furthermore, the ZT values of *p*-type SL1 and SL2 monolayers were reported as 0.95 (0.67) and 0.62 (0.66) through the *x* (*y*)-direction at 1000 K.

TE transport properties of WS₂ /WSe₂ lateral superlattice were studied by Hu *et al.*¹⁷² using BoltzTraP and ShengBTE codes. They also calculated relaxation time by employing the

DP theory. For p -type (n -type) WS_2 / WSe_2 , τ was reported as 40.77×10^{-14} s (2.71×10^{-14} s) and 38.78×10^{-14} s (2.92×10^{-14} s) along xx and yy direction, respectively. The lattice TC was obtained as 16.9 (4.5) $\text{W m}^{-1} \text{K}^{-1}$ through xx (yy) direction. For WS_2 monolayer, lattice TC had values 33.8 $\text{W m}^{-1} \text{K}^{-1}$ and 9.2 $\text{W m}^{-1} \text{K}^{-1}$ through xx and yy direction, respectively. They predicted the ZT value as 0.28 (0.68) for p -type through xx (yy) direction at $T=300$ K.

Zhao *et al.* obtained the biaxial strain effect on TE performance of MoS_2/WS_2 heterostructure by using BoltzTraP package and DP theory²⁹¹. They calculated the strain dependence of lattice TC by performing NEMD simulations. For the strain-free case, the predicted values of lattice TC were 68.44 $\text{W m}^{-1} \text{K}^{-1}$ and 42.81 $\text{W m}^{-1} \text{K}^{-1}$ at $T=300$ K and $T=500$ K, respectively. The obtained results are compatible with previous work reported by Zhang *et al.*²⁸⁷. With the effect of applied biaxial strain, lattice TC value decreases due to change in the phonon scattering, and correspondingly ZT value increases. According to their calculation results, the ZT value of n -type charge carriers has doubled compared to the case without strain effect. For p -type charge carriers, the ZT value increased by 50% compared to the strain-free case.

C. PdX_2 , PtX_2 ($X=\text{S, Se, Te}$)

Due to their widely tunable bandgap, moderate carrier mobility, anisotropy, and ultrahigh air stability, group-X noble TMDs PdX_2 , PtX_2 ($X=\text{S, Se, Te}$) have also been the subject of tremendous attention²⁹². Various experimental and theoretical studies have been carried out to explore the structural, electronic, and optical properties of these materials^{292–297}. As a result of the comprehensive analysis, they have been proposed as potentially good candidates for field effect transistors^{298,299}, photodetectors^{300,301}, catalysis^{302,303}, and sensors^{304,305}. PtTe_2 , PdTe_2 , PtSe_2 , and PtS_2 are thermodynamically stable in trigonal structure³⁰⁶ whereas PdS_2 and PdSe_2 are most stable in orthorhombic pentagonal structure^{293,307}.

In literature, various researchers theoretically investigated the TE properties of monolayer penta- PdX_2 ($X=\text{S, Se, Te}$) and the anisotropy in TE coefficients of these materials using first-principles calculations and BTE within the RTA and CRTA as implemented in the BoltzTraP software^{44,308,309}. Due to the structural anisotropic nature of these monolayers, transport coefficients (σ/τ , $S^2\sigma$, κ_L , κ_e , ZT) possess strong anisotropy along both x and y directions. Using ShengBTE code, Lan *et al.*³⁰⁹ investigated the anisotropy in κ_L and reported κ_{Lx}/κ_{Ly} as ~ 0.34 , 0.43 , and 0.24 at $T=300$ K for penta- PdS_2 , PdSe_2 , PdTe_2 , respectively. Individual values of κ_L along x - and y -directions have been reported as 4.34 and 12.48 $\text{W m}^{-1} \text{K}^{-1}$ for PdS_2 , 2.91 and 6.62 $\text{W m}^{-1} \text{K}^{-1}$ for PdSe_2 , 1.42 and 5.90 $\text{W m}^{-1} \text{K}^{-1}$ for PdTe_2 , respectively. Qin *et al.*⁴⁴ reported the lattice TC values of PdSe_2 along x - and y -directions as 3.7 (1.4) and 7.2 (2.7) $\text{W m}^{-1} \text{K}^{-1}$ at $T=300$ K (800 K), respectively. For different carrier concentration types and different directions, PdTe_2 has higher electrical conductivity, PF and lower κ_L compared to PdS_2 and PdSe_2 ^{44,308,309}. Therefore, it can be stated that the ZT value of PdTe_2 will be higher along

relevant directions. The maximum ZT values along the x -direction for p -type penta- PdS_2 , PdSe_2 and PdTe_2 are reported as 0.85 , 1.18 , and 2.42 at carrier concentration 3.34×10^{13} , 7.08×10^{12} , and $3.78 \times 10^{13} \text{ cm}^{-2}$, respectively³⁰⁹. The calculated ZT value for p -type PdSe_2 along x -direction is 1.1 at room temperature⁴⁴. So, the results clearly demonstrate that each relevant material is a potential anisotropic TE candidate.

Marfoua and Hong examined the TE properties of hexagonal and pentagonal PdTe_2 structures using semiempirical Wiedemann–Franz law and BTE⁴¹. Since the empirical Wiedemann–Franz law underestimated the electronic TC, it may be possible for ZT to have a higher value³¹⁰. Marfoua and Hong⁴¹ estimated the ZT value as high as 3 with Wiedemann–Franz approach. At $T=300$ K, they reported the lattice TC of hexagonal PdTe_2 as 3.20 and 3.23 $\text{W m}^{-1} \text{K}^{-1}$ along zigzag and armchair directions, respectively. Moreover, lattice TC of pentagonal PdTe_2 obtained as 0.53 (1.21) $\text{W m}^{-1} \text{K}^{-1}$ along the x (y)-direction at $T=300$ K. Overall, pentagonal PdTe_2 exhibits lower lattice TC than hexagonal PdTe_2 . Both pentagonal (along x - and y -direction) and hexagonal (along zigzag direction) structures of n -type PdTe_2 possess nearly the same ZT (around ~ 0.7 - 0.75) at $T=300$ K. On the other hand, n -type pentagonal PdTe_2 exhibits better TE performance compared to hexagonal PdTe_2 at temperature values higher than 500 K. Along the armchair direction, the maximum ZT value of n -type hexagonal PdTe_2 obtained as 0.59 , 0.69 and 0.67 $\text{W m}^{-1} \text{K}^{-1}$ at $T=300$ K, 500 K and 700 K, respectively⁴¹. For both zigzag and armchair directions, n -type PdTe_2 shows better TE performance than p -type PdTe_2 . Along the x -direction, the ZT value of n -type pentagonal PdTe_2 reported as 0.7 (0.85) at 300 K (700 K) while n -type pentagonal PdTe_2 exhibits 0.8 (0.91) at 300 K (700 K)⁴¹. Here again, the future potential of these materials is clear.

Zhong *et al.*³¹¹ examined the TE coefficients and TE performance of 2D hexagonal MX_2 ($M=\text{Ni, Pd}$; $X=\text{S, Se and Te}$) using first-principles calculations and BoltzTraP code. The reported κ_L values for H- PdS_2 , H- PdSe_2 , H- PdTe_2 and H- NiSe_2 are 35.87 , 11.52 , 1.30 and 1.08 $\text{W m}^{-1} \text{K}^{-1}$ at 300 K, respectively. Since H- PdTe_2 and H- NiSe_2 have lower κ_L values, they investigated the ZT values for these materials by considering different electronic scattering times (3 fs, 5 fs, 7 fs, and 9 fs). They revealed out that ZT value of n -type H- PdTe_2 is smaller (0.24 at $\tau = 5$ fs) compared to n -type H- NiSe_2 (0.38 at $\tau = 5$ fs) at room temperature. For different electronic scattering time values such as 3 fs, 7 fs, and 9 fs, ZT value of H- PdTe_2 (H- NiSe_2) was predicted as 0.15 (0.25), 0.31 (0.48), and 0.38 (0.58), respectively. When the temperature increases to 700 K, maximum ZT values obtained as 1.08 for n -type H- PdTe_2 and 0.61 for H- NiSe_2 at $\tau = 5$ fs. These results clearly show that the potential of Pd-based materials is differentiable.

As a strategy to tune the TE properties, strain engineering is also applied these materials. Lan *et al.*³¹² explored the strain dependence of lattice TC of PdS_2 monolayer. For unstrained PdS_2 , the in-plane TC was obtained as 32.32 $\text{W m}^{-1} \text{K}^{-1}$ at room temperature³¹². When the biaxial strain ratios increases from 0% to 10% , the lattice TC value significantly decreases and it has value of 26.03 $\text{W m}^{-1} \text{K}^{-1}$ for 10% strain ratio (reduced by 19.5%) at room temperature. Zhang *et al.*³¹³ used

TABLE III. Lattice thermal conductivity (conductance) and ZT values of CrX_2 , MoX_2 , and W_2 ($X=\text{S,Se,Te}$) at room temperature.

Material	Phase (1T/2H)	Theoretical Method (Tool)	κ_L ($\text{Wm}^{-1}\text{K}^{-1}$)	ZT		ZT_{max}		Refs.
				n -type	p -type	n -type	p -type	
CrS_2	2H	Landauer	1.24 (conductance per width)	0.27	0.33	1.02@800 K	1.40@800 K	51
CrSe_2	2H	Landauer	0.83 (conductance per width)	0.4	0.41	1.49@800 K	1.59@800 K	51
CrTe_2	2H	Landauer	0.60 (conductance per width)	0.54	0.55	1.59@800 K	1.70@800 K	51
MoS_2	2H	Landauer	1.03 (conductance per width)	0.22	0.47	0.97@800 K	1.46@800 K	51
MoS_2 -Bulk	2H	Landauer		0.35	0.081			252
MoS_2 -1L	2H	Landauer		1.35	0.97			252
MoS_2 -1L	2H	Landauer				1.6@500 K		249
MoS_2 -2L	2H	Landauer		1.35	1.15			252
MoS_2 -3L	2H	Landauer		2.23	0.51			252
MoS_2 -4L	2H	Landauer		1.78	0.39			252
MoS_2	2H	BTE (BoltzTraP)	116.8@300 K	0.04				244
			79.6@400 K			0.07@400 K		244
MoS_2	2H	BTE (BoltzTraP)	52.9@500 K			0.11@500 K		244
MoS_2	2H	Landauer		0.25	0.58			248
MoS_2	2H	BTE		2.2147				253
MoS_2 (4-aNR)	2H	BTE (BoltzTraP)		2.5	3.4			242
MoS_2 (5-aNR)	2H	BTE (BoltzTraP)		1.3	0.8			242
MoS_2 (6-aNR)	2H	BTE (BoltzTraP)		1.7	0.8			242
MoS_2 -(1-Nb,2-Te)	2H	BTE (BoltzTraP)		0.88	1.1	1.2@1200 K	1.04@1200 K	279
MoS_2 -(1-Nb,4-Te)	2H	BTE (BoltzTraP)		1	1	1.40@1200 K	1.06@1200 K	279
MoSe_2	2H	Landauer		0.37	0.39			248
MoSe_2	1T''	BTE (BoltzWann)	10.7@300 K	0.2				95
MoSe_2	2H	BTE (BoltzTraP)		2.2859				253
MoSe_2	2H	BTE (BoltzTraP)				0.1@1200 K	0.07@1200 K	18
MoSe_2	2H	Landauer	0.72 (conductance per width)	0.35	0.38	1.91@800 K	1.38@800 K	51
MoSe_2 -1L	2H	Landauer		1.39	0.8			252
MoSe_2 -2L	2H	Landauer		2.39	0.81			252
MoSe_2 -3L	2H	Landauer		1.66	0.81			252
MoSe_2 -4L	2H	Landauer		1.65	0.81			252
MoSe_2 -Bulk	2H	Landauer		0.29	0.081			252
MoTe_2	2H	Landauer	0.54 (conductance per width)	0.46	0.51	2.21@800 K	1.85@800 K	51
WS_2	2H	BTE (BoltzTraP)	299.87		0.06		0.43@1000 K	43
WS_2	2H	Landauer		0.23	0.41			248
WS_2	2H	BTE		2.8728				253
WS_2	2H	Landauer	0.83 (conductance per width)	0.22	0.43	1.08@800 K	1.50@800 K	51
WS_2	2H	BTE (BoltzTraP2)	15.6		0.006		0.238@1200 K	281
WS_2 -Bulk	2H	Landauer		0.28	0.082			252
WS_2 -1L	2H	Landauer		1.52	0.7			252
WS_2 -2L	2H	Landauer		1.98	0.72			252
WS_2 -3L	2H	Landauer		2.03	0.76			252
WS_2 -4L	2H	Landauer		1.85	0.76			252
WS_2	2H	BTE (BoltzTraP)	33.8 (x)		0.16 (x)			172
	(orthorhombic)		9.2 (y)		0.47 (y)			172
WSe_2	2H	BTE (BoltzTraP)	120.86		0.05		0.37@1000 K	43
WSe_2	2H	Landauer		0.38	0.35			248
WSe_2	2H	BTE		2.9191				253
WSe_2	2H	BTE (BoltzTraP)		0.13	0.075	0.8@1200 K	0.66@1200 K	18
WSe_2	2H	Landauer	0.66 (conductance per width)	0.33	0.34	2.18@800 K	1.21@800 K	51
WSe_2 -1L	2H	Landauer		1.88	0.62			252
WSe_2 -2L	2H	Landauer		1.92	0.62			252
WSe_2 -2L	2H	Landauer				2.1@500 K		249
WSe_2 -3L	2H	Landauer		1.44	0.62			252
WSe_2 -4L	2H	Landauer		1.13	0.62			252
WSe_2 -Bulk	2H	Landauer		0.26	0.12			252
WTe_2	2H	Landauer	0.50 (conductance per width)	0.36	0.42	1.57@800 K	1.49@800 K	51

TABLE IV. Cont. Lattice thermal conductivity (conductance) and ZT values of CrX_2 , MoX_2 , and W_2 ($X=\text{S,Se,Te}$) at room temperature.

Material	Phase (1T/2H)	Theoretical Method (Tool)	κ_L ($\text{Wm}^{-1}\text{K}^{-1}$)	ZT		ZT_{max}		Refs.
				n -type	p -type	n -type	p -type	
SeMoS	Janus	BTE (BoltzTraP)		~ 1.0	~ 1.0	1.04@1200 K	1.0@1200 K	279
TeMoS	Janus	BTE (BoltzTraP)				0.84@1200 K	0.86@1200 K	279
WSSe	Janus	BTE (BoltzTraP2)	11		0.013		0.355@1200 K	281
WSSe	Janus	BTE (BoltzTraP)	25.37			0.72@1500 K	0.73@1500 K	282
WSTe	Janus	BTE (BoltzTraP2)	0.075		0.74		2.56@1200 K	281
graphene/MoSSe	C/SMoSe stacked NR	Landauer	0.067 (nW K^{-1})		1.16			285
graphene/MoSSe	C/SeMoS stacked NR	Landauer	0.045 (nW K^{-1})	2.01				285
MoSSe	symmetric aNR	Landauer	0.077 (nW K^{-1})		1.64			285
MoSSe	asymmetric aNR	Landauer	0.11 (nW K^{-1})	1.25				285
MoSSe	bilayer NR	Landauer	0.012 (nW K^{-1})	1.28				285
MoS ₂ /MoSe ₂	2H-Hetero	BTE		0.084	0.648	0.115@800 K	1.289@800 K	288
MoS ₂ /WS ₂	2H-Hetero	BTE		0.093	0.407	0.125@800 K	0.871@800 K	288
MoSe ₂ /MoS ₂	2H-Hetero	BTE		0.165	0.56	0.223@500 K	0.934@800 K	288
MoSe ₂ /WSe ₂	2H-Hetero	BTE		0.173	0.714	0.227@500 K	1.045@800 K	288
WS ₂ /MoS ₂	2H-Hetero	BTE		0.598	0.274	1.641@800 K	0.486@800 K	288
WS ₂ /WSe ₂	2H-Hetero	BTE		0.997	0.37	1.806@800 K	0.736@800 K	288
WSe ₂ /MoSe ₂	2H-Hetero	BTE		0.485	0.015	0.875@800 K	0.017@500 K	288
WSe ₂ /WS ₂	2H-Hetero	BTE		0.488	0.011	0.879@800 K	0.013@800 K	288
WS ₂ /WSe ₂	2H-Lateral	BTE (BoltzTraP)	16.9 (x)		0.28 (x)			172
	Superlattice		4.5 (y)		0.68 (y)			172
WS ₂ -WSe ₂	2H-Superlattice (SL1)	BTE (BoltzTraP)	69.95 (x)				0.95 (x)@1000 K	43
			75.06 (y)				0.67 (y)@1000 K	43
WS ₂ -WSe ₂	2H-Superlattice (SL2)	BTE (BoltzTraP)	46 (x)				0.62 (x)@1000 K	43
			53.52 (y)				0.66 (y)@1000 K	43

first-principles calculations within the ballistic transport approach to obtain TE properties of 2D PtX_2 ($X=\text{O, S, Se, Te}$) monolayers. They investigated the ZT values using NEGF formalism. Among these PtX_2 ($X=\text{O, S, Se, Te}$) monolayers, PtTe_2 exhibits the lowest κ_L with a value of $0.207 \text{ W m}^{-1} \text{ K}^{-1}$. κ_L values from lowest to highest are reported as follows 0.297 (PtSe_2), 0.376 (PtS_2) and 0.643 (PtO_2) $\text{Wm}^{-1} \text{ K}^{-1}$. At $T=300 \text{ K}$, p -type charge carrier concentrations of PtTe_2 , PtO_2 , PtSe_2 have ZT values of 1.65, 0.94 and 0.84, respectively. For PtS_2 , n -type charge carrier concentration has prominent ZT value compared to p -type carrier concentration and its ZT value has been reported as 1.42. Under the influence of tensile strain, ZT values of PtTe_2 and PtS_2 monolayers have been decreased to 1.29. Furthermore, San-Dong Guo³¹⁴ explored the bi-axial strain effect on TE properties of PtSe_2 monolayer by performing first principles calculations and semi-classical Boltzmann transport theory as implemented in BoltzTraP³¹⁴. The lattice TC for 4.02% biaxial tensile strain rate is obtained at τ with decreasing τ at 600 K, and 0.80 (for 2.68% compressive strain rate), 0.45 (for 4.02% compressive strain rate) and 0.1 (for 4.02% compressive strain rate) at 900 K³¹⁴. In addition to this study, biaxial strain effect on TE properties of PtTe_2 was studied by Guo *et al.*³¹⁵ using DFT, BoltzTraP code and solving linearized phonon BTE as implemented in Phono3py code. The lattice TC value of PtTe_2 monolayer reported as $7.89 \text{ W m}^{-1} \text{ K}^{-1}$ and $6.37 \text{ W m}^{-1} \text{ K}^{-1}$ with strain rates of 0% and 4%, respectively, at $T = 300 \text{ K}$. For PtTe_2 , it

was concluded that the TC value decreased at a rate of 19% when 4% biaxial strain was applied³¹⁵.

Tao *et al.*³¹⁶ explored the TE properties of pentagonal PtX_2 ($X = \text{S, Se, Te}$) monolayers by carrying out first-principles based BoltzTraP calculations within the RTA. Using ShengBTE code, lattice TC of pentagonal PtTe_2 at 300 K was obtained as 1.77 and $5.17 \text{ W m}^{-1} \text{ K}^{-1}$ along x and y directions, respectively. Along the $x(y)$ direction, κ_L value of PtS_2 and PtSe_2 is larger than PtTe_2 with a value of 4.27 (8.86) and 3.12 ($7.05 \text{ W m}^{-1} \text{ K}^{-1}$), respectively. Compared to hexagonal PtS_2 ($\kappa_L = 54.25 \text{ W m}^{-1} \text{ K}^{-1}$) and PtSe_2 ($\kappa_L = 18.06 \text{ W m}^{-1} \text{ K}^{-1}$) monolayers³¹⁷, pentagonal structures possess lower κ_L values. Since lattice TC is inversely proportional to temperature, at $T = 600 \text{ K}$, κ_L value of the pentagonal PtTe_2 along $x(y)$ direction decreased by 49.7% (50.2%) and its value was reported as 0.89 (2.57) $\text{W m}^{-1} \text{ K}^{-1}$. For p -type charge carrier concentration, the anisotropy in ZT values of the pentagonal PtTe_2 , PtSe_2 , PtS_2 has found to be $ZT_x/ZT_y=2.60/1.14$, $1.75/0.82$ and $0.58/0.16$ at $T = 300 \text{ K}$. For higher temperature values ($T = 600 \text{ K}$), p -type and n -type PtTe_2 exhibits significant ZT along x -direction and it was reported as 5.03 and 4.85, respectively³¹⁶. In addition, they calculated the ZT values of p -type pentagonal PtS_2 and PtSe_2 as 1.46 and 3.42 along the x -direction at $T= 600 \text{ K}$. The reported values point out the efficiency resulting in TE power generation and cooling incompatible with mechanical devices and therefore, indicate the tremendous potential of these materials.

In recent years, Janus structures have received considerable attention in terms of TE research. 1T PdS₂, PdSe₂ pristine monolayers and 1T PdSSe, PdSTe and PdSeTe Janus monolayers investigated by Moujaes and Diery¹⁵³ using first principles based BTE calculations. The lattice TC of PdSe₂ has notably high anisotropy, and the ratio is obtained as $\kappa_L^{yy}/\kappa_L^{xx}=0.67$ at T=300 K. Since the lattice TC of PdS₂, PdSSe, PdSTe and PdSeTe is slightly anisotropic, the lattice TC reported as an average value ($\kappa_L^{av} = (\kappa_L^{xx} + \kappa_L^{yy})/2$). Among considered materials, PdSeTe and PdSTe exhibit lower lattice TCs with a value of $\kappa_L^{av}=1.21$ and $1.09 \text{ W m}^{-1} \text{ K}^{-1}$. These materials are followed by PdSe₂ ($1.51 \text{ W m}^{-1} \text{ K}^{-1}$), PdSSe ($2.85 \text{ W m}^{-1} \text{ K}^{-1}$), and PdS₂ ($7.10 \text{ W m}^{-1} \text{ K}^{-1}$). ZT_{max} of both *p*-type and *n*-type charge carriers of PdS₂, PdSSe, PdSTe, and PdSeTe is slightly anisotropic. *p*-type PdSe₂ exhibits remarkable anisotropy in ZT_{max} . At $T = 300 \text{ K}$, the highest ZT_{max} value along the *x*-direction (*y*-direction) reported as 0.40 (0.42) for *p*-type PdSeTe. At higher temperature values (T=900 K), *p*-type PdSe₂ wins over, and the reported ZT_{max} value is 0.73 (0.77) along the *x*-direction (*y*-direction). In another study, phonon transport properties of PtSse Janus monolayer were explored by performing first-principles calculations and iterative solution of BTE within ShengBTE code³¹⁷. At room temperature, PtSse monolayer exhibits, $36.19 \text{ W m}^{-1} \text{ K}^{-1}$ lattice TC whereas PtS₂ and PtSe₂ monolayer have 54.25 and $18.06 \text{ W m}^{-1} \text{ K}^{-1}$, respectively. The κ_L value of PtSe₂ is lower than that of monolayer MoS₂ ($33.6 \text{ W m}^{-1} \text{ K}^{-1}$ ²⁴⁷) and WS₂ ($31.8 \text{ W m}^{-1} \text{ K}^{-1}$ ²⁴⁷). TE properties of Janus MXY (M= Pd, Pt; X, Y= S, Se, Te) monolayers were comprehensively explored by Tao *et al.*³¹⁸ using first principles calculations within BTE implemented in ShengBTE and BoltzTraP codes. The value of lattice TC from highest to lowest was reported as PtSse > PtSTe > PtSeTe > PdSSe > PdSTe > PdSeTe. The lowest TC values at T=300 K were calculated as 4.02 and 5.45 $\text{W m}^{-1} \text{ K}^{-1}$ for PdSeTe and PdSTe Janus monolayers. For the remaining materials, Tao *et al.*³¹⁸ obtained the TC values as 36.19 (PtSse), 20.56 (PtSTe), 14.47 (PtSeTe), 10.65 (PdSSe) $\text{W m}^{-1} \text{ K}^{-1}$. At 300 K, *p*-type charge carriers of PdSeTe and PtSeTe monolayers have the highest TE performance ($ZT = 0.98$ and $ZT = 0.91$, respectively) among these Janus monolayers. For 600 K, the ZT values of *p*-type PdSeTe and *p*-type PtSeTe have been reported as 1.86 and 1.97, respectively. When the temperature reaches 900K, *p*-type PtSeTe has maximum ZT with a value of 2.54. At $T = 900 \text{ K}$, the other best performers are *p*-type PtSse and *p*-type PtSTe, and the ZT values of these materials were reported as 1.23 and 1.07, respectively. Hence, PtXY Janus monolayers can be considered as best candidates as TE material at high temperatures.

The above-mentioned literature results regarding the ZT values of PdX₂, PtX₂ (X=S, Se, Te) layers are summarized in Table V. In addition to these studies, strain engineering was also adopted for these materials. Phonon transport properties of Janus PtSTe monolayer under the effect of biaxial tensile strain were investigated by Pan *et al.*¹⁹⁰ using first-principles calculations with Boltzmann transport theory. At T=300 K, Janus PtSTe has low TC with a value of 25.71 W

$\text{m}^{-1} \text{ K}^{-1}$, and for the applied strain rate 4%, Janus PtSTe exhibits a lower κ_L value ($13.86 \text{ W m}^{-1} \text{ K}^{-1}$). When the strain rate increased to 8%, the κ_L value was reported as $3.21 \text{ W m}^{-1} \text{ K}^{-1}$.

VII. CONCLUSION AND FUTURE PERSPECTIVE

It is essential to enhance investing and using renewable, fossil fuel-free energy sources to solve the environmental problems we face due to the carbon emission – of course, the political problems that are devastating the World. TE energy conversion has been studied as an alternative in that sense for many years, but the stage reached today is far from meeting this target. Because materials with desired application criteria such as high PF and conversion performance (which is around $ZT > 4$) at a wide temperature range have not been realized yet. Considering the tremendous past effort in the realization of such material, whether the future research plans are unwarranted is another issue. However, the general interpretation we have obtained as a result of the extensive TMD material analysis conducted within the framework of this study is that future TE researches target low-energy critical technology applications (e. g., waste heat recycling) or wearable electronics (e. g. passive sensors)³¹⁹. In this context, if we revise the potential of TMDs for TE applications, the prominent materials would be concluded as follows (Please see Table I-V for further details).

Within the Ti, Zr, and Hf-based TMD materials, experimentally realized 1T-HfSe₂ is highly promising due to the obtained *n*-type ZT values around 2 at high temperature and 1 at moderate temperature values. Also, 1T-TiS₂ is another promising TMD for future investigations in particular due to its ZT value around 1 for a wide range of temperature values. Besides the already synthesized structures, 1H-TiSe₂, 1H-HfSe₂, and 1H-HfS₂ are other potential candidates for future TE research due to their computed *n*- and *p*-type ZT values greater than 2 at higher temperature range. Similar values have also been reported for Cr, Mo, and W-based materials, as well. The calculated ZT values > 2 at both low and high-temperature regimes for 2H structures are pretty promising, however, there is no experimental proof yet. In fact, Pd-, and Pt-based TMDs are the most promising candidates according to computational analyses. In particular, the pentagonal structures PtTe₂, PdTe₂ and PtSe₂ possess ZT values greater than 3 at moderate temperature values. These results are quite a good motivation to search for new routes for synthesizing these materials.

Moreover, quite promising results frankly depict that nanostructuring and layer engineering pave the way for a clear path to engineering the TE potential of TMD materials. For instance, *n*-type ZT values > 1.0 for 1T-ZrSe₂-HfSe₂, ZrSe₂-TiSe₂, graphene/MoSSe, MoS₂/MoSe₂, WS₂/MoS₂, and WS₂/WSe₂ heterostructures, and the predicted stacking-dependent ZT values between 3 and 5 for both monolayer and bilayer Janus TMD structures are conspicuous demonstrations in that sense.

On the other hand, the large area and defect-free synthe-

TABLE V. Lattice thermal conductivity (conductance) and ZT values of Pd and Pt dichalcogenides at room temperature. (*: $\kappa_L^{av} = (\kappa_L^{xx} + \kappa_L^{yy}/2)$)

Material	Phase (1T/2H)	Theoretical Method (Tool)	κ_L ($\text{Wm}^{-1}\text{K}^{-1}$)	ZT		ZT_{max}		Refs.
				n -type	p -type	n -type	p -type	
PdS ₂	pentagonal 1T	BTE (BoltzTraP)	4.34 (x) 12.48 (y)		0.85 (x)			309
		BTE (BoltzWann)	7.10*	0.04(x)	0.09(x)	0.36(x)@900 K	0.41(x)@900 K	153
				0.04 (y)	0.08 (y)	0.37 (y)@900 K	0.42 (y)@900 K	153
PdSe ₂	pentagonal 1T	BTE (BoltzTraP)	2.91(x) 6.62 (y)		1.18(x)			309
		BTE (BoltzTraP)	3.7(x) 7.2(y)		1.1(x) 0.5(y)			44
		BTE (BoltzWann)	1.51*	0.14(x)	0.34(x)	0.49(x)@900 K	0.73(x)@900K	153
PdTe ₂	pentagonal 1T	BTE (BoltzTraP)	1.42(x) 5.90(y)		2.42(x)			309
		BTE (BoltzTraP)	3.20(ZZ) 3.23(AC)	0.8(ZZ) 0.59(AC)				41
	1T	Wiedemann–Franz		3.4(ZZ)	0.09 (ZZ)			41
	pentagonal	BTE (BoltzTraP)	0.53(x) 1.21(y)	0.7(x)	0.8(x)	0.85(x)@700 K	0.91(x)@700 K	41
	pentagonal	Wiedemann–Franz		1.9(y)	3.75(x)			41
	1T	BTE (BoltzTraP)	1.3	0.24 ($\tau = 5$ fs)		1.08@700 K $\tau = 5$ fs		311
PtS ₂	1T	NEGF (NanoDCAL)	0.376	1.42				313
PtSe ₂	pentagonal 1T	BTE (BoltzTraP)	4.27(x) 8.86(y)		0.58(x) 0.16(y)		1.46(x)@600 K	316
		NEGF (NanoDCAL)	0.297		0.84			313
PtTe ₂	pentagonal 1T	BTE (BoltzTraP)	3.12(x) 7.05(y)		1.75(x) 0.82(y)		3.42(x)@600 K	316
		NEGF (NanoDCAL)	0.207		1.65			313
PdSeTe	1T	BTE (BoltzTraP)	1.77 (x)		2.60(x)	4.85(x)@600K	5.03(x)@600 K	316
			5.17 (y)		1.14 (y)		2.68(y)@600 K	316
			1.21*	0.22(x)	0.40(x)	0.52(x)@600 K	0.65(x)@900 K	153
PdSSe	1T	BTE (BoltzTraP)	4.02	0.23 (y)	0.42 (y)	0.51 (y) @600 K	0.65(y)@900 K	153
			2.85*	0.13	0.98	0.34@600 K	1.86@600 K	318
				0.11(x)	0.2 (x)	0.42 (x)@900 K	0.66(x)@900 K	153
PdSTe	1T	BTE (BoltzTraP)	10.65	0.09(y)	0.27(y)	0.42(y)@900 K	0.65(y)@600K	153
			1.09*	0.07	0.09	0.49@900 K	0.58@900 K	318
				0.16(x)	0.25(x)	0.52(x)@900 K	0.57 (x)@ 900 K	153
PtSeTe	1T	BTE (BoltzTraP)		0.17(y)	0.26(y)	0.51(y)@900 K	0.58(y)@900 K	153
			5.45	0.09	0.26	0.31@600 K	0.59@600 K	318
			14.47	0.07	0.91	0.52@900 K	2.54@900 K	318
PtSSe	1T	BTE (BoltzTraP)	36.19	0.03	0.37	0.28@900 K	1.23@900 K	318
PtSTe	1T	BTE (BoltzTraP)	20.56	0.12	0.26	0.34@900 K	1.07@900 K	318

sis of these materials are still challenging. Therefore, considering the TMDs in inorganic-organic hybrid TE materials research is another possible direction^{320–322}. In fact, promising results regarding TE performance have already been reported for conducting polymer/inorganic-semiconductor and /CNT/graphene-based binary TE materials and also ternary hybrid nanocomposite-based TE materials³²³. Moreover, binary and ternary nanostructured TMD-based materials may have the potential to be adopted in printed electronic circuits and device applications which is another flourishing research area of micro and nanoelectronics³²⁴. Since the future target of using TE power supply in IoT technologies is on the agenda, it is important to proceed in this direction in terms of the bonding research with technology. Of course, fabrication and device implementation difficulties are not the scope of this analysis.

In the main part of the article, we present a broad summary of the theoretical approaches developed within the framework of TE research. These methods and approaches are accu-

rate enough to characterize computationally special cases, but there is still plenty of room for improvement to apply these approaches for more realistic, in particular hybrid TE materials. One may argue that computational studies in the ballistic region are quite sufficient to obtain consistent results – for both electronic and thermal transport. And these approaches are very useful for nano-size TE applications. However, the methods that can be adopted for the theoretical characterization of TE materials that can be used in applications such as wearable electronics and sensors are only at the level of producing a physical insight into the TE potential of structures.

In terms of electronic transport calculations, the recently developed carrier relaxation time calculations (mostly electron-phonon coupling-based scattering) have made a significant contribution to the field and provided a remarkable advantage for TE materials search and selection studies. However, due to computational limitations, applying these approaches to large-scale crystal systems or hybrid TE materials is still challenging. Therefore, technical advancements or

multi-scale approach development in that sense is highly critical. On the other hand, scattering mechanisms, in addition to the electron-phonon scattering-based one, such as carrier scattering due to the defects and dislocations, are highly effective in fully understanding the electron transport phenomenon in functional TE materials. Thus, developing novel approaches considering multiple scattering mechanisms and centers might be another future goal. Here, we should once more note the Multi-Scale modeling due to its potential for the adoption of these desired improvements in TE materials simulations.

On the other hand, the Phonon Boltzmann Transport-based first-principles approaches are very powerful for accurately characterizing the lattice thermal transport properties of nanostructure and bulk TE materials. Using these approaches, the inclusion of some additional scattering mechanisms such as alloying, isotope disorder, and defects are also possible for specific cases. Moreover, machine learning-based methods such as HIPHIVE¹⁸⁷ notably reduce the required computational cost for these simulations and makes them possible to apply to large-scale periodic structures. Thus, these BTE-based approaches are powerful tools to be used in multi-scale modeling approaches. However, the direct implementation of these methods for mentioned hybrid TE materials is highly complicated. This challenge can be overcome with MD simulations, but here too, future improvements are required. The accuracy of the traditional force fields is limited. The machine learning potentials are more accurate and can be used to determine lattice thermal transport properties of large-scale and hybrid structures. However, two important drawbacks must be addressed in the near future in that sense: The maximum number of elements to be used in machine learning potential fittings and reaching MD simulation speed limits with machine learning potentials.

In summary, the current literature points out that the experimental studies evolve toward synthesis of hybrid TE materials such as organic-inorganic, nanoparticle matrices, and multi-layer thin film structures. Moreover, the improvement of already characterized TE materials for smart devices, in particular wearable, applications is one of the main scopes now. We should expect to see TE components to take part in technological products much more frequently in the near future.

On the other hand, the following computational research efforts will be highly beneficial for materials optimization and novel materials search studies; (i) improvement and application of the computational tools to characterize electronic transport properties more accurately, including electron relaxation times, (ii) development of multi-scale materials simulation approaches and tools for accurate electronic and thermal transport for ordered and disordered systems, and (iii) development of accurate and computationally fast machine learning potentials for complex materials including multi-element structures.

ACKNOWLEDGMENTS

H.S. acknowledges the support from the TUBITAK projects, 117F480 and 119F353. C. S. acknowledges the sup-

port from the Eskisehir Technical University (22ADP150).

- ¹C. Wood, "Materials for thermoelectric energy conversion," Reports on progress in physics **51**, 459 (1988).
- ²G. J. Snyder et al., "Thermoelectric power generation: Efficiency and compatibility," Thermoelectrics handbook: macro to nano (2006).
- ³D. Champier, "Thermoelectric generators: A review of applications," Energy Conversion and Management **140**, 167–181 (2017).
- ⁴R. Landauer, "Spatial variation of currents and fields due to localized scatterers in metallic conduction," IBM Journal of research and development **1**, 223–231 (1957).
- ⁵C. Jeong, R. Kim, M. Luisier, S. Datta, and M. Lundstrom, "On Landauer versus Boltzmann and full band versus effective mass evaluation of thermoelectric transport coefficients," Journal of Applied Physics **107**, 023707 (2010).
- ⁶M. Cutler and N. F. Mott, "Observation of Anderson localization in an electron gas," Physical Review **181**, 1336 (1969).
- ⁷J. P. Heremans, V. Jovovic, E. S. Toberer, A. Saramat, K. Kurosaki, A. Charoenphakdee, S. Yamanaka, and G. J. Snyder, "Enhancement of thermoelectric efficiency in pbte by distortion of the electronic density of states," Science **321**, 554–557 (2008).
- ⁸J. Mao, Z. Liu, and Z. Ren, "Size effect in thermoelectric materials," npj Quantum Materials **1**, 1–9 (2016).
- ⁹Y. Zhou and L.-D. Zhao, "Promising thermoelectric bulk materials with 2D structures," Advanced Materials **29**, 1702676 (2017).
- ¹⁰M. Samanta, T. Ghosh, S. Chandra, and K. Biswas, "Layered materials with 2D connectivity for thermoelectric energy conversion," Journal of Materials Chemistry A **8**, 12226–12261 (2020).
- ¹¹J. Peltier, "New experiments on the heat effects of electric currents," Ann. Chim. Phys **56**, 371–386 (1834).
- ¹²C. Kittel, *Introduction to solid state physics*, Vol. 8 (John Wiley & Sons, Inc, 2005) pp. 121–122.
- ¹³L. D. Hicks and M. S. Dresselhaus, "Thermoelectric figure of merit of a one-dimensional conductor," Physical review B **47**, 16631 (1993).
- ¹⁴L. D. Hicks and M. S. Dresselhaus, "Effect of quantum-well structures on the thermoelectric figure of merit," Physical Review B **47**, 12727 (1993).
- ¹⁵M. Dresselhaus, X. Sun, S. Cronin, T. Koga, G. Dresselhaus, and K. Wang, "Prospects for high thermoelectric figures of merit in 2d systems," MRS Online Proceedings Library (OPL) **478**, 55 (1997).
- ¹⁶A. Balandin and K. L. Wang, "Significant decrease of the lattice thermal conductivity due to phonon confinement in a free-standing semiconductor quantum well," Physical Review B **58**, 1544 (1998).
- ¹⁷A. Nissimagoudar and N. Sankeshwar, "Significant reduction of lattice thermal conductivity due to phonon confinement in graphene nanoribbons," Physical Review B **89**, 235422 (2014).
- ¹⁸S. Kumar and U. Schwingenschlögl, "Thermoelectric response of bulk and monolayer MoSe₂ and WSe₂," Chemistry of Materials **27**, 1278–1284 (2015).
- ¹⁹D. Saleta Reig, S. Varghese, R. Farris, A. Block, J. D. Mehew, O. Hellman, P. Woźniak, M. Sledzinska, A. El Sachat, E. Chávez-Ángel, et al., "Unraveling heat transport and dissipation in suspended mose2 from bulk to monolayer," Advanced Materials **34**, 2108352 (2022).
- ²⁰E. Unsal, R. Senger, and H. Sevinçli, "Enhancement of thermoelectric efficiency of T-HfSe₂ via nanostructuring," Physical Review B **103**, 014104 (2021).
- ²¹Z. Zhang, Y. Ouyang, Y. Cheng, J. Chen, N. Li, and G. Zhang, "Size-dependent phononic thermal transport in low-dimensional nanomaterials," Physics Reports **860**, 1–26 (2020).
- ²²R. Chen, J. Lee, W. Lee, and D. Li, "Thermoelectrics of nanowires," Chemical reviews **119**, 9260–9302 (2019).
- ²³D. Singh and R. Ahuja, "Dimensionality effects in high-performance thermoelectric materials: Computational and experimental progress in energy harvesting applications," Wiley Interdisciplinary Reviews: Computational Molecular Science **12**, e1547 (2022).
- ²⁴H. Alam and S. Ramakrishna, "A review on the enhancement of figure of merit from bulk to nano-thermoelectric materials," Nano energy **2**, 190–212 (2013).
- ²⁵R. Takahashi and S. Murakami, "Thermoelectric transport in perfectly conducting channels in quantum spin hall systems," Physical Review B **81**, 161302 (2010).

- ²⁶S. Murakami, R. Takahashi, O. Tretiakov, A. Abanov, and J. Sinova, "Thermoelectric transport of perfectly conducting channels in two- and three-dimensional topological insulators," in *Journal of Physics: Conference Series*, Vol. 334 (IOP Publishing, 2011) p. 012013.
- ²⁷Y. Xu, Z. Gan, and S.-C. Zhang, "Enhanced thermoelectric performance and anomalous seebeck effects in topological insulators," *Physical review letters* **112**, 226801 (2014).
- ²⁸D. A. Bandurin, A. V. Tyurnina, G. L. Yu, A. Mishchenko, V. Zolyomi, S. V. Morozov, R. K. Kumar, R. V. Gorbachev, Z. R. Kudrynskiy, S. Pezzini, et al., "High electron mobility, quantum hall effect and anomalous optical response in atomically thin inSe," *Nature nanotechnology* **12**, 223–227 (2017).
- ²⁹J. Ou and Q. Zhang, "Enhanced spin thermopower in phosphorene nanoribbons via edge-state modifications," *Nanomaterials* **12**, 2350 (2022).
- ³⁰O. Ávalos-Ovando, D. Mastrogiuseppe, and S. E. Ulloa, "Lateral heterostructures and one-dimensional interfaces in 2d transition metal dichalcogenides," *Journal of Physics: Condensed Matter* **31**, 213001 (2019).
- ³¹R. Ma, H. Geng, W. Deng, M. Chen, L. Sheng, and D. Xing, "Effect of the edge states on the conductance and thermopower in zigzag phosphorene nanoribbons," *Physical Review B* **94**, 125410 (2016).
- ³²N. Xu, Y. Xu, and J. Zhu, "Topological insulators for thermoelectrics," *npj Quantum Materials* **2**, 51 (2017).
- ³³Y. Zhou, K. Luo, X. Zha, Z. Liu, X. Bai, Q. Huang, Z. Guo, C.-T. Lin, and S. Du, "Electronic and transport properties of Ti₂CO₂ mxene nanoribbons," *The Journal of Physical Chemistry C* **120**, 17143–17152 (2016).
- ³⁴D. Tang, M. Dan, and Y. Zhang, "High performance piezotronic thermoelectric devices based on zigzag MoS₂ nanoribbon," *Nano Energy* **104**, 107888 (2022).
- ³⁵X. Wang, V. Askarpour, J. Maassen, and M. Lundstrom, "On the calculation of Lorenz numbers for complex thermoelectric materials," *Journal of Applied Physics* **123**, 055104 (2018).
- ³⁶H.-S. Kim, Z. M. Gibbs, Y. Tang, H. Wang, and G. J. Snyder, "Characterization of Lorenz number with Seebeck coefficient measurement," *APL materials* **3**, 041506 (2015).
- ³⁷E. Witkoske, X. Wang, J. Maassen, and M. Lundstrom, "Universal behavior of the thermoelectric figure of merit, zT, vs. quality factor," *Materials Today Physics* **8**, 43–48 (2019).
- ³⁸H. Lv, W. Lu, D. Shao, H. Lu, and Y. Sun, "Strain-induced enhancement in the thermoelectric performance of a ZrS₂ monolayer," *Journal of Materials Chemistry C* **4**, 4538–4545 (2016).
- ³⁹D. Qin, X.-J. Ge, G.-q. Ding, G.-y. Gao, and J.-T. Lü, "Strain-induced thermoelectric performance enhancement of monolayer ZrSe₂," *RSC advances* **7**, 47243–47250 (2017).
- ⁴⁰P. Sengupta, Y. Tan, G. Klimeck, and J. Shi, "Low-temperature thermal transport and thermopower of monolayer transition metal dichalcogenide semiconductors," *Journal of Physics: Condensed Matter* **29**, 405701 (2017).
- ⁴¹B. Marfoua and J. Hong, "High thermoelectric performance in hexagonal 2D PdTe₂ monolayer at room temperature," *ACS applied materials & interfaces* **11**, 38819–38827 (2019).
- ⁴²H. Wang, Y.-S. Lan, B. Dai, X.-W. Zhang, Z.-G. Wang, and N.-N. Ge, "Improved Thermoelectric Performance of Monolayer HfS₂ by Strain Engineering," *ACS omega* **6**, 29820–29829 (2021).
- ⁴³D. Han, X. Yang, M. Du, G. Xin, J. Zhang, X. Wang, and L. Cheng, "Improved thermoelectric properties of WS₂-WSe₂ phononic crystals: insights from first-principles calculations," *Nanoscale* **13**, 7176–7192 (2021).
- ⁴⁴D. Qin, P. Yan, G. Ding, X. Ge, H. Song, and G. Gao, "Monolayer PdSe₂: A promising two-dimensional thermoelectric material," *Scientific reports* **8**, 1–8 (2018).
- ⁴⁵Z. M. Gibbs, F. Ricci, G. Li, H. Zhu, K. Persson, G. Ceder, G. Hautier, A. Jain, and G. J. Snyder, "Effective mass and fermi surface complexity factor from ab initio band structure calculations," *npj Computational Materials* **3**, 8 (2017).
- ⁴⁶M. Dutta, T. Ghosh, and K. Biswas, "Electronic structure modulation strategies in high-performance thermoelectrics," *Apl Materials* **8**, 040910 (2020).
- ⁴⁷D. I. Bilc, D. Bena, V. Pop, P. Ghosez, and M. J. Verstraete, "Electronic and Thermoelectric Properties of Transition-Metal Dichalcogenides," *The Journal of Physical Chemistry C* (2021).
- ⁴⁸H. Wang, Y. Pei, A. D. LaLonde, and G. J. Snyder, "Material design considerations based on thermoelectric quality factor," in *Thermoelectric Nanomaterials* (Springer, 2013) pp. 3–32.
- ⁴⁹O. Cherniushok, T. Parashchuk, J. Tobola, S. D. Luu, A. Pogodin, O. Kokhan, I. Studenyak, I. Barchiy, M. Piasecki, and K. T. Wojciechowski, "Entropy-induced multivalley band structures improve thermoelectric performance in p-Cu₇P (S_xSe_{1-x})₆ argyrodites," *ACS Applied Materials & Interfaces* **13**, 39606–39620 (2021).
- ⁵⁰P. Yan, G.-y. Gao, G.-q. Ding, and D. Qin, "Bilayer MSe₂ (M= Zr, Hf) as promising two-dimensional thermoelectric materials: a first-principles study," *RSC advances* **9**, 12394–12403 (2019).
- ⁵¹G. Özal, R. T. Senger, C. Sevik, and H. Sevinçli, "Ballistic thermoelectric properties of monolayer semiconducting transition metal dichalcogenides and oxides," *Physical Review B* **100**, 085415 (2019).
- ⁵²B. Kozinsky and D. J. Singh, "Thermoelectrics by Computational Design: Progress and Opportunities," *Annual Review of Materials Research* **51** (2021).
- ⁵³P. Graziosi, C. Kumarasinghe, and N. Neophytou, "Material descriptors for the discovery of efficient thermoelectrics," *ACS Applied Energy Materials* **3**, 5913–5926 (2020).
- ⁵⁴P. Gorai, V. Stevanović, and E. S. Toberer, "Computationally guided discovery of thermoelectric materials," *Nature Reviews Materials* **2**, 1–16 (2017).
- ⁵⁵G. Xing, J. Sun, Y. Li, X. Fan, W. Zheng, and D. J. Singh, "Electronic fitness function for screening semiconductors as thermoelectric materials," *Physical Review Materials* **1**, 065405 (2017).
- ⁵⁶G. Xing, J. Sun, Y. Li, X. Fan, W. Zheng, and D. J. Singh, "Erratum: Electronic fitness function for screening semiconductors as thermoelectric materials [Phys. Rev. Materials 1, 065405 (2017)]," *Physical Review Materials* **1**, 079901 (2017).
- ⁵⁷Y. Ota, H. Namiki, H. Yamazaki, R. Konagaya, S. Yonezawa, T. Komori, and M. Takashiri, "Effect of Se incorporation on thermoelectric properties of Bi₂ (Se_xTe_{1-x})₃ alloys," *Japanese Journal of Applied Physics* **60**, 070910 (2021).
- ⁵⁸P. Bulut, B. Beceren, S. Yıldırım, C. Sevik, and T. Gürel, "Promising room temperature thermoelectric conversion efficiency of zinc-blende AgI from first principles," *Journal of Physics: Condensed Matter* **33**, 015501 (2020).
- ⁵⁹P. Adebambo, O. Osafire, J. Laoye, M. Idowu, and G. Adebayo, "Electronic fitness function, effective mass and thermoelectric properties of Rh-based (-ScTe₂-TiSb)-VSn alloys for thermoelectric generator applications," *Computational Condensed Matter* **26**, e00523 (2021).
- ⁶⁰S. Sarikurt, T. Kocabaş, and C. Sevik, "High-throughput computational screening of 2D materials for thermoelectrics," *Journal of Materials Chemistry A* **8**, 19674–19683 (2020).
- ⁶¹Z. Feng, Y. Fu, A. Putatunda, Y. Zhang, and D. J. Singh, "Electronic structure as a guide in screening for potential thermoelectrics: Demonstration for half-Heusler compounds," *Physical Review B* **100**, 085202 (2019).
- ⁶²G. Ding, G. Gao, Z. Huang, W. Zhang, and K. Yao, "Thermoelectric properties of monolayer MSe₂ (M= Zr, Hf): low lattice thermal conductivity and a promising figure of merit," *Nanotechnology* **27**, 375703 (2016).
- ⁶³H. J. Goldsmid et al., *Introduction to thermoelectricity*, Vol. 121 (Springer, 2010).
- ⁶⁴G. J. Snyder and A. H. Snyder, "Figure of merit ZT of a thermoelectric device defined from materials properties," *Energy & Environmental Science* **10**, 2280–2283 (2017).
- ⁶⁵H. S. Kim, W. Liu, G. Chen, C.-W. Chu, and Z. Ren, "Relationship between thermoelectric figure of merit and energy conversion efficiency," *Proceedings of the National Academy of Sciences* **112**, 8205–8210 (2015).
- ⁶⁶Q. Yan and M. G. Kanatzidis, "High-performance thermoelectrics and challenges for practical devices," *Nature materials* **21**, 503–513 (2022).
- ⁶⁷K. Kanahashi, J. Pu, and T. Takenobu, "2d materials for large-area flexible thermoelectric devices," *Advanced Energy Materials* **10**, 1902842 (2020).
- ⁶⁸K. Nan, S. D. Kang, K. Li, K. J. Yu, F. Zhu, J. Wang, A. C. Dunn, C. Zhou, Z. Xie, M. T. Agne, et al., "Compliant and stretchable thermoelectric coils for energy harvesting in miniature flexible devices," *Science Advances* **4**, eaau5849 (2018).
- ⁶⁹K. Hippalgaonkar, Y. Wang, Y. Ye, D. Y. Qiu, H. Zhu, Y. Wang, J. Moore,

- S. G. Louie, and X. Zhang, "High thermoelectric power factor in two-dimensional crystals of MoS₂," *Physical Review B* **95**, 115407 (2017).
- ⁷⁰M. Yoshida, T. Iizuka, Y. Saito, M. Onga, R. Suzuki, Y. Zhang, Y. Iwasa, and S. Shimizu, "Gate-optimized thermoelectric power factor in ultrathin WSe₂ single crystals," *Nano letters* **16**, 2061–2065 (2016).
- ⁷¹S. Lv, Z. Qian, D. Hu, X. Li, and W. He, "A comprehensive review of strategies and approaches for enhancing the performance of thermoelectric module," *Energies* **13**, 3142 (2020).
- ⁷²T. Tritt and D. Rowe, "Thermoelectrics handbook: macro to nano," *Thermoelectrics Handbook: Macro to Nano* (2005).
- ⁷³W. He, J. Zhou, C. Chen, and J. Ji, "Experimental study and performance analysis of a thermoelectric cooling and heating system driven by a photovoltaic/thermal system in summer and winter operation modes," *Energy conversion and management* **84**, 41–49 (2014).
- ⁷⁴M. Siahmargoi, N. Rahbar, H. Kargarsharifabad, S. E. Sadati, and A. Asadi, "An experimental study on the performance evaluation and thermodynamic modeling of a thermoelectric cooler combined with two heatsinks," *Scientific reports* **9**, 1–11 (2019).
- ⁷⁵X. Wang, M. Zebarjadi, and K. Esfarjani, "High-performance solid-state thermionic energy conversion based on 2d van der waals heterostructures: A first-principles study," *Scientific reports* **8**, 1–9 (2018).
- ⁷⁶G. Mahan and J. Sofo, "The best thermoelectric," *Proceedings of the National Academy of Sciences* **93**, 7436–7439 (1996).
- ⁷⁷J. Zhou, R. Yang, G. Chen, and M. S. Dresselhaus, "Optimal bandwidth for high efficiency thermoelectrics," *Physical review letters* **107**, 226601 (2011).
- ⁷⁸C. Jeong, R. Kim, and M. S. Lundstrom, "On the best bandstructure for thermoelectric performance: A Landauer perspective," *Journal of Applied Physics* **111**, 113707 (2012).
- ⁷⁹C. Rudderham and J. Maassen, "Analysis of simple scattering models on the thermoelectric performance of analytical electron dispersions," *Journal of Applied Physics* **127**, 065105 (2020).
- ⁸⁰H. Sevinçli, "Quartic dispersion, strong singularity, magnetic instability, and unique thermoelectric properties in two-dimensional hexagonal lattices of group-VA elements," *Nano letters* **17**, 2589–2595 (2017).
- ⁸¹J. Maassen, "Limits of thermoelectric performance with a bounded transport distribution," *Physical Review B* **104**, 184301 (2021).
- ⁸²J. Bardeen and W. Shockley, "Deformation potentials and mobilities in non-polar crystals," *Physical review* **80**, 72 (1950).
- ⁸³H. Lang, S. Zhang, and Z. Liu, "Mobility anisotropy of two-dimensional semiconductors," *Physical Review B* **94**, 235306 (2016).
- ⁸⁴Y. Wu, B. Hou, C. Ma, J. Cao, Y. Chen, Z. Lu, H. Mei, H. Shao, Y. Xu, H. Zhu, et al., "Thermoelectric performance of 2D materials: the band-convergence strategy and strong intervalley scatterings," *Materials Horizons* **8**, 1253–1263 (2021).
- ⁸⁵Y. Nakamura, T. Zhao, J. Xi, W. Shi, D. Wang, and Z. Shuai, "Intrinsic charge transport in stanene: Roles of bucklings and electron-phonon couplings," *Advanced Electronic Materials* **3**, 1700143 (2017).
- ⁸⁶Y. Wu, B. Hou, Y. Chen, J. Cao, H. Shao, Y. Zhang, C. Ma, H. Zhu, R. Zhang, and H. Zhang, "Strong electron-phonon coupling influences carrier transport and thermoelectric performances in group-IV/V elemental monolayers," *npj Computational Materials* **7**, 1–12 (2021).
- ⁸⁷T. Gunst, T. Markussen, K. Stokbro, and M. Brandbyge, "First-principles method for electron-phonon coupling and electron mobility: Applications to two-dimensional materials," *Physical Review B* **93**, 035414 (2016).
- ⁸⁸J. Xi, D. Wang, Y. Yi, and Z. Shuai, "Electron-phonon couplings and carrier mobility in graphynes sheet calculated using the Wannier-interpolation approach," *The Journal of chemical physics* **141**, 034704 (2014).
- ⁸⁹G. Samsonidze and B. Kozinsky, "Accelerated screening of thermoelectric materials by first-principles computations of electron-phonon scattering," *Advanced Energy Materials* **8**, 1800246 (2018).
- ⁹⁰L. Cheng and Y. Liu, "What limits the intrinsic mobility of electrons and holes in two dimensional metal dichalcogenides?" *Journal of the American Chemical Society* **140**, 17895–17900 (2018).
- ⁹¹S.-L. Li, K. Tsukagoshi, E. Orgiu, and P. Samorì, "Charge transport and mobility engineering in two-dimensional transition metal chalcogenide semiconductors," *Chemical Society Reviews* **45**, 118–151 (2016).
- ⁹²T. Sohler, D. Campi, N. Marzari, and M. Gibertini, "Mobility of two-dimensional materials from first principles in an accurate and automated framework," *Physical Review Materials* **2**, 114010 (2018).
- ⁹³L. Cheng, C. Zhang, and Y. Liu, "Why two-dimensional semiconductors generally have low electron mobility," *Physical Review Letters* **125**, 177701 (2020).
- ⁹⁴Y. Zhao, Z. Dai, C. Zhang, C. Lian, S. Zeng, G. Li, S. Meng, and J. Ni, "Intrinsic electronic transport and thermoelectric power factor in n-type doped monolayer mos₂," *New Journal of Physics* **20**, 043009 (2018).
- ⁹⁵Y. Ge, W. Wan, Y. Ren, and Y. Liu, "Large thermoelectric power factor of high-mobility transition-metal dichalcogenides with 1 T'' phase," *Physical Review Research* **2**, 013134 (2020).
- ⁹⁶G. Sharma, V. K. Pandey, S. Datta, and P. Ghosh, "Effect of electron-phonon coupling on the transport properties of monolayers of ZrS₂, BiI₃ and PbI₂: a thermoelectric perspective," *Physical Chemistry Chemical Physics* **23**, 11663–11671 (2021).
- ⁹⁷M. G. Rosul and M. Zebarjadi, "Effect of electron-phonon interaction and ionized impurity scattering on the room-temperature thermoelectric properties of bulk mose₂," *The Journal of Physical Chemistry C* **126**, 15011–15018 (2022).
- ⁹⁸C. Liu, M. Yao, J. Yang, J. Xi, and X. Ke, "Strong electron-phonon interaction induced significant reduction in lattice thermal conductivities for single-layer MoS₂ and PtSSe," *Materials Today Physics* **15**, 100277 (2020).
- ⁹⁹G. A. Slack, "Nonmetallic crystals with high thermal conductivity," *Journal of Physics and Chemistry of Solids* **34**, 321–335 (1973).
- ¹⁰⁰D. Morelli and J. Heremans, "Thermal conductivity of germanium, silicon, and carbon nitrides," *Applied physics letters* **81**, 5126–5128 (2002).
- ¹⁰¹C. Muratore, V. Varshney, J. J. Gengler, J. Hu, J. E. Bultman, T. M. Smith, P. J. Shamberger, B. Qiu, X. Ruan, A. K. Roy, et al., "Cross-plane thermal properties of transition metal dichalcogenides," *Applied Physics Letters* **102**, 081604 (2013).
- ¹⁰²X. Gu, Y. Wei, X. Yin, B. Li, and R. Yang, "Phononic thermal properties of two-dimensional materials," *Rev. Mod. Phys.* **90**, 041002 (2018).
- ¹⁰³Y. Zhang, "First-principles Debye–Callaway approach to lattice thermal conductivity," *Journal of Materiomics* **2**, 237–247 (2016).
- ¹⁰⁴D. Morelli, J. Heremans, and G. Slack, "Estimation of the isotope effect on the lattice thermal conductivity of group IV and group III-V semiconductors," *Physical Review B* **66**, 195304 (2002).
- ¹⁰⁵M. Asen-Palmer, K. Bartkowski, E. Gmelin, M. Cardona, A. Zhernov, A. Inyushkin, A. Taldenkov, V. Ozhogin, K. M. Itoh, and E. Haller, "Thermal conductivity of germanium crystals with different isotopic compositions," *Physical review B* **56**, 9431 (1997).
- ¹⁰⁶T. Fan and A. R. Oganov, "AICON: A program for calculating thermal conductivity quickly and accurately," *Computer Physics Communications* **251**, 107074 (2020).
- ¹⁰⁷F. Q. Wang, J. Yu, Q. Wang, Y. Kawazoe, and P. Jena, "Lattice thermal conductivity of penta-graphene," *Carbon* **105**, 424–429 (2016).
- ¹⁰⁸K. Dabsamut, T. Thanasarnsurapong, T. Maluangnont, T. Jiraroj, S. Jungthawan, A. Boonchun, et al., "Strain engineering and thermal conductivity of a penta-BCN monolayer: a computational study," *Journal of Physics D: Applied Physics* **54**, 355301 (2021).
- ¹⁰⁹D. Nika, E. Pokatilov, A. Askerov, and A. Balandin, "Phonon thermal conduction in graphene: Role of Umklapp and edge roughness scattering," *Physical Review B* **79**, 155413 (2009).
- ¹¹⁰R. D'Souza and S. Mukherjee, "Length-dependent lattice thermal conductivity of single-layer and multilayer hexagonal boron nitride: A first-principles study using the callaway-klemens and real-space supercell methods," *Physical Review B* **96**, 205422 (2017).
- ¹¹¹R. Peierls, "Zur kinetischen theorie der wärmeleitung in kristallen," *Annalen der Physik* **395**, 1055–1101 (1929).
- ¹¹²L. Lindsay, "First principles peierls-boltzmann phonon thermal transport: a topical review," *Nanoscale and Microscale Thermophysical Engineering* **20**, 67–84 (2016).
- ¹¹³D. A. Broido, M. Malorny, G. Birner, N. Mingo, and D. Stewart, "Intrinsic lattice thermal conductivity of semiconductors from first principles," *Applied Physics Letters* **91**, 231922 (2007).
- ¹¹⁴A. Ward, D. Broido, D. A. Stewart, and G. Deinzer, "Ab initio theory of the lattice thermal conductivity in diamond," *Physical Review B* **80**, 125203 (2009).
- ¹¹⁵X. Gu and R. Yang, "Phonon transport in single-layer transition metal dichalcogenides: A first-principles study," *Applied Physics Letters* **105**, 131903 (2014).

- ¹¹⁶X. Gu, B. Li, and R. Yang, "Layer thickness-dependent phonon properties and thermal conductivity of MoS₂," *Journal of Applied Physics* **119**, 085106 (2016).
- ¹¹⁷C. A. Polanco, T. Pandey, T. Berlijn, and L. Lindsay, "Defect-limited thermal conductivity in MoS₂," *Physical Review Materials* **4**, 014004 (2020).
- ¹¹⁸J. Wang and J.-S. Wang, "Carbon nanotube thermal transport: Ballistic to diffusive," *Applied physics letters* **88**, 111909 (2006).
- ¹¹⁹L. Medrano Sandonas, R. Gutierrez, A. Pecchia, A. Croy, and G. Cuniberti, "Quantum phonon transport in nanomaterials: Combining atomistic with non-equilibrium green's function techniques," *Entropy* **21**, 735 (2019).
- ¹²⁰J.-S. Wang, J. Wang, and J. Lü, "Quantum thermal transport in nanostructures," *The European Physical Journal B* **62**, 381–404 (2008).
- ¹²¹Z.-Z. Yu, G.-H. Xiong, and L.-F. Zhang, "A brief review of thermal transport in mesoscopic systems from nonequilibrium Green's function approach," *Frontiers of Physics* **16**, 1–18 (2021).
- ¹²²C. A. Polanco, "Nonequilibrium Green's functions (NEGF) in vibrational energy transport: a topical review," *Nanoscale and Microscale Thermophysical Engineering* **25**, 1–24 (2021).
- ¹²³Y. Xu, J.-S. Wang, W. Duan, B.-L. Gu, and B. Li, "Nonequilibrium Green's function method for phonon-phonon interactions and ballistic-diffusive thermal transport," *Physical Review B* **78**, 224303 (2008).
- ¹²⁴X.-K. Chen, Y.-J. Zeng, and K.-Q. Chen, "Thermal transport in two-dimensional heterostructures," *Frontiers in Materials*, 427 (2020).
- ¹²⁵H. Sevinçli, S. Roche, G. Cuniberti, M. Brandbyge, R. Gutierrez, and L. M. Sandonas, "Green function, quasi-classical rangein and kubo-greenwood methods in quantum thermal transport," *Journal of Physics: Condensed Matter* **31**, 273003 (2019).
- ¹²⁶T. Yamamoto and K. Watanabe, "Nonequilibrium Green's function approach to phonon transport in defective carbon nanotubes," *Physical review letters* **96**, 255503 (2006).
- ¹²⁷N. Mingo and L. Yang, "Phonon transport in nanowires coated with an amorphous material: An atomistic Green's function approach," *Physical Review B* **68**, 245406 (2003).
- ¹²⁸J.-S. Wang, J. Wang, and N. Zeng, "Nonequilibrium Green's function approach to mesoscopic thermal transport," *Physical Review B* **74**, 033408 (2006).
- ¹²⁹J. Turney, A. McGaughey, and C. Amon, "Assessing the applicability of quantum corrections to classical thermal conductivity predictions," *Physical Review B* **79**, 224305 (2009).
- ¹³⁰A. Kandemir, H. Yapicioglu, A. Kinaci, T. Çağın, and C. Sevik, "Thermal transport properties of MoS₂ and MoSe₂ monolayers," *Nanotechnology* **27**, 055703 (2016).
- ¹³¹A. Mobaraki, A. Kandemir, H. Yapicioglu, O. Gülseren, and C. Sevik, "Validation of inter-atomic potential for WS₂ and WSe₂ crystals through assessment of thermal transport properties," *Computational Materials Science* **144**, 92–98 (2018).
- ¹³²A. Mobaraki, C. Sevik, H. Yapicioglu, D. Çakır, and O. Gülseren, "Temperature-dependent phonon spectrum of transition metal dichalcogenides calculated from the spectral energy density: Lattice thermal conductivity as an application," *Physical Review B* **100**, 035402 (2019).
- ¹³³J.-J. Zhou, J. Park, I.-T. Lu, I. Maliyov, X. Tong, and M. Bernardi, "Perturbo: A software package for ab initio electron-phonon interactions, charge transport and ultrafast dynamics," *Computer Physics Communications* **264**, 107970 (2021).
- ¹³⁴P. Giannozzi, S. Baroni, N. Bonini, M. Calandra, R. Car, C. Cavazzoni, D. Ceresoli, G. L. Chiarotti, M. Cococcioni, I. Dabo, et al., "QUANTUM ESPRESSO: a modular and open-source software project for quantum simulations of materials," *Journal of physics: Condensed matter* **21**, 395502 (2009).
- ¹³⁵P. Giannozzi, O. Andreussi, T. Brumme, O. Bunau, M. B. Nardelli, M. Calandra, R. Car, C. Cavazzoni, D. Ceresoli, M. Cococcioni, et al., "Advanced capabilities for materials modelling with Quantum ESPRESSO," *Journal of physics: Condensed matter* **29**, 465901 (2017).
- ¹³⁶N. Marzari, A. A. Mostofi, J. R. Yates, I. Souza, and D. Vanderbilt, "Maximally localized Wannier functions: Theory and applications," *Reviews of Modern Physics* **84**, 1419 (2012).
- ¹³⁷A. A. Mostofi, J. R. Yates, G. Pizzi, Y.-S. Lee, I. Souza, D. Vanderbilt, and N. Marzari, "An updated version of wannier90: A tool for obtaining maximally-localised Wannier functions," *Computer Physics Communications* **185**, 2309–2310 (2014).
- ¹³⁸G. Pizzi, V. Vitale, R. Arita, S. Blügel, F. Freimuth, G. Géranton, M. Gibertini, D. Gresch, C. Johnson, T. Koretsune, et al., "Wannier90 as a community code: new features and applications," *Journal of Physics: Condensed Matter* **32**, 165902 (2020).
- ¹³⁹J.-J. Zhou and M. Bernardi, "Ab initio electron mobility and polar phonon scattering in GaAs," *Physical Review B* **94**, 201201 (2016).
- ¹⁴⁰W. Li, "Electrical transport limited by electron-phonon coupling from Boltzmann transport equation: An ab initio study of Si, Al, and MoS₂," *Physical Review B* **92**, 075405 (2015).
- ¹⁴¹S. Poncé, E. R. Margine, C. Verdi, and F. Giustino, "EPW: Electron-phonon coupling, transport and superconducting properties using maximally localized Wannier functions," *Computer Physics Communications* **209**, 116–133 (2016).
- ¹⁴²J. Noffsinger, F. Giustino, B. D. Malone, C.-H. Park, S. G. Louie, and M. L. Cohen, "Epw: A program for calculating the electron-phonon coupling using maximally localized wannier functions," *Computer Physics Communications* **181**, 2140–2148 (2010).
- ¹⁴³F. Giustino, M. L. Cohen, and S. G. Louie, "Electron-phonon interaction using wannier functions," *Phys. Rev. B* **76**, 165108 (2007).
- ¹⁴⁴H. T. T. Nguyen, V. T. T. Vi, T. V. Vu, N. V. Hieu, D. V. Lu, D. P. Rai, and N. T. T. Binh, "Spin-orbit coupling effect on electronic, optical, and thermoelectric properties of janus ga2sse," *RSC Adv.* **10**, 44785–44792 (2020).
- ¹⁴⁵T. Deng, G. Wu, M. B. Sullivan, Z. M. Wong, K. Hippalgaonkar, J.-S. Wang, and S.-W. Yang, "EPIC STAR: a reliable and efficient approach for phonon-and impurity-limited charge transport calculations," *npj Computational Materials* **6**, 1–11 (2020).
- ¹⁴⁶G. K. Madsen and D. J. Singh, "BoltzTraP. A code for calculating band-structure dependent quantities," *Computer Physics Communications* **175**, 67–71 (2006).
- ¹⁴⁷G. K. Madsen, J. Carrete, and M. J. Verstraete, "BoltzTraP2, a program for interpolating band structures and calculating semi-classical transport coefficients," *Computer Physics Communications* **231**, 140–145 (2018).
- ¹⁴⁸W. Chen, J.-H. Pöhl, G. Hautier, D. Broberg, S. Bajaj, U. Aydemir, Z. M. Gibbs, H. Zhu, M. Asta, G. J. Snyder, et al., "Understanding thermoelectric properties from high-throughput calculations: trends, insights, and comparisons with experiment," *Journal of Materials Chemistry C* **4**, 4414–4426 (2016).
- ¹⁴⁹S. Sarikurt, D. Çakır, M. Keçeli, and C. Sevik, "The influence of surface functionalization on thermal transport and thermoelectric properties of MXene monolayers," *Nanoscale* **10**, 8859–8868 (2018).
- ¹⁵⁰L. Xi, S. Pan, X. Li, Y. Xu, J. Ni, X. Sun, J. Yang, J. Luo, J. Xi, W. Zhu, et al., "Discovery of high-performance thermoelectric chalcogenides through reliable high-throughput material screening," *Journal of the American Chemical Society* **140**, 10785–10793 (2018).
- ¹⁵¹A. M. Ganose, J. Park, A. Faghaninia, R. Woods-Robinson, K. A. Persson, and A. Jain, "Efficient calculation of carrier scattering rates from first principles," *Nature communications* **12**, 1–9 (2021).
- ¹⁵²G. Pizzi, D. Volja, B. Kozinsky, M. Fornari, and N. Marzari, "BoltzWann: A code for the evaluation of thermoelectric and electronic transport properties with a maximally-localized Wannier functions basis," *Computer Physics Communications* **185**, 422–429 (2014).
- ¹⁵³E. A. Moujaes and W. Diery, "Thermoelectric properties of 1T monolayer pristine and Janus Pd dichalcogenides," *Journal of Physics: Condensed Matter* **31**, 455502 (2019).
- ¹⁵⁴X. Li, Z. Zhang, J. Xi, D. J. Singh, Y. Sheng, J. Yang, and W. Zhang, "TransOpt. A code to solve electrical transport properties of semiconductors in constant electron-phonon coupling approximation," *Computational Materials Science* **186**, 110074 (2021).
- ¹⁵⁵A. Cepellotti, J. Coulter, A. Johansson, N. S. Fedorova, and B. Kozinsky, "Phoebe: a collection of Phonon and Electron Boltzmann Equation solvers," *arXiv preprint arXiv:2111.14999* (2021).
- ¹⁵⁶A. Togo, L. Chaput, and I. Tanaka, "Distributions of phonon lifetimes in Brillouin zones," *Physical Review B* **91**, 094306 (2015).
- ¹⁵⁷W. Li, J. Carrete, N. A. Katcho, and N. Mingo, "ShengBTE: A solver of the Boltzmann transport equation for phonons," *Computer Physics Communications* **185**, 1747–1758 (2014).
- ¹⁵⁸W. Diery, "Electronic properties, stability, and lattice thermal conductivity of bulk Janus 3R-PtXY (X, Y = S, Se, Te) transition-metal dichalcogenide,"

- The European Physical Journal B **94**, 1–10 (2021).
- 159 T. Fan and A. R. Oganov, “AICON2: A program for calculating transport properties quickly and accurately,” *Computer Physics Communications* **266**, 108027 (2021).
 - 160 T. Fan and A. R. Oganov, “Discovery of high performance thermoelectric chalcogenides through first-principles high-throughput screening,” *Journal of Materials Chemistry C* **9**, 13226–13235 (2021).
 - 161 N. H. Protik, C. Li, M. Pruneda, D. Broido, and P. Ordejón, “Elphbolt: An ab initio solver for the coupled electron-phonon Boltzmann transport equations,” arXiv preprint arXiv:2109.08547 (2021).
 - 162 N. H. Protik and D. A. Broido, “Coupled transport of phonons and carriers in semiconductors: A case study of n-doped GaAs,” *Physical Review B* **101**, 075202 (2020).
 - 163 N. Papior, N. Lorente, T. Frederiksen, A. García, and M. Brandbyge, “Improvements on non-equilibrium and transport green function techniques: The next-generation transiesta,” *Computer Physics Communications* **212**, 8–24 (2017).
 - 164 J. Ferrer, C. J. Lambert, V. M. García-Suárez, D. Z. Manrique, D. Visontai, L. Oroszlany, R. Rodríguez-Ferradás, I. Grace, S. W. D. Bailey, K. Gillemot, H. Sadeghi, and L. A. Algharagholy, “Gollum: a next-generation simulation tool for electron, thermal and spin transport,” *New Journal of Physics* **16**, 093029 (2014).
 - 165 A. R. Rocha, V. M. García-Suárez, S. Bailey, C. Lambert, J. Ferrer, and S. Sanvito, “Spin and molecular electronics in atomically generated orbital landscapes,” *Phys. Rev. B* **73**, 085414 (2006).
 - 166 T. Ozaki, K. Nishio, H. Weng, and H. Kino, “Dual spin filter effect in a zigzag graphene nanoribbon,” *Phys. Rev. B* **81**, 075422 (2010).
 - 167 C. W. Groth, M. Wimmer, A. R. Akhmerov, and X. Waintal, “Kwant: a software package for quantum transport,” *New Journal of Physics* **16**, 063065 (2014).
 - 168 S. M. João, M. Anđelković, L. Covaci, T. G. Rappoport, J. M. Lopes, and A. Ferreira, “Kite: high-performance accurate modelling of electronic structure and response functions of large molecules, disordered crystals and heterostructures,” *Royal Society Open Science* **7**, 191809 (2020), <https://royalsocietypublishing.org/doi/pdf/10.1098/rsos.191809>.
 - 169 T. D. Kühne, M. Iannuzzi, M. Del Ben, V. V. Rybkin, P. Seewald, F. Stein, T. Laino, R. Z. Khaliullin, O. Schütt, F. Schiffmann, D. Golze, J. Wilhelm, S. Chulkov, M. H. Bani-Hashemian, V. Weber, U. Borštnik, M. Taillefumier, A. S. Jakobovits, A. Lazzaro, H. Pabst, T. Müller, R. Schade, M. Guidon, S. Andermatt, N. Holmberg, G. K. Schenter, A. Hehn, A. Bussy, F. Belleflamme, G. Tabacchi, A. Glöb, M. Lass, I. Bethune, C. J. Mundy, C. Plessl, M. Watkins, J. VandeVondele, M. Krack, and J. Hutter, “Cp2k: An electronic structure and molecular dynamics software package - quickstep: Efficient and accurate electronic structure calculations,” *The Journal of Chemical Physics* **152**, 194103 (2020), <https://doi.org/10.1063/5.0007045>.
 - 170 Y. Wei, X. You, H. Yang, Z. Luan, and D. Qian, “Towards GPU Acceleration of Phonon Computation with ShengBTE,” in *Proceedings of the International Conference on High Performance Computing in Asia-Pacific Region* (2020) pp. 32–42.
 - 171 M. Zulfiqar, Y. Zhao, G. Li, Z. Li, and J. Ni, “Intrinsic thermal conductivities of monolayer transition metal dichalcogenides mx_2 ($m = mo, w; x = s, se, te$),” *Scientific Reports* **9**, 4571 (2019).
 - 172 Y. Hu, T. Yang, D. Li, G. Ding, C. Dun, D. Wu, and X. Wang, “Origins of minimized lattice thermal conductivity and enhanced thermoelectric performance in WS_2/WS_2 lateral superlattice,” *ACS omega* **6**, 7879–7886 (2021).
 - 173 Z. Han, X. Yang, W. Li, T. Feng, and X. Ruan, “FourPhonon: An extension module to ShengBTE for computing four-phonon scattering rates and thermal conductivity,” arXiv preprint arXiv:2104.04895 (2021).
 - 174 T. Feng and X. Ruan, “Quantum mechanical prediction of four-phonon scattering rates and reduced thermal conductivity of solids,” *Physical Review B* **93**, 045202 (2016).
 - 175 A. Togo and I. Tanaka, “First principles phonon calculations in materials science,” *Scripta Materialia* **108**, 1–5 (2015).
 - 176 J. Carrete, B. Vermeersch, A. Katre, A. van Roekeghem, T. Wang, G. K. Madsen, and N. Mingo, “almaBTE: A solver of the space-time dependent Boltzmann transport equation for phonons in structured materials,” *Computer Physics Communications* **220**, 351–362 (2017).
 - 177 B. Vermeersch, J. Carrete, and N. Mingo, “Cross-plane heat conduction in thin films with ab-initio phonon dispersions and scattering rates,” *Applied Physics Letters* **108**, 193104 (2016).
 - 178 P. Chen, N. Katcho, J. Feser, W. Li, M. Glaser, O. Schmidt, D. G. Cahill, N. Mingo, and A. Rastelli, “Role of surface-segregation-driven intermixing on the thermal transport through planar Si/Ge superlattices,” *Physical review letters* **111**, 115901 (2013).
 - 179 B. Vermeersch, J. Carrete, N. Mingo, and A. Shakouri, “Superdiffusive heat conduction in semiconductor alloys. I. Theoretical foundations,” *Physical Review B* **91**, 085202 (2015).
 - 180 G. Barbalinardo, Z. Chen, N. W. Lundgren, and D. Donadio, “Efficient anharmonic lattice dynamics calculations of thermal transport in crystalline and disordered solids,” *Journal of Applied Physics* **128**, 135104 (2020).
 - 181 L. Isaeva, G. Barbalinardo, D. Donadio, and S. Baroni, “Modeling heat transport in crystals and glasses from a unified lattice-dynamical approach,” *Nature communications* **10**, 1–6 (2019).
 - 182 G. Romano, “OpenBTE: a Solver for ab-initio Phonon Transport in Multi-dimensional Structures,” arXiv preprint arXiv:2106.02764 (2021).
 - 183 G. Romano, “Phonon Transport in Patterned Two-Dimensional Materials from First Principles,” arXiv preprint arXiv:2002.08940 (2020).
 - 184 T. Tadano, Y. Gohda, and S. Tsuneyuki, “Anharmonic force constants extracted from first-principles molecular dynamics: applications to heat transfer simulations,” *Journal of Physics: Condensed Matter* **26**, 225402 (2014).
 - 185 T. Tadano and S. Tsuneyuki, “Self-consistent phonon calculations of lattice dynamical properties in cubic $SrTiO_3$ with first-principles anharmonic force constants,” *Physical Review B* **92**, 054301 (2015).
 - 186 N. Werthamer, “Self-consistent phonon formulation of anharmonic lattice dynamics,” *Physical Review B* **1**, 572 (1970).
 - 187 F. Eriksson, E. Fransson, and P. Erhart, “The Hiphive Package for the Extraction of High-Order Force Constants by Machine Learning,” *Advanced Theory and Simulations* **2**, 1800184 (2019).
 - 188 A. H. Larsen, J. J. Mortensen, J. Blomqvist, I. E. Castelli, R. Christensen, M. Dulak, J. Friis, M. N. Groves, B. Hammer, C. Hargus, et al., “The atomic simulation environment—a Python library for working with atoms,” *Journal of Physics: Condensed Matter* **29**, 273002 (2017).
 - 189 R. Gupta, B. Dongre, C. Bera, and J. Carrete, “The effect of Janus asymmetry on thermal transport in SnS_2 ,” *The Journal of Physical Chemistry C* **124**, 17476–17484 (2020).
 - 190 L. Pan, J. Carrete, and Z. Wang, “Strain-tunable lattice thermal conductivity of the Janus PtSe monolayer,” *Journal of Physics: Condensed Matter* **34**, 015303 (2021).
 - 191 Z. Zeng, Z. Yin, X. Huang, H. Li, Q. He, G. Lu, F. Boey, and H. Zhang, “Single-layer semiconducting nanosheets: high-yield preparation and device fabrication,” *Angewandte Chemie* **123**, 11289–11293 (2011).
 - 192 M. Zhang, Y. Zhu, X. Wang, Q. Feng, S. Qiao, W. Wen, Y. Chen, M. Cui, J. Zhang, C. Cai, et al., “Controlled synthesis of ZrS_2 monolayer and few layers on hexagonal boron nitride,” *Journal of the American Chemical Society* **137**, 7051–7054 (2015).
 - 193 A. Padilla, R. R. Rugh, and D. Joubert, “Mechanical, thermal and thermoelectric properties of MX_2 ($M = Zr, Hf; X = S, Se$),” *Materials Today Communications* **25**, 101434 (2020).
 - 194 D. Singh and R. Ahuja, “Enhanced optoelectronic and thermoelectric properties by intrinsic structural defects in monolayer HfS_2 ,” *ACS Applied Energy Materials* **2**, 6891–6903 (2019).
 - 195 J. Bera, A. Betal, and S. Sahu, “Spin orbit coupling induced enhancement of thermoelectric performance of HfX_2 ($X = S, Se$) and its Janus monolayer,” *Journal of Alloys and Compounds* **872**, 159704 (2021).
 - 196 J. Xiang, H. Wang, B. Dai, W.-L. Cheng, X.-W. Zhang, Z.-G. Wang, and N.-N. Ge, “Optimizing the thermoelectric transmission of monolayer $hfse_2$ by strain engineering,” *Journal of Physics and Chemistry of Solids* , 110834 (2022).
 - 197 J. Tseng and X. Luo, “First-principles investigation of low-dimension MSe_2 ($M = Ti, Hf, Zr$) configurations as promising thermoelectric materials,” *Journal of Physics and Chemistry of Solids* **139**, 109322 (2020).
 - 198 R. Bhatt, S. Bhattacharya, R. Basu, S. Ahmad, A. Chauhan, G. Okram, P. Bhatt, M. Roy, M. Navaneethan, Y. Hayakawa, et al., “Enhanced thermoelectric properties of selenium-deficient layered $TiSe_{2-x}$: A charge-density-wave material,” *ACS applied materials & interfaces* **6**, 18619–18625 (2014).
 - 199 G. Li, K. Yao, and G. Gao, “Strain-induced enhancement of thermoelec-

- tric performance of TiS_2 monolayer based on first-principles phonon and electron band structures,” *Nanotechnology* **29**, 015204 (2017).
- ²⁰⁰Y. Gu, K. Song, X. Hu, C. Chen, L. Pan, C. Lu, X. Shen, K. Koumoto, and Y. Wang, “Realization of an Ultrahigh Power Factor and Enhanced Thermoelectric Performance in TiS_2 via Microstructural Texture Engineering,” *ACS Applied Materials & Interfaces* **12**, 41687–41695 (2020).
- ²⁰¹L. Wang, Z. Zhang, L. Geng, T. Yuan, Y. Liu, J. Guo, L. Fang, J. Qiu, and S. Wang, “Solution-printable fullerene/ TiS_2 organic/inorganic hybrids for high-performance flexible n-type thermoelectrics,” *Energy & Environmental Science* **11**, 1307–1317 (2018).
- ²⁰²C. Wan, X. Gu, F. Dang, T. Itoh, Y. Wang, H. Sasaki, M. Kondo, K. Koga, K. Yabuki, G. J. Snyder, et al., “Flexible n-type thermoelectric materials by organic intercalation of layered transition metal dichalcogenide TiS_2 ,” *Nature materials* **14**, 622–627 (2015).
- ²⁰³S. N. Sadeghi, M. Zabarjadi, and K. Esfarjani, “Non-linear enhancement of thermoelectric performance of a TiSe_2 monolayer due to tensile strain, from first-principles calculations,” *Journal of Materials Chemistry C* **7**, 7308–7317 (2019).
- ²⁰⁴F. Khan, H. Din, S. Khan, G. Rehman, M. Bilal, C. V. Nguyen, I. Ahmad, L.-Y. Gan, and B. Amin, “Theoretical investigation of electronic structure and thermoelectric properties of MX_2 ($\text{M}=\text{Zr, Hf}$; $\text{X}=\text{S, Se}$) van der Waals heterostructures,” *Journal of Physics and Chemistry of Solids* **126**, 304–309 (2019).
- ²⁰⁵G. Ding, C. Wang, G. Gao, K. Yao, C. Dun, C. Feng, D. Li, and G. Zhang, “Engineering of charge carriers via a two-dimensional heterostructure to enhance the thermoelectric figure of merit,” *Nanoscale* **10**, 7077–7084 (2018).
- ²⁰⁶S. E. Rezaei, M. Zabarjadi, and K. Esfarjani, “Effect of exchange-correlation functional type and spin-orbit coupling on thermoelectric properties of ZrTe_2 ,” *Journal of Solid State Chemistry* **302**, 122414 (2021).
- ²⁰⁷S.-D. Guo, Y.-F. Li, and X.-S. Guo, “Predicted Janus monolayer ZrSSe with enhanced n-type thermoelectric properties compared with monolayer ZrS_2 ,” *Computational Materials Science* **161**, 16–23 (2019).
- ²⁰⁸S. Ahmad, F. Khan, B. Amin, and I. Ahmad, “Effect of strain on structural and electronic properties, and thermoelectric response of MXY ($\text{M}=\text{Zr, Hf}$ and Pt ; $\text{X/Y}=\text{S, Se}$) vdW heterostructures; A first principles study,” *Journal of Solid State Chemistry* **299**, 122189 (2021).
- ²⁰⁹H. Wang, B. Dai, N.-N. Ge, X.-W. Zhang, and G.-F. Ji, “High thermoelectric performance of janus monolayer and bilayer hfsse ,” *physica status solidi (b)*, 2200090 (2022).
- ²¹⁰D. Hoat, M. Naseri, N. N. Hieu, R. Ponce-Pérez, J. Rivas-Silva, T. V. Vu, and G. H. Cocolezzi, “A comprehensive investigation on electronic structure, optical and thermoelectric properties of the HfSSe Janus monolayer,” *Journal of Physics and Chemistry of Solids* **144**, 109490 (2020).
- ²¹¹M. Buscema, M. Barkelid, V. Zwiller, H. S. van der Zant, G. A. Steele, and A. Castellanos-Gomez, “Large and tunable photothermoelectric effect in single-layer MoS_2 ,” *Nano letters* **13**, 358–363 (2013).
- ²¹²B. W. Baugher, H. O. Churchill, Y. Yang, and P. Jarillo-Herrero, “Intrinsic electronic transport properties of high-quality monolayer and bilayer MoS_2 ,” *Nano letters* **13**, 4212–4216 (2013).
- ²¹³S. Sahoo, A. P. Gaur, M. Ahmadi, M. J.-F. Guinel, and R. S. Katiyar, “Temperature-dependent Raman studies and thermal conductivity of few-layer MoS_2 ,” *The Journal of Physical Chemistry C* **117**, 9042–9047 (2013).
- ²¹⁴R. Yan, J. R. Simpson, S. Bertolazzi, J. Brivio, M. Watson, X. Wu, A. Kis, T. Luo, A. R. Hight Walker, and H. G. Xing, “Thermal conductivity of monolayer molybdenum disulfide obtained from temperature-dependent Raman spectroscopy,” *ACS Nano* **8**, 986–993 (2014).
- ²¹⁵I. Jo, M. T. Pettes, E. Ou, W. Wu, and L. Shi, “Basal-plane thermal conductivity of few-layer molybdenum disulfide,” *Applied Physics Letters* **104**, 201902 (2014).
- ²¹⁶J. Wu, H. Schmidt, K. K. Amara, X. Xu, G. Eda, and B. Özyilmaz, “Large thermoelectricity via variable range hopping in chemical vapor deposition grown single-layer MoS_2 ,” *Nano letters* **14**, 2730–2734 (2014).
- ²¹⁷N. Peimyoo, J. Shang, W. Yang, Y. Wang, C. Cong, and T. Yu, “Thermal conductivity determination of suspended mono- and bilayer WS_2 by Raman spectroscopy,” *Nano Research* **8**, 1210–1221 (2015).
- ²¹⁸X. Zhang, D. Sun, Y. Li, G.-H. Lee, X. Cui, D. Chenet, Y. You, T. F. Heinz, and J. C. Hone, “Measurement of lateral and interfacial thermal conductivity of single- and bilayer MoS_2 and MoSe_2 using refined optothermal Raman technique,” *ACS applied materials & interfaces* **7**, 25923–25929 (2015).
- ²¹⁹A. Taube, J. Judek, A. Łapinska, and M. Zdrojek, “Temperature-dependent thermal properties of supported MoS_2 monolayers,” *ACS applied materials & interfaces* **7**, 5061–5065 (2015).
- ²²⁰P. Jiang, X. Qian, X. Gu, and R. Yang, “Probing anisotropic thermal conductivity of transition metal dichalcogenides mx_2 ($\text{m}=\text{mo, w}$ and $\text{x}=\text{s, se}$) using time-domain thermoreflectance,” *Advanced Materials* **29**, 1701068 (2017).
- ²²¹E. Easy, Y. Gao, Y. Wang, D. Yan, S. M. Gousheghir, E.-H. Yang, B. Xu, and X. Zhang, “Experimental and Computational Investigation of Layer-Dependent Thermal Conductivities and Interfacial Thermal Conductance of One-to Three-Layer WSe_2 ,” *ACS Applied Materials & Interfaces* **13**, 13063–13071 (2021).
- ²²²R. Wang, T. Wang, H. Zobeiri, P. Yuan, C. Deng, Y. Yue, S. Xu, and X. Wang, “Measurement of the thermal conductivities of suspended MoS_2 and MoSe_2 by nanosecond ET-Raman without temperature calibration and laser absorption evaluation,” *Nanoscale* **10**, 23087–23102 (2018).
- ²²³H. Babaei, J. Khodadadi, and S. Sinha, “Large theoretical thermoelectric power factor of suspended single-layer MoS_2 ,” *Applied Physics Letters* **105**, 193901 (2014).
- ²²⁴Z. Luo, J. Maassen, Y. Deng, Y. Du, R. P. Garrelts, M. S. Lundstrom, D. Y. Peide, and X. Xu, “Anisotropic in-plane thermal conductivity observed in few-layer black phosphorus,” *Nature communications* **6**, 1–8 (2015).
- ²²⁵M. T. Pettes, J. Maassen, I. Jo, M. S. Lundstrom, and L. Shi, “Effects of surface band bending and scattering on thermoelectric transport in suspended bismuth telluride nanoplates,” *Nano letters* **13**, 5316–5322 (2013).
- ²²⁶M.-S. Kang, S.-Y. Kang, W.-Y. Lee, N.-W. Park, K. C. Kown, S. Choi, G.-S. Kim, J. Nam, K. S. Kim, E. Saitoh, et al., “Large-scale MoS_2 thin films with a chemically formed holey structure for enhanced Seebeck thermopower and their anisotropic properties,” *Journal of Materials Chemistry A* **8**, 8669–8677 (2020).
- ²²⁷J. Liu, G.-M. Choi, and D. G. Cahill, “Measurement of the anisotropic thermal conductivity of molybdenum disulfide by the time-resolved magneto-optic Kerr effect,” *Journal of Applied Physics* **116**, 233107 (2014).
- ²²⁸P. Yuan, R. Wang, T. Wang, X. Wang, and Y. Xie, “Nonmonotonic thickness-dependence of in-plane thermal conductivity of few-layered mo_2 : 2.4 to 37.8 nm,” *Physical Chemistry Chemical Physics* **20**, 25752–25761 (2018).
- ²²⁹H. S. Choe, R. Prabhakar, G. Wehmeyer, F. I. Allen, W. Lee, L. Jin, Y. Li, P. Yang, C.-W. Qiu, C. Dames, et al., “Ion write microthermotics: Programming thermal metamaterials at the microscale,” *Nano letters* **19**, 3830–3837 (2019).
- ²³⁰Y. Zhao, M. Zheng, J. Wu, B. Huang, and J. T. Thong, “Studying thermal transport in suspended monolayer molybdenum disulfide prepared by a nano-manipulator-assisted transfer method,” *Nanotechnology* **31**, 225702 (2020).
- ²³¹C. Lee, J. Hong, M.-H. Whangbo, and J. H. Shim, “Enhancing the thermoelectric properties of layered transition-metal dichalcogenides 2H-MQ_2 ($\text{M}=\text{Mo, W}$; $\text{Q}=\text{S, Se, Te}$) by layer mixing: density functional investigation,” *Chemistry of Materials* **25**, 3745–3752 (2013).
- ²³²J.-W. Jiang, H. S. Park, and T. Rabczuk, “Molecular dynamics simulations of single-layer molybdenum disulfide (MoS_2): Stillinger-Weber parametrization, mechanical properties, and thermal conductivity,” *Journal of Applied Physics* **114**, 064307 (2013).
- ²³³D. Çakır, F. M. Peeters, and C. Sevik, “Mechanical and thermal properties of h-MX_2 ($\text{M}=\text{Cr, Mo, W}$; $\text{X}=\text{O, S, Se, Te}$) monolayers: A comparative study,” *Applied Physics Letters* **104**, 203110 (2014).
- ²³⁴S.-D. Guo and J.-L. Wang, “Spin-orbital coupling effect on the power factor in semiconducting transition-metal dichalcogenide monolayers,” *Semiconductor Science and Technology* **31**, 095011 (2016).
- ²³⁵C. Adessi, S. Thebaud, R. Bouzerar, and G. Bouzerar, “First principle investigation on thermoelectric properties of transition metal dichalcogenides: beyond the rigid band model,” *The Journal of Physical Chemistry C* **121**, 12577–12584 (2017).
- ²³⁶G. Zhang and Y.-W. Zhang, “Thermoelectric properties of two-dimensional transition metal dichalcogenides,” *Journal of Materials Chemistry C* **5**, 7684–7698 (2017).
- ²³⁷W. Zhou, H. Gong, X. Jin, Y. Chen, H. Li, and S. Liu, “Recent progress of

- two-dimensional transition metal dichalcogenides for thermoelectric applications,” *Frontiers in Physics*, **67** (2022).
- ²³⁸X. Wei, Y. Wang, Y. Shen, G. Xie, H. Xiao, J. Zhong, and G. Zhang, “Phonon thermal conductivity of monolayer MoS₂: A comparison with single layer graphene,” *Applied Physics Letters* **105**, 103902 (2014).
- ²³⁹A. A. Balandin, S. Ghosh, W. Bao, I. Calizo, D. Teweldebrhan, F. Miao, and C. N. Lau, “Superior thermal conductivity of single-layer graphene,” *Nano letters* **8**, 902–907 (2008).
- ²⁴⁰Y. Cai, J. Lan, G. Zhang, and Y.-W. Zhang, “Lattice vibrational modes and phonon thermal conductivity of monolayer MoS₂,” *Physical Review B* **89**, 035438 (2014).
- ²⁴¹X. Liu, G. Zhang, Q.-X. Pei, and Y.-W. Zhang, “Phonon thermal conductivity of monolayer MoS₂ sheet and nanoribbons,” *Applied Physics Letters* **103**, 133113 (2013).
- ²⁴²D. Fan, H. Liu, L. Cheng, P. Jiang, J. Shi, and X. Tang, “MoS₂ nanoribbons as promising thermoelectric materials,” *Applied physics letters* **105**, 133113 (2014).
- ²⁴³W. Li, J. Carrete, and N. Mingo, “Thermal conductivity and phonon linewidths of monolayer MoS₂ from first principles,” *Applied Physics Letters* **103**, 253103 (2013).
- ²⁴⁴Z. Jin, Q. Liao, H. Fang, Z. Liu, W. Liu, Z. Ding, T. Luo, and N. Yang, “A revisit to high thermoelectric performance of single-layer MoS₂,” *Scientific reports* **5**, 1–7 (2015).
- ²⁴⁵A. N. Gandi and U. Schwingenschlögl, “Thermal conductivity of bulk and monolayer MoS₂,” *EPL (Europhysics Letters)* **113**, 36002 (2016).
- ²⁴⁶Y. Hong, J. Zhang, and X. C. Zeng, “Thermal conductivity of monolayer MoSe₂ and MoS₂,” *The Journal of Physical Chemistry C* **120**, 26067–26075 (2016).
- ²⁴⁷B. Peng, H. Zhang, H. Shao, Y. Xu, X. Zhang, and H. Zhu, “Thermal conductivity of monolayer MoS₂, MoSe₂, and WS₂: interplay of mass effect, interatomic bonding and anharmonicity,” *RSC advances* **6**, 5767–5773 (2016).
- ²⁴⁸W. Huang, H. Da, and G. Liang, “Thermoelectric performance of MX₂ (M= Mo, W; X= S,Se) monolayers,” *Journal of Applied Physics* **113**, 104304 (2013).
- ²⁴⁹W. Huang, X. Luo, C. K. Gan, S. Y. Quek, and G. Liang, “Theoretical study of thermoelectric properties of few-layer MoS₂ and WSe₂,” *Physical Chemistry Chemical Physics* **16**, 10866–10874 (2014).
- ²⁵⁰C. Chiritescu, D. G. Cahill, N. Nguyen, D. Johnson, A. Bodapati, P. Keblinski, and P. Zschack, “Ultralow thermal conductivity in disordered, layered WSe₂ crystals,” *Science* **315**, 351–353 (2007).
- ²⁵¹V. Varshney, S. S. Patnaik, C. Muratore, A. K. Roy, A. A. Voevodin, and B. L. Farmer, “MD simulations of molybdenum disulphide (MoS₂): Force-field parameterization and thermal transport behavior,” *Computational Materials Science* **48**, 101–108 (2010).
- ²⁵²D. Wickramaratne, F. Zahid, and R. K. Lake, “Electronic and thermoelectric properties of few-layer transition metal dichalcogenides,” *The Journal of chemical physics* **140**, 124710 (2014).
- ²⁵³M. R. Jobayr and E. M. Salman, “Investigation of the thermoelectric properties of one-layer Transition Metal Dichalcogenides,” *Chinese Journal of Physics* (2021).
- ²⁵⁴E. Revolinsky and D. Beerntsen, “Electrical properties of the mote2- wt2 and mote2- wse2 systems,” *Journal of Applied Physics* **35**, 2086–2089 (1964).
- ²⁵⁵S. El-Mahalawy and B. Evans, “Temperature dependence of the electrical conductivity and hall coefficient in 2H-MoS₂, MoSe₂, WSe₂, and MoTe₂,” *physica status solidi (b)* **79**, 713–722 (1977).
- ²⁵⁶W.-X. Zhou and K.-Q. Chen, “First-principles determination of ultralow thermal conductivity of monolayer WSe₂,” *Scientific reports* **5**, 1–8 (2015).
- ²⁵⁷J.-W. Jiang, X. Zhuang, and T. Rabczuk, “Orientation dependent thermal conductance in single-layer mos₂,” *Scientific reports* **3**, 1–4 (2013).
- ²⁵⁸Z. Zhang, Y. Xie, Y. Ouyang, and Y. Chen, “A systematic investigation of thermal conductivities of transition metal dichalcogenides,” *International Journal of Heat and Mass Transfer* **108**, 417–422 (2017).
- ²⁵⁹J. Ma, W. Li, and X. Luo, “Ballistic thermal transport in monolayer transition-metal dichalcogenides: role of atomic mass,” *Applied Physics Letters* **108**, 082102 (2016).
- ²⁶⁰Y. Ouyang and J. Guo, “A theoretical study on thermoelectric properties of graphene nanoribbons,” *Applied Physics Letters* **94**, 263107 (2009).
- ²⁶¹H. Zhang, G. Lee, and K. Cho, “Thermal transport in graphene and effects of vacancy defects,” *Physical Review B* **84**, 115460 (2011).
- ²⁶²S. Chen, Q. Wu, C. Mishra, J. Kang, H. Zhang, K. Cho, W. Cai, A. A. Balandin, and R. S. Ruoff, “Thermal conductivity of isotopically modified graphene,” *Nature materials* **11**, 203–207 (2012).
- ²⁶³H.-p. Li and R.-q. Zhang, “Vacancy-defect-induced diminution of thermal conductivity in silicene,” *EPL (Europhysics Letters)* **99**, 36001 (2012).
- ²⁶⁴B. Liu, C. Reddy, J. Jiang, H. Zhu, J. A. Baimova, S. V. Dmitriev, and K. Zhou, “Thermal conductivity of silicene nanosheets and the effect of isotopic doping,” *Journal of Physics D: Applied Physics* **47**, 165301 (2014).
- ²⁶⁵S. V. Ovsvannikov, V. V. Shchennikov, G. V. Vorontsov, A. Y. Manakov, A. Y. Likhacheva, and V. A. Kulbachinskii, “Giant improvement of thermoelectric power factor of Bi₂Te₃ under pressure,” *Journal of Applied Physics* **104**, 053713 (2008).
- ²⁶⁶H. Lv, W. Lu, D. Shao, and Y. Sun, “Enhanced thermoelectric performance of phosphorene by strain-induced band convergence,” *Physical Review B* **90**, 085433 (2014).
- ²⁶⁷J. Bera and S. Sahu, “Strain induced valley degeneracy: A route to the enhancement of thermoelectric properties of monolayer ws₂,” *RSC advances* **9**, 25216–25224 (2019).
- ²⁶⁸Z. Ding, Q.-X. Pei, J.-W. Jiang, and Y.-W. Zhang, “Manipulating the thermal conductivity of monolayer MoS₂ via lattice defect and strain engineering,” *The Journal of Physical Chemistry C* **119**, 16358–16365 (2015).
- ²⁶⁹B. Peng, Z. Ning, H. Zhang, H. Shao, Y. Xu, G. Ni, and H. Zhu, “Beyond perturbation: role of vacancy-induced localized phonon states in thermal transport of monolayer mos₂,” *The Journal of Physical Chemistry C* **120**, 29324–29331 (2016).
- ²⁷⁰Z. Yan, M. Yoon, and S. Kumar, “Influence of defects and doping on phonon transport properties of monolayer mose₂,” *2D Materials* **5**, 031008 (2018).
- ²⁷¹M. Sharma, A. Kumar, and P. Ahluwalia, “Electron transport and thermoelectric performance of defected monolayer MoS₂,” *Physica E: Low-dimensional Systems and Nanostructures* **107**, 117–123 (2019).
- ²⁷²C. Adessi, S. Pecorario, S. Thebaud, and G. Bouzerar, “First principle investigation of the influence of sulfur vacancies on thermoelectric properties of single layered mos₂,” *Physical Chemistry Chemical Physics* **22**, 15048–15057 (2020).
- ²⁷³R. Kumar, “Ab initio study of effect of Se vacancies on the electronic and thermoelectric properties of the two-dimensional MoSe₂ monolayer,” *Applied Physics A* **127**, 1–7 (2021).
- ²⁷⁴S.-D. Guo, “Spin-orbit and strain effect on power factor in monolayer MoS₂,” *Computational Materials Science* **123**, 8–13 (2016).
- ²⁷⁵D. Han, H. Sun, W. Ding, Y. Chen, X. Wang, and L. Cheng, “Effect of biaxial strain on thermal transport in WS₂ monolayer from first principles calculations,” *Physica E: Low-dimensional Systems and Nanostructures* **124**, 114312 (2020).
- ²⁷⁶A. Aiyiti, S. Hu, C. Wang, Q. Xi, Z. Cheng, M. Xia, Y. Ma, J. Wu, J. Guo, Q. Wang, et al., “Thermal conductivity of suspended few-layer MoS₂,” *Nanoscale* **10**, 2727–2734 (2018).
- ²⁷⁷Y. Zhao, M. Zheng, J. Wu, X. Guan, A. Swardi, Y. Li, M. Lal, G. Xie, G. Zhang, L. Zhang, et al., “Modification of thermal transport in few-layer MoS₂ by atomic-level defects engineering,” *Nanoscale* (2021).
- ²⁷⁸S.-D. Guo, “Phonon transport in Janus monolayer MoSSe: a first-principles study,” *Physical Chemistry Chemical Physics* **20**, 7236–7242 (2018).
- ²⁷⁹M. Vallinayagam, M. Posselt, and S. Chandra, “Electronic structure and thermoelectric properties of Mo-based dichalcogenide monolayers locally and randomly modified by substitutional atoms,” *RSC Advances* **10**, 43035–43044 (2020).
- ²⁸⁰A. Shafique and Y.-H. Shin, “Strain engineering of phonon thermal transport properties in monolayer 2h-mote₂,” *Physical Chemistry Chemical Physics* **19**, 32072–32078 (2017).
- ²⁸¹A. Patel, D. Singh, Y. Sonvane, P. Thakor, and R. Ahuja, “High thermoelectric performance in two-dimensional Janus monolayer material WS-X (X= Se and Te),” *ACS applied materials & interfaces* **12**, 46212–46219 (2020).
- ²⁸²R. Chaurasiya, S. Tyagi, N. Singh, S. Auluck, and A. Dixit, “Enhancing thermoelectric properties of Janus WSSe monolayer by inducing strain mediated valley degeneracy,” *Journal of Alloys and Compounds* **855**,

- 157304 (2021).
- ²⁸³J. Zhang, Y. Hong, X. Wang, Y. Yue, D. Xie, J. Jiang, Y. Xiong, and P. Li, "Phonon thermal properties of transition-metal dichalcogenides MoS₂ and MoSe₂ heterostructure," *The Journal of Physical Chemistry C* **121**, 10336–10344 (2017).
- ²⁸⁴J.-J. Ma, J.-J. Zheng, X.-L. Zhu, P.-F. Liu, W.-D. Li, and B.-T. Wang, "First-principles calculations of thermal transport properties in MoS₂/MoSe₂ bilayer heterostructure," *Physical Chemistry Chemical Physics* **21**, 10442–10448 (2019).
- ²⁸⁵S. Deng, L. Li, O. J. Guy, and Y. Zhang, "Enhanced thermoelectric performance of monolayer MoSSe, bilayer MoSSe and graphene/MoSSe heterogeneous nanoribbons," *Physical Chemistry Chemical Physics* **21**, 18161–18169 (2019).
- ²⁸⁶W. Zhang, J.-Y. Yang, and L. Liu, "Strong interfacial interactions induced a large reduction in lateral thermal conductivity of transition-metal dichalcogenide superlattices," *RSC advances* **9**, 1387–1393 (2019).
- ²⁸⁷M. Zhang, G. Tang, Y. Li, B. Fu, and X. Wang, "Phonon thermal properties of heterobilayers with a molecular dynamics study," *International Journal of Thermophysics* **41**, 1–18 (2020).
- ²⁸⁸S. Bharadwaj, A. Ramasubramaniam, and L. Ram-Mohan, "Lateral transition metal dichalcogenide heterostructures for high efficiency thermoelectric devices," arXiv preprint arXiv:2012.02056 (2020).
- ²⁸⁹Y. Luo, W.-L. Tao, C.-E. Hu, Y. Cheng, and G.-F. Ji, "First-principles study on band gaps and transport properties of van der Waals WSe₂/WTe₂ heterostructure," *Zeitschrift für Naturforschung A* **76**, 361–370 (2021).
- ²⁹⁰Z. Chang, K. Yuan, Z. Sun, X. Zhang, Y. Gao, X. Gong, and D. Tang, "First-principles analysis of phonon thermal transport properties of two-dimensional WS₂/WSe₂ heterostructures," *Chinese Physics B* **30**, 034401 (2021).
- ²⁹¹X. Zhao, G. Tang, Y. Li, M. Zhang, and Y. Nie, "Biaxial Strain Improving the Thermoelectric Performance of a Two-Dimensional MoS₂/WS₂ Heterostructure," *ACS Applied Electronic Materials* **3**, 2995–3004 (2021).
- ²⁹²L. Pi, L. Li, K. Liu, Q. Zhang, H. Li, and T. Zhai, "Recent progress on 2D noble-transition-metal dichalcogenides," *Advanced Functional Materials* **29**, 1904932 (2019).
- ²⁹³A. D. Oyedele, S. Yang, L. Liang, A. A. Puzosky, K. Wang, J. Zhang, P. Yu, P. R. Pudasaini, A. W. Ghosh, Z. Liu, et al., "PdSe₂: pentagonal two-dimensional layers with high air stability for electronics," *Journal of the American Chemical Society* **139**, 14090–14097 (2017).
- ²⁹⁴Y. Wang, L. Li, W. Yao, S. Song, J. Sun, J. Pan, X. Ren, C. Li, E. Okunishi, Y.-Q. Wang, et al., "Monolayer PtSe₂, a new semiconducting transition-metal-dichalcogenide, epitaxially grown by direct selenization of Pt," *Nano letters* **15**, 4013–4018 (2015).
- ²⁹⁵Y. Zhao, J. Qiao, P. Yu, Z. Hu, Z. Lin, S. P. Lau, Z. Liu, W. Ji, and Y. Chai, "Extraordinarily strong interlayer interaction in 2D layered PtS₂," *Advanced materials* **28**, 2399–2407 (2016).
- ²⁹⁶C. Liu, C.-S. Lian, M.-H. Liao, Y. Wang, Y. Zhong, C. Ding, W. Li, C.-L. Song, K. He, X.-C. Ma, et al., "Two-dimensional superconductivity and topological states in PdTe₂ thin films," *Physical Review Materials* **2**, 094001 (2018).
- ²⁹⁷Y. Gong, Z. Lin, Y.-X. Chen, Q. Khan, C. Wang, B. Zhang, G. Nie, N. Xie, and D. Li, "Two-Dimensional Platinum Diselenide: Synthesis, Emerging Applications, and Future Challenges," *Nano-Micro Letters* **12**, 1–34 (2020).
- ²⁹⁸Y. Zhao, J. Qiao, Z. Yu, P. Yu, K. Xu, S. P. Lau, W. Zhou, Z. Liu, X. Wang, W. Ji, et al., "High-electron-mobility and air-stable 2d layered ptse2 fets," *Advanced Materials* **29**, 1604230 (2017).
- ²⁹⁹T.-Y. Su, H. Medina, Y.-Z. Chen, S.-W. Wang, S.-S. Lee, Y.-C. Shih, C.-W. Chen, H.-C. Kuo, F.-C. Chuang, and Y.-L. Chueh, "Phase-engineered ptse2-layered films by a plasma-assisted selenization process toward all ptse2-based field effect transistor to highly sensitive, flexible, and wide-spectrum photoresponse photodetectors," *Small* **14**, 1800032 (2018).
- ³⁰⁰Q. Liang, Q. Wang, Q. Zhang, J. Wei, S. X. Lim, R. Zhu, J. Hu, W. Wei, C. Lee, C. Sow, et al., "High-performance, room temperature, ultra-broadband photodetectors based on air-stable pdse2," *Advanced Materials* **31**, 1807609 (2019).
- ³⁰¹M. Long, Y. Wang, P. Wang, X. Zhou, H. Xia, C. Luo, S. Huang, G. Zhang, H. Yan, Z. Fan, et al., "Palladium diselenide long-wavelength infrared photodetector with high sensitivity and stability," *ACS nano* **13**, 2511–2519 (2019).
- ³⁰²X. Chia, Z. Sofer, J. Luxa, and M. Pumera, "Layered noble metal dichalcogenides: tailoring electrochemical and catalytic properties," *ACS applied materials & interfaces* **9**, 25587–25599 (2017).
- ³⁰³H. Huang, X. Fan, D. J. Singh, and W. Zheng, "Modulation of hydrogen evolution catalytic activity of basal plane in monolayer platinum and palladium dichalcogenides," *ACS omega* **3**, 10058–10065 (2018).
- ³⁰⁴M. Sajjad, E. Montes, N. Singh, and U. Schwingenschlögl, "Superior gas sensing properties of monolayer ptse2," *Advanced Materials Interfaces* **4**, 1600911 (2017).
- ³⁰⁵S. Wagner, C. Yim, N. McEvoy, S. Kataria, V. Yokaribas, A. Kuc, S. Pindl, C.-P. Fritzen, T. Heine, G. S. Duesberg, et al., "Highly sensitive electromechanical piezoresistive pressure sensors based on large-area layered ptse2 films," *Nano letters* **18**, 3738–3745 (2018).
- ³⁰⁶Z. Kahraman, A. Kandemir, M. Yagmurcukardes, and H. Sahin, "Single-layer Janus-type platinum dichalcogenides and their heterostructures," *The Journal of Physical Chemistry C* **123**, 4549–4557 (2019).
- ³⁰⁷Y. Wang, Y. Li, and Z. Chen, "Not your familiar two dimensional transition metal disulfide: structural and electronic properties of the pds 2 monolayer," *Journal of Materials Chemistry C* **3**, 9603–9608 (2015).
- ³⁰⁸J. Sun, H. Shi, T. Siegrist, and D. J. Singh, "Electronic, transport, and optical properties of bulk and mono-layer PdSe₂," *Applied Physics Letters* **107**, 153902 (2015).
- ³⁰⁹Y.-S. Lan, X.-R. Chen, C.-E. Hu, Y. Cheng, and Q.-F. Chen, "Penta-PdX₂ (X= S, Se, Te) monolayers: promising anisotropic thermoelectric materials," *Journal of Materials Chemistry A* **7**, 11134–11142 (2019).
- ³¹⁰S. Ahmad and S. Mahanti, "Energy and temperature dependence of relaxation time and Wiedemann-Franz law on PbTe," *Physical Review B* **81**, 165203 (2010).
- ³¹¹Q. Zhong, Z. Dai, J. Liu, Y. Zhao, and S. Meng, "A comprehensive phonon thermal transport study of 2D hexagonal MX₂ and orthorhombic M₂X₃ (M= Ni, Pd; X= S, Se and Te)," *Materials Today Communications* **25**, 101441 (2020).
- ³¹²Y.-S. Lan, Q. Lu, C.-E. Hu, X.-R. Chen, and Q.-F. Chen, "Strain-modulated mechanical, electronic, and thermal transport properties of two-dimensional PdS₂ from first-principles investigations," *Applied Physics A* **125**, 1–11 (2019).
- ³¹³J. Zhang, Y. Xie, Y. Hu, and H. Shao, "Remarkable intrinsic ZT in the 2D PtX₂ (X= O, S, Se, Te) monolayers at room temperature," *Applied Surface Science* **532**, 147387 (2020).
- ³¹⁴S.-D. Guo, "Biaxial strain tuned thermoelectric properties in monolayer PtSe₂," *Journal of Materials Chemistry C* **4**, 9366–9374 (2016).
- ³¹⁵S.-D. Guo and Y. Wang, "Small compressive strain induced semiconductor metal transition and tensile strain enhanced thermoelectric properties in monolayer PtTe₂," *Semiconductor Science and Technology* **32**, 055004 (2017).
- ³¹⁶W.-L. Tao, Y.-Q. Zhao, Z.-Y. Zeng, X.-R. Chen, and H.-Y. Geng, "Anisotropic Thermoelectric Materials: Pentagonal PtM₂ (M= S, Se, Te)," *ACS Applied Materials & Interfaces* **13**, 8700–8709 (2021).
- ³¹⁷W.-L. Tao, Y. Mu, C.-E. Hu, Y. Cheng, and G.-F. Ji, "Electronic structure, optical properties, and phonon transport in Janus monolayer PtSse via first-principles study," *Philosophical Magazine* **99**, 1025–1040 (2019).
- ³¹⁸W.-L. Tao, J.-Q. Lan, C.-E. Hu, Y. Cheng, J. Zhu, and H.-Y. Geng, "Thermoelectric properties of Janus MXY (M= Pd, Pt; X, Y= S, Se, Te) transition-metal dichalcogenide monolayers from first principles," *Journal of Applied Physics* **127**, 035101 (2020).
- ³¹⁹M. Mukherjee, A. Srivastava, and A. K. Singh, "Recent advances in designing thermoelectric materials," *J. Mater. Chem. C* **10**, 12524–12555 (2022).
- ³²⁰J. Liang, S. Yin, and C. Wan, "Hybrid thermoelectrics," *Annual Review of Materials Research* **50**, 319–344 (2020).
- ³²¹X.-L. Shi, J. Zou, and Z.-G. Chen, "Advanced thermoelectric design: from materials and structures to devices," *Chemical Reviews* **120**, 7399–7515 (2020).
- ³²²S. Gogoc and P. Data, "Organic thermoelectric materials as the waste heat remedy," *Molecules* **27**, 1016 (2022).
- ³²³P. A. Finn, C. Asker, K. Wan, E. Bilotti, O. Fenwick, and C. B. Nielsen, "Thermoelectric materials: Current status and future challenges," *Frontiers in Electronic Materials* **1**, 677845 (2021).
- ³²⁴M. Burton, G. Howells, J. Atoyo, and M. Carnie, "Printed thermoelectrics," *Advanced Materials* **34**, 2108183 (2022),

<https://onlinelibrary.wiley.com/doi/pdf/10.1002/adma.202108183>.